Tevhide ÖZKAYA AHMADOV

M.S. Thesis In Chemistry

August 2008

SYNTHESIS and CHARACTERIZATION of M_3O_4 (M = Fe, Co, Mn) MAGNETIC NANOPARTICLES

by

Tevhide Ö. AHMADOV

August 2008

SYNTHESIS and CHARACTERIZATION of M_3O_4 (M = Fe, Co, Mn) MAGNETIC NANOPARTICLES

by

Tevhide Ö. AHMADOV

A thesis submitted to

the Graduate Institute of Science and Engineering

of

Fatih University

in partial fulfillment of the requirements for the degree of

Master of Science

in

Chemistry

August 2008
Istanbul, Turkey

APPROVAL PAGE

I certify that this thesis satisfies all the requirements as a thesis for the degree of Master of Science.

_____
Assist. Prof. Dr. Metin TÜLÜ
Head of Department

This is to certify that I have read this thesis and that in my opinion it is fully adequate, in scope and quality, as a thesis for the degree of Master of Science.

_____
Assist. Prof. Dr. Abdülhadi BAYKAL
Supervisor

Examining Committee Members

Prof. Dr. Naz Mohammed AGH ATABAY _____

Assoc. Prof. Dr. Yüksel KÖSEOĞLU _____

Assist. Prof. Dr. Abdülhadi BAYKAL _____

It is approved that this thesis has been written in compliance with the formatting rules laid down by the Graduate Institute of Sciences and Engineering.

_____
Assist. Prof. Dr. Nurullah ARSLAN
Director

August 2008

SYNTHESIS and CHARACTERIZATION of M_3O_4 (M = Fe, Co, Mn) MAGNETIC NANOPARTICLES

Tevhide Ö. AHMADOV

M. S. Thesis - Chemistry
August 2008

Supervisor: Assist. Prof. Dr. Abdülhadi BAYKAL

ABSTRACT

In this study, M_3O_4 (M = Fe, Co, Mn) type of spinel compounds were synthesized by various methods (Hydrothermal, surfactant-assisted hydrothermal, oxidation-reduction, gel to crystalline, thermal decomposition and co-precipitation). Structural, morphological, spectroscopic and magnetic characterizations of all samples were done using XRD, TEM, SEM, FTIR and VSM measurements. Crystallite size of the magnetic nanoparticles was determined by Zeta Potential Particle Size Analyzer, XRD (Scherrer equation and line profile fitting method), TEM micrographs. In addition to TEM analysis, for the morphological investigation of some samples, SEM was also used.

PEG (polyethylene glycol) and egg white types of surfactants were used for the first time in this study to synthesize the M_3O_4 spinel nanoparticles.

Superparamagnetic iron oxide (Fe_3O_4, magnetite) nanoparticles were synthesized successfully by four different methods by using NaOH or NH_3 as alkalizing agent. The average crystallite size was determined in the range of 11-25 nm for all magnetite nanoparticles.

Magnetic Co_3O_4 nanoparticles were synthesized by three different methods. These methods are simple and cost effective. By using diffraction profile fitting method, the average crystallite size was calculated in the range of 28-30 nm. Different

morphology was observed because of the effects of surfactants and experimental conditions.

Mn_3O_4, nanoparticles were successfully prepared by a novel oxidation-precipitation method based on oxidation of manganese sulfate to manganese salts and hydrolyzing with NaOH and conc. NH_3. Because of the oxidant agents, morphology and size of the two samples differ from each other. XRD analysis confirmed the tetragonal haussmanite structure with average crystallite size of ~14 nm and ~11 nm; TEM analysis showed crystallite size of 14±5 and 12±3 nm for NaOH and NH_3 hydrolyzed samples respectively.

Keywords: Magnetic Nanoparticles, Spinel Compounds, Hydrothermal Synthesis, XRD, TEM.

M_3O_4 (M= Fe, Co, Mn) MANYETİK NANOPARÇACIKLARININ SENTEZİ VE KARAKTERİZASYONU

Tevhide Ö. AHMADOV

Yüksek Lisans Tezi - Kimya
Ağustos 2008

Tez yöneticisi: Assist. Prof. Dr. Abdülhadi BAYKAL

ÖZ

Bu çalışmada M_3O_4 (M = Fe,Co, Mn) tipi spinel bileşikler değişik metodlar kullanılarak sentezlenmiştir (hidrothermal, surfaktant (CTAB, PEG, pyrrolidone,yumurta akı,) yardımıyla hidrotermal, yükseltgenme-indirgenme, jel-kristal dönüşümü, birlikte çöktürme ve yüksek sıcalıkta bozunma metotları). Sentezlenen maddelerin yapısal, morfolojik, spektroskopik ve magnetik karakterizasyonu XRD, TEM, SEM, FTIR ve VSM metotları kullanılarak analiz edilmiştir. Manyetik nanoparçacıkların kristal boyutu Zeta Potansiyel, XRD, TEM kullanılarak ölçülmüştür. Ek olarak, maddelerin morfolojik özelliklerinin araştırılması için SEM kullanılmıştır.

PEG (polietilen glikol) ve yumruta akı gibi surfactant malzemeler ilk kez bu çalışmada M_3O_4 spinel nano malzemelerin sentezinde kullanılmıştır.

Fe_3O_4 nanoparçacıklar NaOH veya NH_3 kullanılarak dört farklı metodla başarılı bir şekilde sentezlenmiştir. Bütün manyetik nanoparçacıkların ortalama kristal boyutu ise 11-25 nm olarak belirlenmiştir.

Magnetik Co_3O_4 nanoparçacıkları üç değişik metotla sentezlenmiştir. Bu metotlar basit ve düşük maliyetlidirler. XRD metodu kullanılarak ortalama kristal boyutu 28-30 nm olarak hesaplanmıştır. Deneyde farklı morfoloji elde edilmesinde ise surfaktant ve deney koşullarinin etkisinin oldugu gozlenmiştir.

Mn_3O_4, nanoparçacıkları yükseltgenme-indirgenme methoduyla ilk defa başarıyla sentezlenmiştir. Bu metod da mangan sülfat mangan tuzuna yükseltgenir ve NaOH ve konsantre NH_3 kullanılarak hidrolizi sağlanmıştır. XRD analizi sonucunda ortalama kristal boyutu ~14 nm ve ~11 nm olduğu saptanmıştır; daha sonra yapilan TEM analizi sonucu kristal boyutu 14±5 and 12±3 nm olarak belirlenmistir.

Anahtar Kelimeler: Manyetik Nanoparçacıklar, Spinel Bileşikler, Hidrotermal Sentez, XRD, TEM.

This dissertation is dedicated to my family

ACKNOWLEDGMENT

I am really grateful to those who give direct and indirect contribution to this dissertation. I appreciate their invaluable helps and advices for my work.

First and foremost, I thank my thesis supervisor, Assist. Prof. Dr. Abdülhadi BAYKAL, for his guidance and understanding throughout my research work and writing thesis. His constant encouragement and significant suggestions made this work successful.

I specially thank to Asst. Prof. Dr. Muhammed S. TOPRAK for his generous assistance and insightful discussions during SEM, TEM, Zeta Potential analysis of my compounds in Royal Institute of Technology in Sweden.

I thank to Prof.Dr.Bekir AKTAŞ and Assoc.Prof.Dr. Yüksel KÖSEOĞLU, for their valuable discussions and suggestions for VSM studies. And I am also grateful to our group member Dr. Hüseyin KAVAS for his efforts to achieve novel analysis methods such as a goal in magnetic studies.

I thank to The Graduate Institute of Sciences and Engineering of Fatih University for funding my thesis with the AFP no of P50020602.

I also would like to thank my dissertation committee members Prof. Dr. Naz Mohammed AGH ATABAY and for his valuable times and their advices for the research work.

Lastly, but in no sense the least, I am very grateful to Bahar Birsöz and Hilal Onay for their suggestions and helpful discussions.

My deep thanks go to my family for their love, encouragement, support, care and patience. This dissertation is dedicated to them.

TABLE OF CONTENTS

ABSTRACT……iii
ÖZ……...…...v
ACKNOWLEDGMENT……viii
TABLE OF CONTENTS…….....ix
LIST OF TABLES…….xiii
LIST OF FIGURES……..…..xiv
CHAPTER 1 INTRODUCTION……..…….……1
1.1 General Introduction……..……..1
1.2 Properties of Nanoparticles……6
1.2.1 Geometric Structure…….……..8
1.2.2 Melting Point……...…….10
1.2.3 Electronic Properties…….……11
1.2.3.1 Catalysis and Reactivity…….……..12
1.2.4 Optical Properties……...……12
1.2.5 Magnetic Properties……..…….14
1.3 Preparation of Nanoparticles…….15
1.3.1 Physical Methods……..……..17
1.3.2 Chemical Methods……..18
1.3.2.1 Metal Nanocrystals by Reduction……20
1.3.2.1.1 Borohydrate Reduction…….20
1.3.2.1.2 Alcohol Reduction……22
1.3.2.1.3 Citrate Reduction……..22
1.3.2.2 Solvothermal Synthesis……23
1.3.2.3 Photochemical Synthesis……..23
1.3.2.4 Electrochemical Synthesis……..…….24
1.3.2.5 Thermolysis Routes……..…25
1.3.2.6 Sonochemical Routes……...……25

1.3.2.7 Michelles and Microemulsions……26
1.3.2.8 The Liquid- liquid Interface…….27
1.3.3 Size Tuning…….……28
1.3.3.1 Effect of Heating Time…….……...……30
1.3.3.2 Effect of Reaction Temperature……..…….31
1.1.4 Shape Control of Nanoparticles……..……..……32
1.4 Magnetic Nanoparticles (MNPs)…….……..34
1.4.1 Synthesis of MNPs…….34
1.4.1.1 Synthesis of Single Metal MNPs…….……35
1.4.1.2 Synthesis of Alloyed Metal Nanoparticles……..……37
1.4.1.3 Synthesis of Metal Oxide Nanoparticles……..38
1.4.1.4 Preparation of Bioconjugates MNPs……39
1.4.1.5 Biosynthetic Routes to MNPs……..40
1.4.2 Physical Properties of MNPs…….41
1.4.2.1 Spinel Crystal Structure……..…….41
1.4.3 Characterization Techniques of MNPs……..…….42
1.5 Magnetism of MNPs……...…46
1.5.1 Type of Magnetism…….47
1.5.1.1 Diamagnetism and paramagnetism……..……47
1.5.1.2 Ferromagnetism……...…49
1.5.1.3 Antiferromagnetism…….54
1.5.1.4 Ferrimagnetism……55
1.6 Applications of MNPs……...……55
1.7 Purpose of the Thesis…….……57
CHAPTER 2 EXPERIMENTAL…….…...58
2.1 INSTRUMENTATION……...58
2.1.1 X-ray Powder Diffraction (XRD)……..……58
2.1.2 Electron Microscopy…….……..58
2.1.2.1 Scanning Electron Microscopy (SEM)……...…….58
2.1.2.2 Transmission Electron Microscopy (TEM)…….58

2.1.3 Fourier Transform Infrared Spectroscopy (FTIR)……59
2.1.4 Vibrating Sample Magnetometer (VSM)……..59
2.1.5 Zeta Potential…….59
2.2 PROCEDURE…….……59
2.2.1 Fe_3O_4 NANOPARTICLES…….59
2.2.1.1 Cost-effective gel-to-crystalline method (Tev13)…..……..…….59
2.2.1.2 Co-precipitation and Hydrothermal Synthesis
(Tev9 & Tev19)……..60
2.2.1.3 Oxidation-Reduction Method (Tev14a & Tev25)…..…..……61
2.2.1.4 PEG-assisted Route (Te2 & Te 3)…….……..…...….61
2.2.2 Co_3O_4 NANOPARTICLES…….…..……62
2.2.2.1 Reflux Method (Tev37)…..…….……62
2.2.2.2 Oxidation-Reduction Method (Tev11b)…….…….62
2.2.2.3 Simple Route Using Egg White (Te19)……...……63
2.2.3 Mn_3O_4 NANOPARTICLES…….63
2.2.3.1 Thermal Decomposition Method (Tev29)…..…….…..…63
2.2.3.2 Oxidation-Reduction Method (Tev12a & Tev21)…...……63
2.2.3.3 PEG-assisted Route (Te5)……...……64
CHAPTER 3 RESULT AND DISCUSSION…….65
3.1 Fe_3O_4 Analysis……65
3.1.1 Fe_3O_4 Nanoparticles by cost-effective gel-to crystalline method
(Tev13)… ……...65
3.1.1.1 XRD analysis……...66
3.1.1.2 FTIR analysis…….…..67
3.1.1.3 TEM analysis……...68
3.1.1.4 Magnetization……..70
3.1.2 Fe_3O_4 nanoparticles by hydrothermal synthesis (Tev9 & Tev19).……75
3.1.2.1 XRD analysis……...75
3.1.2.2 FTIR analysis……...……76
3.1.2.3 SEM & TEM analysis…..……77

3.1.3 Fe_3O_4 nanoparticles by oxidation-reduction method (Tev14a & Tev25).....81
3.1.3.1 XRD analysis…….……81
3.1.3.2 FTIR analysis……..……82
3.1.4 Fe_3O_4 nanoparticles by PEG-assisted route (Te2 & Te3)…….....…..83
3.1.4.1 XRD analysis…….……..…83
3.1.4.2 FTIR analysis…….….84
3.2 Co_3O_4 Analysis…….……...85
3.2.1 Co_3O_4 nanoparticles by reflux and oxidation-reduction method…..……85
3.2.1.1 XRD analysis…….....85
3.2.1.2 FTIR analysis…….86
3.2.1.3 SEM & TEM analysis……..……..88
3.2.1.4 Magnetization……...91
3.2.2 Co_3O_4 Simple Route Using Egg White (Te19)...……...95
3.2.2.1 XRD analysis…….…….....95
3.2.2.2 FTIR analysis…….97
3.3 Mn_3O_4 Analysis……...98
3.3.1 Mn_3O_4 nanoparticles by thermal decomposition method (Tev29).....…...98
3.3.1.1 XRD analysis…….……...……...98
3.3.1.2 FTIR analysis……...…99
3.3.1.3 SEM analysis……..101
3.3.2 Mn_3O_4 nanoparticles by oxidation-reduction method (Tev12a & Tev21)……...…….104
3.3.2.1 XRD analysis……...……...….....104
3.3.2.2 FTIR analysis……...……..105
3.3.2.3 TEM analysis……..……..……106
3.3.2.4 Magnetization……..…….……..107
3.3.3 PEG-assisted Route (Te5)……...112
3.3.3.1 XRD analysis……...…….....112
3.3.3.2 FTIR analysis…….113

CHAPTER 4 CONCLUSIONS…….115
REFERENCES……..118

LIST OF TABLES

TABLE

Table 1. Infrared Transmission Frequencies of 2-Pyrrolidone and the final product.....100

LIST OF FIGURES

FIGURE

1.1 Nanometer in context……..……...2

1.2 Lycurgus Cup (British Museum; AD fourth century)……..……3

1.3 Schematic Diagram of the inter- and intro agglomerate porosity in the agglomerate powder…….…….....5

1.4 Materials with nanometer dimensions……..……5

1.5 CdSe, CdSe/ZnS and water soluble quantum dots……...……6

1.6 Schematic illustration of the factors lending stability to a colloidal dispersion: a)an electric double layer and (b) loss of conformational freedom of chain-like ligands……7

1.7 Schematic illustration of the size-dependence of manifold nanocrystal Properties……..…….7

1.8 Plot of the number of atoms vs. the percentage of atoms located on the surface of a particle. The calculation of the percentage of atoms is made on the basis of (1.1) and is valid for metal particles……..…..…..8

1.9 Schematic illustration of how a cuboctahedral 147 atom-cluster, composed of seven close-packed layers can be made out of a stacking sequence reminiscent of a fcc lattice……...……...9

1.10 Optical absorption spectra of gold nanoparticles with diameters of 22, 48, and 99 nm……..……...…13

1.11 Emission from ZnS coated CdSe nanocrystals of different sizes, dispersed in hexane……..13

1.12 Plot showing the variation of saturation magnetization with the inverse of mean diameter for $MnFe_2O_4$ nanoparticles at 20K……...…….14

1.13 Unit cell of spinel ferrites .In certain cases, the surface layer makes nanoparticle behave like a spin glass……...……15

1.14 Preparation methods of nanoscale materials. (a) In a top-down process, material is removed from a monolithic entity resulting in the nanostructure. (b) In a bottom- up process, building-blocks self-organize to form the nanostructure……....16

1.15 Two approaches to the synthesis of nanoparticles. A comparision of nanochemistry and Nanophysics…….17

1.16 Schematically illustration of physical methods of synthesizing nanoparticles……...…….18

1.17 Ostwald ripening.…….19

1.18 Some Reducing Agents to synthesize nanocrystals…….20

1.19 Schematic of the synthesis of metal nanoparticles within dendrimer templates……..…..……22

1.20 Schematic illustration of the steps involved in the electrochemical reduction of metal nanocrystals by the Reetz method……..……24

1.21 Schematic diagram showing the mechanism of formation of nanoparticles with microemulsion technology……..……27

1.22 Nanocrystals of: (a) Au, (b) CdS, and (c) γ–Fe2O3 formed at the toluene water interface…….…….28

1.23 Organometallic synthesis of $CoPt_3$ nanocrystals……..……....29

1.24 Synthesis of nanoparticles in the absence of Ostwald ripening…….…..30

1.25 Dependence of FePt (a) and $CoPt_3$ (b) nanocrystal size on duration of heating during the synthesis ……30

1.26 Dependence of $CoPt_3$ nanocrystal size on the reaction temperature…..…..…….31

1.27 TEM and HRTEM images showing effect of the reaction temperature on the mean size and size distribution of $CoPt_3$ nanocrystals: 3.7-, 4.9-, 6.3-, and 9.3-nm large particles were prepared at 220, 200, 170 and 145°C, respectively……..……..32

1.28 TEM image of Au nanorods prepared by the seed mediated growth method……...……..…33

1.29 TEM images showing cubic to rod-shaped gold particles produced with low concentrations of ascorbic acid in the presence of a small quantity of silver nitrate, by seed-mediated growth method……....33

1.30 Schematimatically illustration of synthesizing methods of MNPs……..35

1.31 Example of the production of Ni MNPs by H_2NNH_2 reduction of $NiCl_2$ in a w/o microemulsion system…….36

1.32 (a) Thermal decomposition of $Fe(CO)_5$ in the presence of oleic acid and TOPO to produce Fe MNPs and (b) use of varying ligands to produce Co MNPs with spherical , rod, disk morphologies from $Co_2(CO)_8$. ……..……..37

1.33 Synthesis of solid solution FePt MNPs…….……..38

1.34 Aqueous preparative methods for synthesis of iron oxide MNPs……..38

1.35 Reaction of CLIO-NH_2 with heterobifunctional crosslinkers, producing nanoparticles that are starting points for the creation of bioconjugated MNPs…….....39

1.36 Synthesis of magnetoliposomes (a) by employing a lipid bilayer as a reactor and (b) lipid coating of Fe_3O_4 MNPs…….40

1.37 The structure of spinels. **(**Crystal structures of magnetite, Fe_3O_4). (a) Face-centered cubic inverse spinel structure of magnetite. (b) Magnification of one tetrahedron and one adjacent octahedron sharing an oxygen atom. ……..….41

1.38 a) Crystal Structure of $CoFe_2O_4$ and b) $LiMn_2O_4$. …….……42

1.39 Highly simplified view of structure of TEM……...……43

1.40 Highly simplified view of structure of SEM……..…….44

1.41 Schematic representation of zeta potential……..……....46

1.42 A periodic table showing the type of magnetic behavior of each element at room temperature…….……47

1.43 Field dependence of magnetization in paramagnetic and diamagnetic materials……...48

1.44 Linear arrays of spins illustrating possible (a) ferromagnetic, (b)antiferromagnetic, and (c) ferrimagnetic orderings……50
1.45 Magnetization curve of iron, cobalt, and nickel at room temperature…….51
1.46 Magnetization vs Temperature plot…….52
1.47 Hysteresis loop…….53
1.48 Temperature dependence of the magnetic susceptibility in paramagnets, ferromagnets, and antiferromagnets……55
1.49 Schematic illustration of **s**ome applications of MNPs…….57
2.1 Scheme of synthesizing Fe_3O_4 nanoparticles by reflux……..…….……60
2.2 Scheme of synthesizing Mn_3O_4 nanoparticles by Oxidation-Reduction Method……64
3.1 X-ray powder diffraction pattern and theoretical profile fit of as-synthesized Fe_3O_4 nanoparticles…….……67
3.2 FTIR spectra of as-synthesized iron oxide nanoparticles and commerical magnetite powder……..68
3.3 TEM micrograph (a), calculated histogram (b), and Electron diffraction pattern, (c) for as-synthesized iron oxide nanoparticles…….….69
3.4 Magnetization versus magnetic field curves for iron oxide nanoparticles at (a) 300 K and (b) 10 K. ……..…….……....71
3.5 M-T curves for as-synthesized iron oxide nanoparticles recorded in the presence of 200 Oe field……73
3.6 XRD patterns of Fe_3O_4 nanoparticles with and without CTAB……...….75
3.7 FTIR spectra of Fe_3O_4 nanoparticles with(Tev19) and without CTAB(Tev9)……...76
3.8 SEM micrographs iron oxide nanoparticles without CTAB (Tev9)……...……77
3.9 SEM micrograph iron oxide nanoparticles with CTAB (Tev19)……...…78
3.10 TEM micrographs of iron oxide nanoparticles without CTAB (Tev9)…….…79
3.11 TEM micrograph iron oxide nanoparticles with CTAB (Tev19)……....80
3.12 XRD patterns of Fe_3O_4 nanoparticles ……...……..81
3.13 FTIR spectra of Fe_3O_4 nanoparticles…….……..82

3.14 XRD patterns of PEG-Fe_3O_4 nanoparticles……...…83
3.15 FTIR spectra of PEG-Fe_3O_4 nanoparticles……...….84
3.16 XRD patterns of Co_3O_4 nanoparticles with the line profiles fitting……..….86
3.17 FTIR spectra of Co_3O_4 nanoparticles prepared by reflux method (Tev37) and oxidation- reduction method (Tev11b)……...…...…...87
3.18 SEM micrographs of Co_3O_4 nanoparticles prepared by Reflux method (Tev11b)……...……...….88
3.19 SEM micrographs of Co_3O_4 nanoparticles prepared by oxidation-reduction method (Tev37)……89
3.20 TEM micrographs of Co_3O_4 nanoparticles prepared by reflux method (Tev11b)……..…..…90
3.21 TEM micrographs of Co_3O_4 nanoparticles prepared by oxidation-reduction method (Tev37)……...….90
3.22 Room temperature M-H Curves of sample Tev11 (27 nm) and Tev37 (30 nm)…….……..91
3.23 M-H Curve of sample Tev11 (27 nm) and Tev37 (29.7 nm) at 10 K. The inset shows an expansion of the central portions……..……..……92
3.24 Central portions of FC hysteresis loops at low field showing an obvious loop shift……..…….……93
3.25 M-T curves of sample Tev11b with 200 Oe applied field……..94
3.26 M-T curves of sample Tev37 with 200 Oe applied field ……95
3.27 XRD Powder pattern of Co_3O_4 nanoparticles (Te19)….…….96
3.28 FTIR of Co_3O_4 nanoparticles.(Te19)……..…….97
3.29 Reaction scheme for the synthesis of 2-pyrrolidone capped Mn_3O_4 nanoparticles……98
3.30 X-ray powder diffraction pattern of as-prepared capped Mn_3O_4 nanoparticles……...…….99
3.31 FTIR spectra of (a) pure 2-pyrrolidone, and (b) 2-pyrrolidone capped Mn_3O_4 nanoparticles...……..……101

3.32 a) SEM micrograph, b) TEM micrograph, and c) calculated histogram of 2-pyrrolidone capped Mn_3O_4 nanoparticles…….……102

3.33 Surface potential measurement of a clear suspension of 2-pyrrolidone capped Mn_3O_4 nanoparticles…….……103

3.34 XRD patterns of Mn_3O_4 nanoparticles synthesized using (a) NaOH (Tev12a); (b) NH_3 gas (Tev21) as hydrolyzing agent……..…….105

3.35 FTIR spectra of Mn_3O_4 of nanoparticles synthesized using (a) NaOH (Tev12a); (b) NH_3 gas (Tev21) as hydrolyzing agent…..……...……..…….106

3.36 TEM micrographs of Mn_3O_4 nanoparticles synthesized using (a) NaOH (Tev12a); (b) NH_3 gas (Tev21) as hydrolyzing agent…..……..107

3.37 Temperature variation of the FC magnetization measurements of Mn_3O_4 nanoparticles synthesized using (a) NaOH (Tev12a); (b) NH_3 gas (Tev21) as hydrolyzing agent. ……..…..…….……..…..108

3.38 Room temperature M-H curves for Mn_3O_4 nanoparticles synthesized using (a) NaOH (Tev12a); (b) NH_3 gas (Tev21) as hydrolyzing agent…..…….....109

3.39 M-H curves measured at Temperatures below T_c for Mn_3O_4 nanoparticles synthesized using (a) NH_3 gas (Tev21); (b) NaOH (Tev12a) as hydrolyzing agent……...……...111

3.40 XRD patterns of PEG-Mn_3O_4 nanoparticles……..112

3.41 FTIR spectra of PEG-Mn_3O_4 nanoparticles……..…….114

CHAPTER 1

INTRODUCTION

1.1 General Introduction

Nanotechnology [1] is enabling technology that deals with nano-meter sized objects and will be developed at several levels: materials, devices and systems. Nanotechnology is interdisciplinary and relies on scientists who come from a broad range of backgrounds, such as materials science, colloid and interface and science, biological and medical science as well as many of the engineering disciplines [2].

The prefix ‘nano’ is derived from the Greek word for dwarf. Nanoparticles are often determined as particles of less than 100 nm in diameter. A nanometer (nm) is extremely small, equal to one billionth of a meter. For comparison, a human hair is approximately 80,000 nm wide, a red blood cell is almost 7,000 nm wide , a DNA double- helix is around 2 nm wide, and a typical carbon-carbon bond length in the range 0.12- 0.15 nm [3]. Fig.1.1 illustrates the nanometer in context. Atoms are below a nanometer size, whereas many molecules, including some proteins, range from a nanometer upwards [4].

Nanoparticles, major class of nanomaterials, are zero-dimensional, possessing nanometric dimensions in all the three dimensions. And their diameters can vary between one and a few hundreds of nanometers. Accordingly, the electronic and atomic structures of such small nanoparticles have unusual features, obviously different from those of the bulk materials. On the other hand, large nanoparticles which are bigger than 20–50 nm, would have properties similar to those of the bulk [5]. The size-dependent properties of nanoparticles comprise electronic, optical, magnetic, and chemical characteristics. In other words, changing the size of nanoscale materials produces new materials [6].

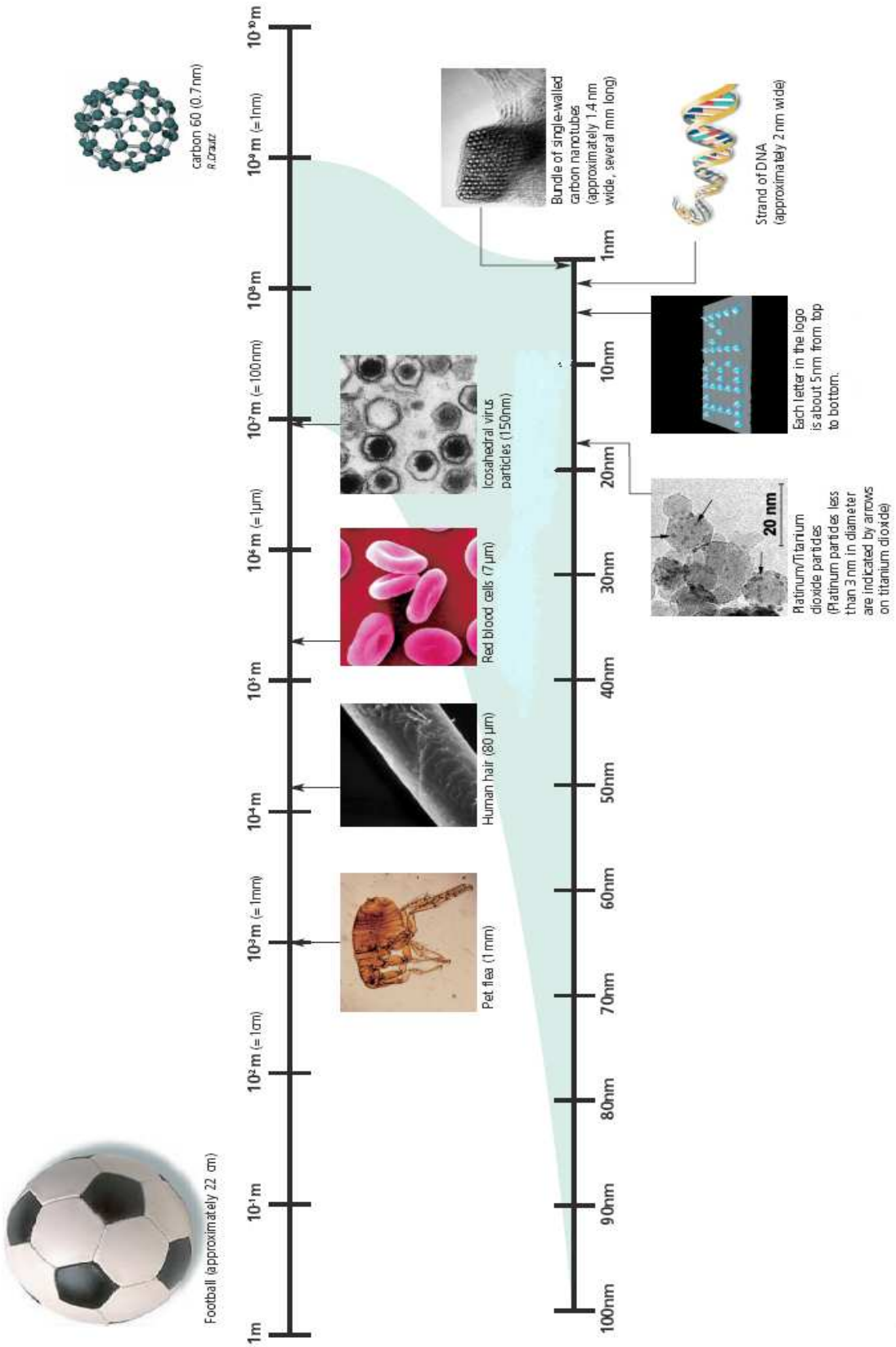

Figure 1.1. Nanometer in context [4].

For instance, in transition metal nanoparticles, an increase in surface area results in a corresponding increase in chemical reactivity, making them potentially useful as catalysts. In addition, quantum effects of nanoparticles become more important and can change a particle's optical, magnetic, or electrical properties [7].

Nanoparticles can be amorphous or crystalline. Crystalline nanoparticles, being small in size, can be of single domain. Nanoparticles of metals, chalcogenides, nitrides, and oxides are often single crystalline. Crystalline nanoparticles are named as nanocrystals [8].

Nanoparticles are not novel and their history can be traced back to the Roman period. Colloidal metals were used to dye glass articles and fabrics and as a therapeutic aid in the treatment of arthritis. The Purple of Cassius, formed on reacting stannic acid with chloroauric acid, was a popular purple dye in the olden days. It is actually made up of tin oxide and Au nanocrystals [9]. The Romans were skillful at impregnating glass with metal particles to achieve dramatic color effects. The Lycurgus cup, a glass cup of 4th century AD, appears red in transmitted light and green in reflected light (Figure 1.2). This effect, which can be seen in the cup preserved in the British museum in London, is due to Au and Ag nanocrystals present in the walls of the cup. Maya blue, a blue dye employed by the Mayas around 7th century AD has been shown recently to consist of metal and oxide nanocrystals in addition to indigo and silica [10].

Figure 1.2. Lycurgus Cup (British Museum; AD fourth century) [10].

Nanoparticles have a range of potential applications in areas as diverse as drug delivery, catalyst and catalytic carrier, information and communication technologies, water decontamination, and the production of stronger, lighter materials. For example, titanium dioxide and zinc oxide particles become translucent at nanoscale size and are able to absorb UV light while allowing visible light to pass through, so they are used in sunscreens. In the last couple of decades, the field of nanoparticles has witnessed a rapid growth. The research efforts are expected to produce monodisperse nanoparticles, to provide a fundamental understanding of 'nano-sized particles' general and surface properties, and to use their properties to create devices and systems with new functions. All scientific activities are driven by the excitement of understanding nanoscience and potential applications in numerous fields, assisted by the development of characterization techniques for measuring and observing nanoparticles such as electron beam techniques and scanning probe techniques [11-13].

Classification of Nanomaterials

In the nanostructured materials field, many names and labels have been used. It is significant that some terms are explained in the nanoscale materials**:**

Cluster → A collection of units (atoms or reactive molecules) of up to about 50 units. Cluster *compounds* are such moieties surrounded by a ligand shell that allows isolation of a molecular species (stable, isolable, soluble).

Colloid → A stable liquid phase containing particles in the 1-1000 nm range. A colloidal particle is one such 1-1000 nm sized particle

Nanoparticle →A solid particle in the 1-1000 nm range that could be nanocrystalline, an aggregarate (Fig.1.3) of crystallites, or a single crystalline;

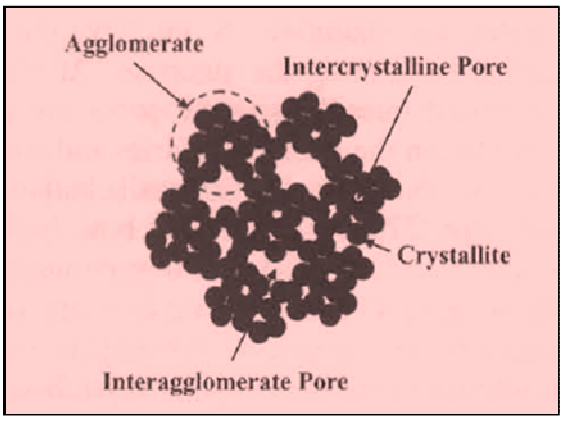

Figure 1.3. Schematic diagram of the inter- and intro agglomerate porosity in the agglomerate powder [14].

Nanocrystal → A solid particle that is a single crystal in the nanometer size range.

Nanostructured or nanoscale material → Any solid material that has a nanometer dimension (Fig.1.4);

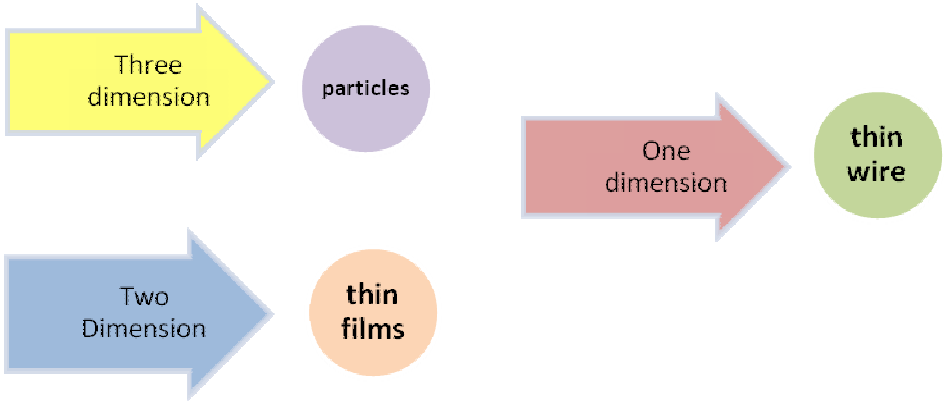

Figure 1.4. Materials with nanometer dimensions.

Nanophase material → The same as nanostructured materials.

Quantum dot → A particle that reveals a size quantization effect in at least one dimension [15] (Fig. 1.5 exhibits an example of quantum dots [16]).

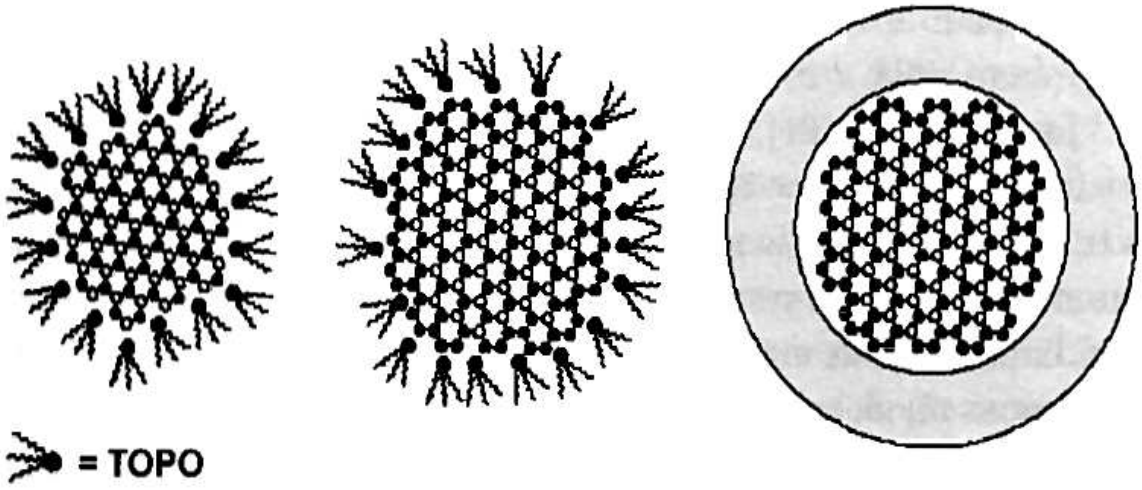

Figure 1.5. CdSe, CdSe/ZnS and water soluble quantum dots [16].

1.1 Properties of Nanoparticles

Nanocrystals of materials are commonly obtainable as sols. Sols containing nanocrystals behave like the classical colloids. For example, the stability of dispersion depends on the ionic strength of the medium. Nanocrystalline sols have exceptional optical clarity. A key factor that lends stability to nanocrystal sols is the presence of a ligand shell, a layer of molecular species adsorbed on the surface of the particles. Without the ligand shell, the particles tend to aggregate to form bulk species that flocculate or settle down in the medium. Depending on the dispersion medium, the ligands lend stability to particles in two different ways. Thus, in an aqueous medium, coulomb interactions between charged ligand species provide a repulsive force to counter the attractive van der Waals force between the tiny grains, by forming an electrical double layer. In an organic medium, the loss of conformational freedom of the ligands and the apparent increase in solute concentration provide the necessary repulsive force. Nanocrystals dispersed in liquids are either charge-stabilized or sterically stabilized (Fig.1.6) [8].

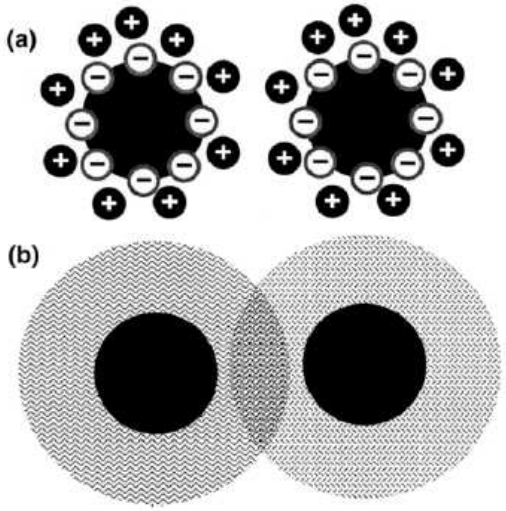

Figure 1.6. Schematic illustrations of the factors lending stability to a colloidal dispersion: (**a**) an electric double layer and (**b**) loss of conformational freedom of chain- like ligands [8].

It is practical to categorize sizes of nanocrystals into different regimes specific to the different properties, beyond which size dependence would not be related. The schematic in Figure 1.7 shows this aspect. All the regimes begin essentially with small clusters (≥1 nm), but the upper limits are different [8].

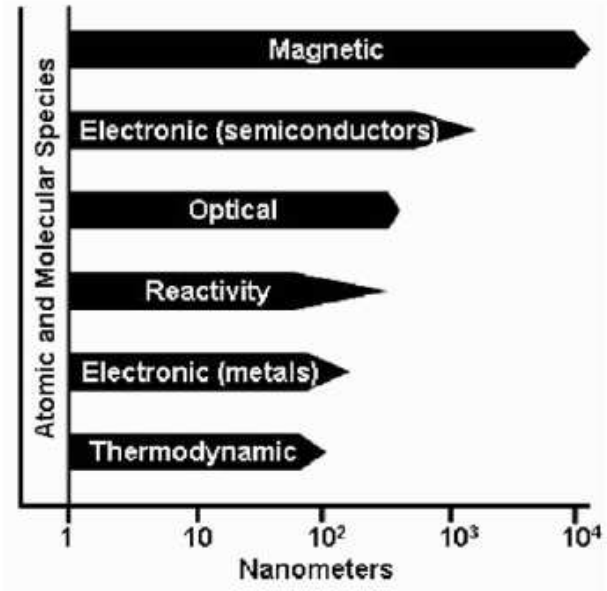

Figure 1.7. Schematic illustration of the size-dependence of manifold nanocrystal properties. The property specific regimes are indicated [8].

1.1.1 Geometric Structure

The dimensions of nanocrystals are so close to atomic dimensions that an unusually high fraction of the total atoms would be present on their surfaces. For example, a particle consisting of 13 atoms, would have 12 atoms on the surface, regardless of the packing scheme followed. Such a particle has a surface more populated than the bulk. It is possible to estimate the fraction of atoms on the surface of the particle (*P*s, percentage) using the simple relation,

$$P\text{s} = 4N^{-1/3} \times 100, \quad (1.1)$$

where N is the total number of atoms in the particle [17]. The variation of the surface fraction of atoms with the number of atoms is shown in Figure 1.8. We see that the fraction of surface atoms becomes less than 1% only when the total number of atoms is of the order of 10^7, which for a typical metal would correspond to a particle diameter of 150 nm [8].

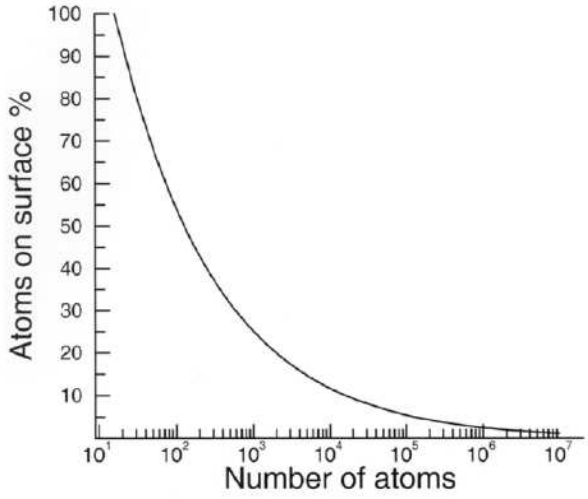

Figure 1.8. Plot of the number of atoms vs. the percentage of atoms located on the surface of a particle. The calculation of the percentage of atoms is made on the basis of (1.1) and is valid for metal particles [8].

Nanoparticles are generally assumed to be spherical. However, an interesting interplay exists between the morphology and the packing arrangement, specially in small nanocrystals. If one were to assume that the nanocrystals strictly follow the bulk crystalline order, the most stable structure is arrived at by simply constraining the

number of surface atoms. It is reasonable to assume that the overall polyhedral shape has some of the symmetry elements of the constituent lattice. Polyhedra such as the tetrahedron, the octahedron, and the cuboctahedron can be constructed following the packing scheme of a fcc lattice [18, 19]. Figure 1.9 shows how a cuboctahedral cluster of 146 constituent atoms follows from a fcc type *abcabc* layer stacking.

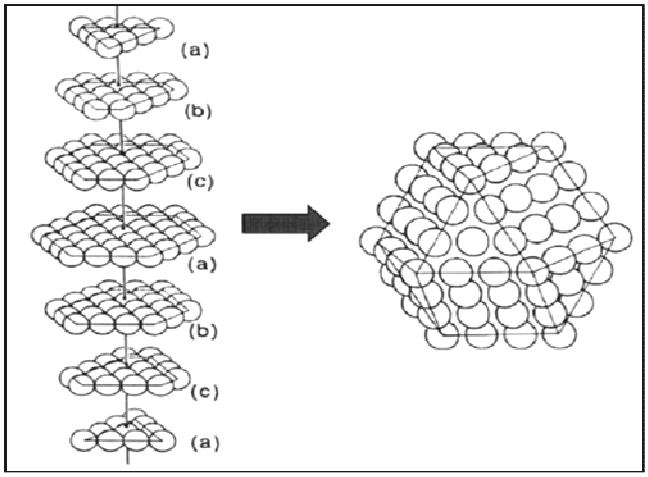

Figure 1.9. Schematic illustration of how a cuboctahedral 147 atom-cluster, composed of seven close-packed layers can be made out of a stacking sequence reminiscent of a fcc lattice [8].

Determination of the structures of nanocrystals should ideally follow from X-ray diffraction, but small particles do not diffract well owing to their limited size. The peaks in the diffraction pattern are less intense and are broad. Structural studies are therefore based on high resolution transmission electron microscopy (HRTEM), extended X-ray absorption fine structure (EXAFS), scanning tunneling microscopy (STM) and atomic force microscopy (AFM). X-ray diffraction patterns provide estimates of the diameters (D) of nanocrystals from the width of the diffraction profiles, by the use of the Scherrer formula [20].

$$D = 0.9\lambda / \beta\cos\theta \qquad (1.2)$$

Here, β is the full-width at half-maximum of the broadened X-ray peak corrected for the instrumental width,

$$\beta = \beta 2\text{observed} - \beta 2\text{instrumental.} \quad (1.3)$$

Estimates based on the Scherrer relation are used routinely. It is desirable to carry out a Reitveld analysis of the broad profiles of nanoparticles to obtain estimates of *D*.

HRTEM with its ability to image atomic distributions in real space, is a popular and powerful method. High resolution imaging provides compelling evidence for the presence of multiply twinned crystallites specially in the case of Au and Ag nanoparticles [21]. Characterization by electron microscopy also has certain problems. For example, the ligands are stripped from the clusters under the electron beam; the beam could also induce phase transitions and other dynamic events like quasi-melting and lattice reconstruction [22]. The fact that ligands desorb from clusters has made it impossible to follow the influence of the ligand shell on cluster packing.

STM, with its ability to resolve atoms, provides exciting opportunities to study the size and morphology of individual nanoparticles. In the case of ligated nanocrystals, the diameters obtained by STM include the thickness of the ligand shell. Ultra high vacuum STM facilitates in situ studies of clusters deposited on a substrate. Furthermore, it is possible to manipulate individual nanoscale particles using STM. However, it is not possible to probe the internal structure of a nanocrystal, especially if it is covered with a ligand shell. AFM supplements STM and provides softer ways of imaging nanocrystals. EXAFS has advantages over the other techniques in providing an ensemble average, and is complimentary to HRTEM [8].

1.1.2 Melting Point

"Does the melting temperature of a small particle depend on its size?" asked Lord Kelvin as early as in 1871 [23]. The majority in those days seemed to be that it would not be the case. An initial attempt was made to examine this issue by Pawlow in 1909 [24]. The first demonstration that the melting point was indeed different in small particles is due to Takagi [25], who established by means of electron microscopy that nanoscale particles of Pb, Sn, and Bi with sizes in the range of a few nanometers exhibited lower melting temperatures. Buffat et al. [26] carried out extensive studies on

the melting points of Au nanocrystals by means of scanning electron diffraction technique and compared their results with previous findings. The change in the melting point can be quite dramatic, with lowering of as much as 600 K in Au nanocrystals. It is supposed that the surface atoms are more susceptible to thermal displacement and initiate the melting process due to the lower coordination. Such a surface melting process is thought to be the major cause for the lowering of melting points. Lately, an entirely different melting behavior has been observed for much smaller particles of nuclearities less than 500.

1.2.3 Electronic Properties

Electronic properties of nanocrystals critically depend on size. This aspect is properly put forth in the quest “How many atoms make a metal?” It is clear that as the size of metal nanocrystals is reduced, the accompanying changes in the electronic structure render them insulating. This transition, called the size-induced metal–insulator transition (SIMIT), has evoked much interest from chemists and physicists alike. A SIMIT is manifested in experiments that measure the electronic band structure and atomistic properties such as ionization energy.

In small metal particles containing up to a few hundred atoms, the electronic properties are entwined with changes in the structure and bonding. The closure of electronic and geometric shells also plays a part in determining the electronic structure of small metal particles. A large part of the understanding of bare metal clusters follows from the measurement of ionization energy [8]. Ionization energy is generally measured by means of photo ionization. A cluster beam is ionized by photons from a monochromatized UV source or a tunable laser and the mass distribution of the produced ions are analyzed after considering factors such as the temperature of the clusters and their cross-sections. Such measurements have been carried out on several s, p, and transition metal clusters [27, 28].

1.2.3.1 Catalysis and Reactivity

Metal nanocrystals have been used as catalysts in commercial processes. The use of fine particles is attractive in view of their high surface areas per unit volume. The catalytic activity of nanocrystals is affected by other factors as well. A brief illustration is provided by the findings on Au catalysis. Despite its reputation as a noble metal, Au is found to be catalytically active at the nanoscale. An early study by Haruta et al.[29] found that Au nanocrystals embedded in oxide supports such as α-Fe_2O_3, Co_3O_4, and NiO were highly active for CO oxidation even at temperature as low as 200 K. Au nanocrystals with diameters in the range of 5–10nm supported on γ-Al_2O_3 were capable of catalyzing CO oxidation [30]. Larger Au nanocrystals were not catalytically active. Goodman and coworkers [31] have observed that Au nanocrystals supported on titania exhibit a marked size effect in their catalytic ability for CO oxidation, with Au nanocrystals in the range of 3.5 nm exhibiting maximum chemical reactivity. Tunneling spectroscopic measurements reveal that accompanying maximum catalytic activity is a metal to nonmetal transition, as the cluster size is decreased below 3.5 nm^3.

1.2.4 Optical Properties

Optical properties of nanocrystals have been of interest for centuries.Optical properties of nanocrystals of metals such as Au across a large size range reflect the changes in the electronic properties that occur with the variation in size. While it is ideal to study the optical properties using nanocrystals prepared by a single method, no single method, chemical or physical, yields nanocrystals of all the required size ranges.

Metal nanocrystals of various sizes exhibit characteristic colors depending on their diameters and the dielectric constant of the surrounding medium. Typical size-dependent changes in the optical spectra are illustrated in Fig.1.10 [32].

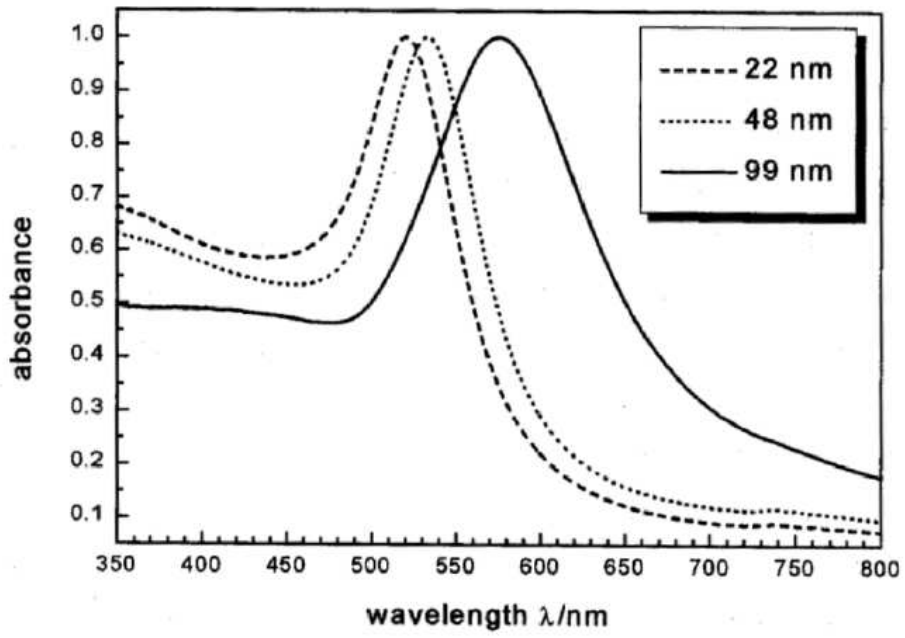

Figure 1.10. Optical absorption spectra of gold nanoparticles with diameters of 22, 48, and 99 nm [32].

In addition to properties associated with optical absorption, semiconductor nanocrystals exhibit interesting luminescent behavior. The luminescence generally dependent on the size of the nanocrystals and the surface structure. A photograph showing changes in the emission wavelength as a function of size of semiconductor quantum dots is illustrated in Fig.1.11.

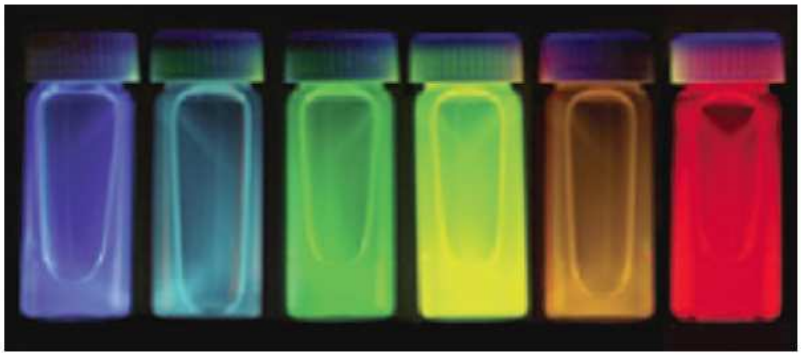

Figure 1.11. Emission from ZnS coated CdSe nanocrystals of different sizes, dispersed in hexane [33].

1.2.4 Magnetic Properties

Magnetic properties at the nanoscale strongly depend on the interplay involving the surface atoms and the energetics of spin reversal. When particles of a wide range of sizes are investigated, their coercivity tends to follow a trend. Changes in coercivity with size can often be complicated. In the nanoregime, it is possible that shape anisotropy has a higher value than the magnetocrystalline anisotropy, specially in elongated particles and nanorods' properties.

Magnetic properties such as the saturation magnetization also exhibit size-dependent changes at the nanoscale. The saturation magnetization of nanocrystals is less than that of the corresponding bulk, because of the dead layer on the surface. Figure 1.12 shows the variation of saturation magnetization with size for $MnFe_2O_4$ nanoparticles. A linear correlation is obtained with the inverse of diameters and can be useful to estimate the thickness of the magnetically inactive surface layer [34].

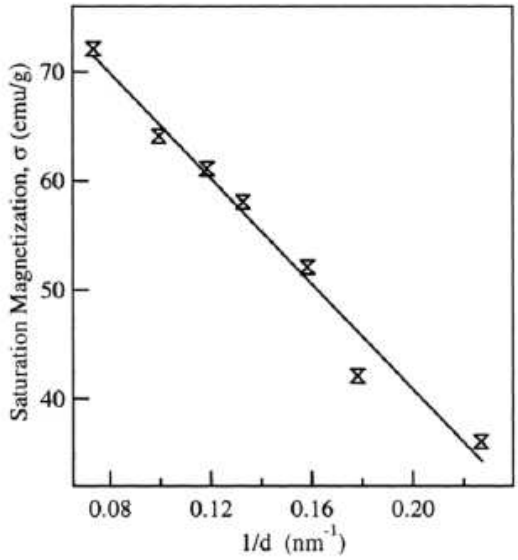

Figure 1.12. Plot showing the variation of saturation magnetization with the inverse of mean diameter for $MnFe_2O_4$ nanoparticles at 20K [34].

Much of our understanding of magnetic properties of fine particles is derived from studies on magnetic oxide systems, especially spinels. Spinel ferrites with the formula MFe_2O_4 (M= Mn, Mg, Zn, Co, Ni, Fe) with a face-centered cubic unit cell contain eight formula units (see Figure 1.13). Two sites, the tetrahedral A site and the octahedral B site, are available for cation occupation. A variety of size-dependent changes are observed with spinel ferrite nanocrystals. For example, a blocking behavior

has been observed in $CoFe_2O_4$ [35] and $MnFe_2O_4$ [36]. The expected fall in coercivity with size occurs in most spinel ferrite nanoparticles. Depending on the method of preparation, the nanoparticles exhibit different properties due to differences in the cation occupancy. Locations of the trivalent and bivalent cations affect the magnetic exchange interaction markedly, leading to differences in the magnetic properties. $CoFe_2O_4$ nanoparticles exhibit a blocking temperature 150K higher than the Mn ferrite nanoparticles [37]. Tetragonal $CoMn_2O_4$ nanocrystals (5–12nm diameter) prepared by the decomposition of Co–Mn acetylacetonate in oleylamine are ferromagnetic at low temperature and paramagnetic at room temperature, with a blocking temperature of 30–40 K. Magnetic properties such as the saturation magnetization also exhibit size-dependent changes at the nanoscale. The saturation magnetization of nanocrystals is less than that of the corresponding bulk, because of the dead layer on the surface [38].

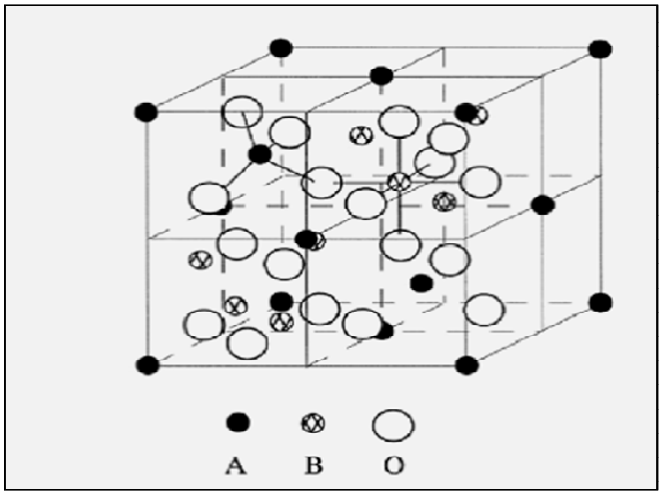

Figure 1.13. Unit cell of spinel ferrites .In certain cases, the surface layer makes nanoparticle behave like a spin glass [39].

1.3 Preparation of Nanoparticles

The various approaches to synthesizing nanomaterials can be roughly categorized into “top-down” methods or “bottom-up” methods [Fig.1.14] [40]. Top-down methods include mechanical attrition of a bulk material, by ball-milling for instance, until the dimensions of the material are sufficiently small. While this method can produce large quantities of material, there are impurity problems as well as size polydispersity and other control issues. Bottom-up, however, approaches involve the creation of material

from precursor chemicals or materials via chemical, thermal or other reactions. The general technique involves the nucleation and growth of a new phase from a liquid, solid or gas phase. Some examples include vapor phase deposition methods, phase transformation in mixtures and a wide variety of solution based chemical approaches both in aqueous and organic solvents. These bottom-up approaches make use of thermodynamic and kinetic controls to create particles of controlled size and shape and composition. Additionally, impurities are less of a concern, composite materials such as core-shell nanoparticles can be synthesized and self-assembly of particles can be induced, all of which are difficult with top-down methods. Many of the solution based techniques are also scalable to make large quantities of material, either in batch mode or continuous flow.

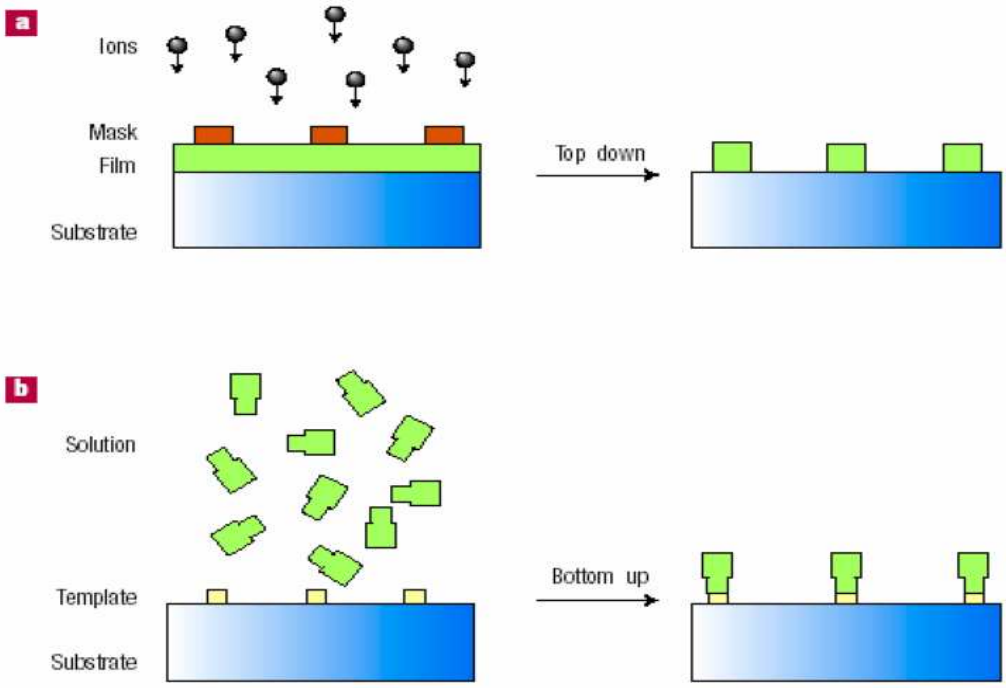

Figure 1.14. Preparation methods of nanoscale materials. (a) In a top-down process, materialis removed from a monolithic entity resulting in the nanostructure. (b) In a bottom-up process, building-blocks self-organize to form the nanostructure [40].

The top-down and bottom-up approaches can also be considered as physical and chemical methods, respectively [8]. Figure 1.15 illustrates both approaches [41].

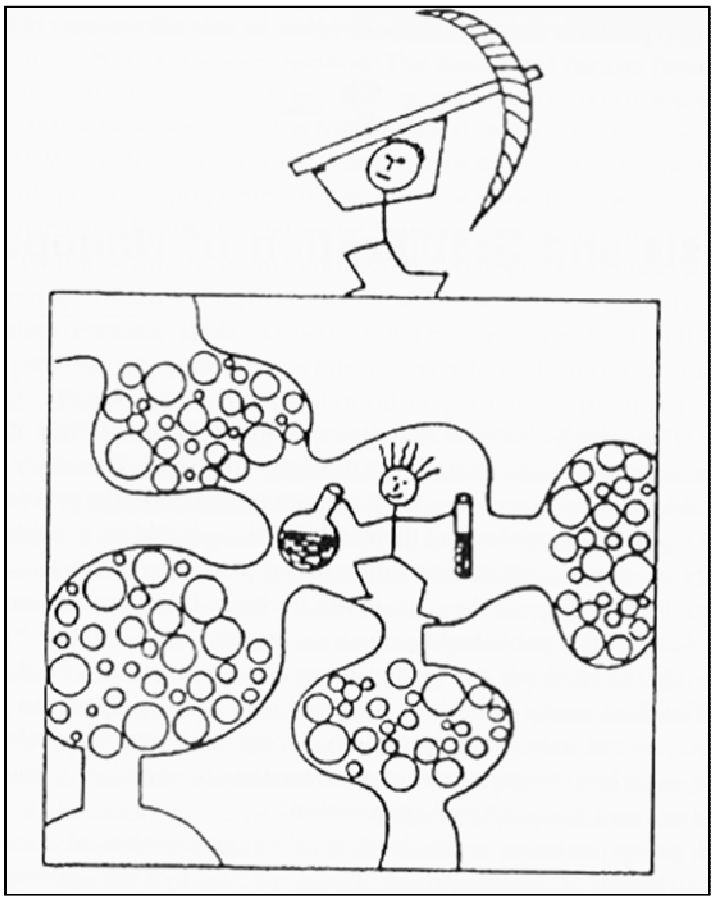

Figure 1.15. Two approaches to the synthesis of nanoparticles. A comparision of nanochemistry and nanophysics [41].

1.3.1 Physical Methods

Many of the physical methods involve the evaporation of a solid material to form a supersaturated vapor from which homogenous nucleation of nanoparticles occurs. In these methods, the size of the particles is controlled by temporarily inactivating the source of evaporation, or by slowing the rate by introducing gas molecules to collide with the particles. The growth generally occurs rapidly, from milliseconds to seconds, requiring a precise control over experimental parameters. Several specialized techniques have been developed in the last few decades and they can be classified on the basis of the energy source and whether they make use of solid or liquid (vapor) precursors [42]. Figure 1.16 provides a summary of nanoparticles synthesized by physical methods.

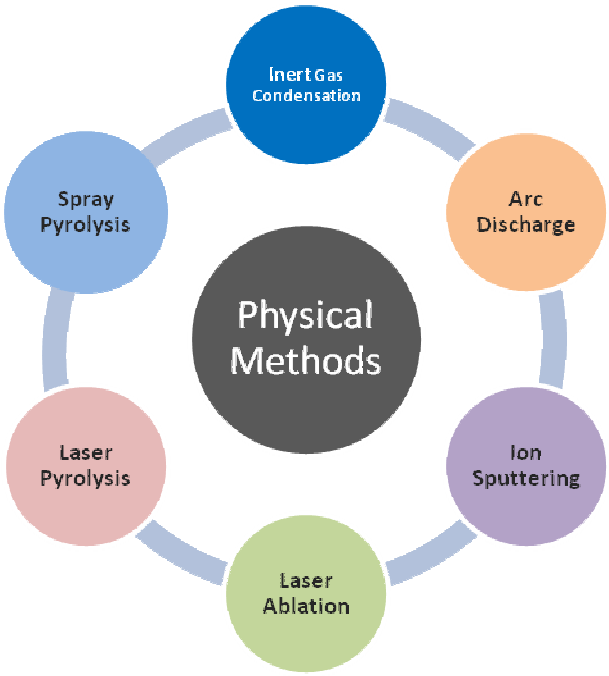

Figure 1.16. Schematically illustration of physical methods of synthesizing nanoparticles.

1.3.2 Chemical Methods

Chemical methods have emerged to be indispensable for synthesizing nanocrystals of various types of materials. These methods are generally carried out under mild conditions and are relatively simple. Nanodimensional materials in the form of embedded solids, liquids, and foams have also been prepared by chemical means and such materials have been in use for some time.

There are several reviews in the literature focusing on the synthesis of nanocrystals [43, 44]. Any chemical reaction resulting in a sol consists of three steps - seeding, particle growth, and growth termination by capping. An important process that occurs during the growth of a colloid is Ostwald ripening (Figure 1.17). Ostwald ripening is a growth mechanism whereby smaller particles dissolve releasing monomers or ions for consumption by larger particles, the driving force being the lower solubility of larger particles [45].

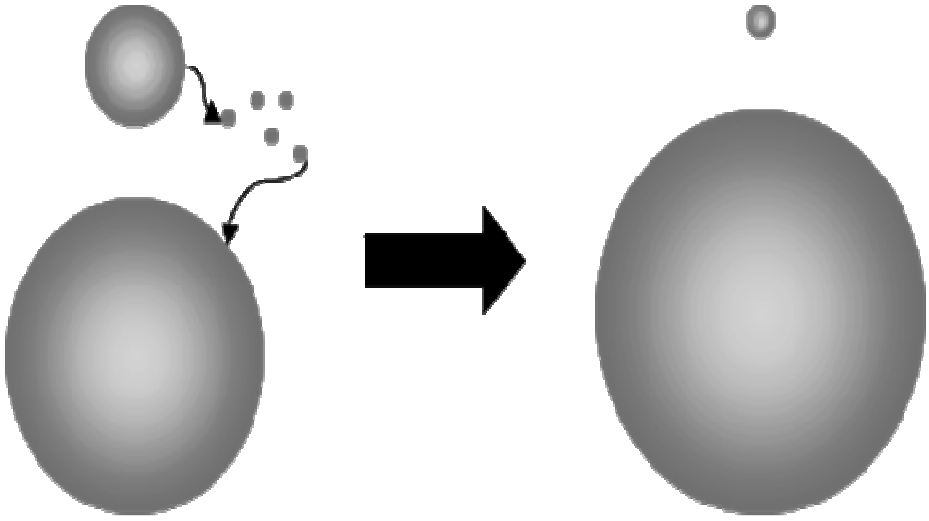

Figure 1.17. Ostwald ripening [45].

Ostwald ripening limits the ultimate size distribution obtainable to about 15% of the particle diameter when the growth occurs under equilibrium conditions. However, by employing high concentrations of the monomers and capping agents, growth can be forced to occur in a transient regime. The seeding, nucleation, and termination steps are often not separable and one, therefore, starts with a mixture of the nanocrystal constituents, capping agents, and the solvent. The relative rates of the steps can be altered by changing parameters such as concentrations and temperature. This is the common trick employed to obtain nanocrystals of different dimensions from the same reaction mixture. One of the important factors that determine the quality of a synthetic procedure is the monodispersity of the nanocrystals obtained. It is desirable to have nanoparticles of nearly the same size, in order to be able to relate the size and the property under study. Hence, narrower the size distribution, more attractive is the synthetic procedure. The best synthetic schemes today produce nanocrystals with diameter distribution of around 5%. The other important issues are the choice of the capping agent and control over the shape.

Sols produced by chemical means can either be in aqueous media (hydrosols) or in organic solvents (organosols). Organosols are sterically stabilized, while hydrosols can either be sterically or electrostatically stabilized. Steric stabilization of hydrosols can be brought about by the use of polymers as stabilizing agents. Natural polymers such as starch and cellulose, synthetic polymers, such as polyvinyl pyrrolidone (PVP),

polyvinyl alcohol (PVA), and polymethyl vinylether are used as stabilizing agents. Unlike text-book colloids such as India ink and dust in river beds, sterically stabilized sols are redispersible. The nanoparticulate matter in the sols can be precipitated by various means, filtered and dissolved again in a solvent. Redispersibility of the particles is an important characteristic of great utility. Furthermore, metal nanocrystals in a sterically stabilized sol can be dispersed in high concentrations. As a general rule, organic solvents provide better control over the size of the nanocrystals [8].

1.3.2.1 Metal Nanocrystals by Reduction

A variety of reducing agents are used to reduce soluble metal salts to obtain then corresponding metals. By concluding the growth with suitable surfactants or ions, metal nanoparticles are produced. Some representative reducing agents are shown below (Fig.1.18):

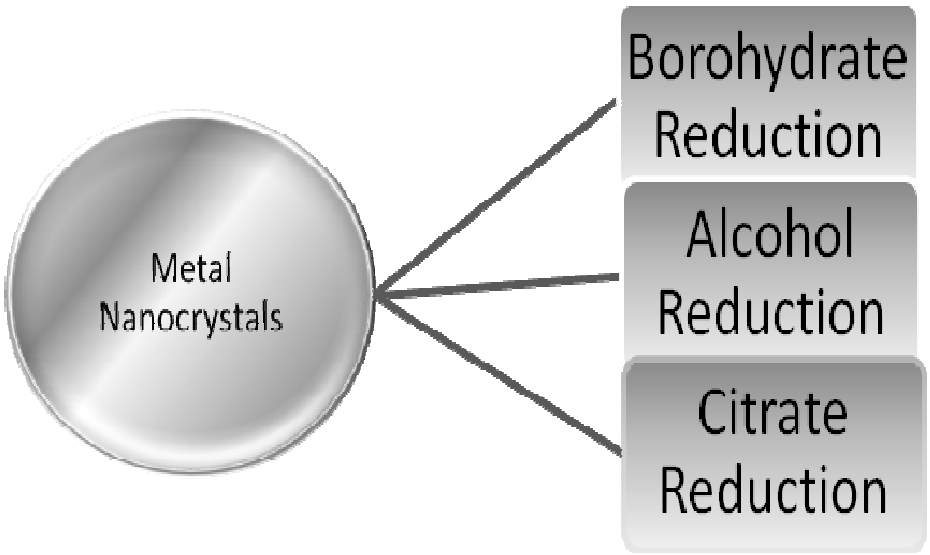

Figure 1.18. Some Reducing Agents to synthesize nanocrystals.

1.3.2.1.1 Borohydrate Reduction

Nanocrystals of a variety of metals have been made by borohydride reduction. Thus, Pt nanocrystals with mean diameter 2.8 nm were prepared by the reduction of chloroplatinic acid with sodium borohydride [46]. And there is a study about the

synthesis of metal nanoparticles within dendrimer templates. The composites are prepared by mixing of the dendrimer and metal ion, and subsequent chemical reduction. These materials can be immobilized on electrode surfaces where they serve as electrocatalysts or dissolved in essentially any solvent (after appropriate end-group functionalization) as homogeneous catalysts (Fig.1.19) [47].

Schiffrin and coworkers [48] developed a two-phase method to reduce noble metals. This method, popularly known as the Brust method, has been widely used to prepare organosols. In this method, aqueous metal ions are transferred to a toluene layer by the use of tetraoctylammonium bromide, a phase transfer catalyst which is also capable of acting as a stabilizing agent. The Au complex transferred to toluene is reacted with alkanethiols to form polymeric thiolates. Aqueous borohydride is added to this mixture to bring about the reduction that is modulated by the interface of toluene and water. The thiol molecules also serve as capping agents. The capping action of the thiols is related to the formation of a crystalline monolayer on the metal particle surface. The length of the alkane chain and the concentration of borohydride affect the size of the nanocrystals obtained by the Brust method.

Sun and coworkers [49] have used lithium triethylborohydride ($LiBEt_3H$, also called superhydride) to reduce Co chloride in a solvent mixture consisting of oleic acid and an alkylphosphine. The alkylphosphine serves as a capping agent as well. The size of the nanocrystals could be tuned by varying the chain length of the alkylphosphine.

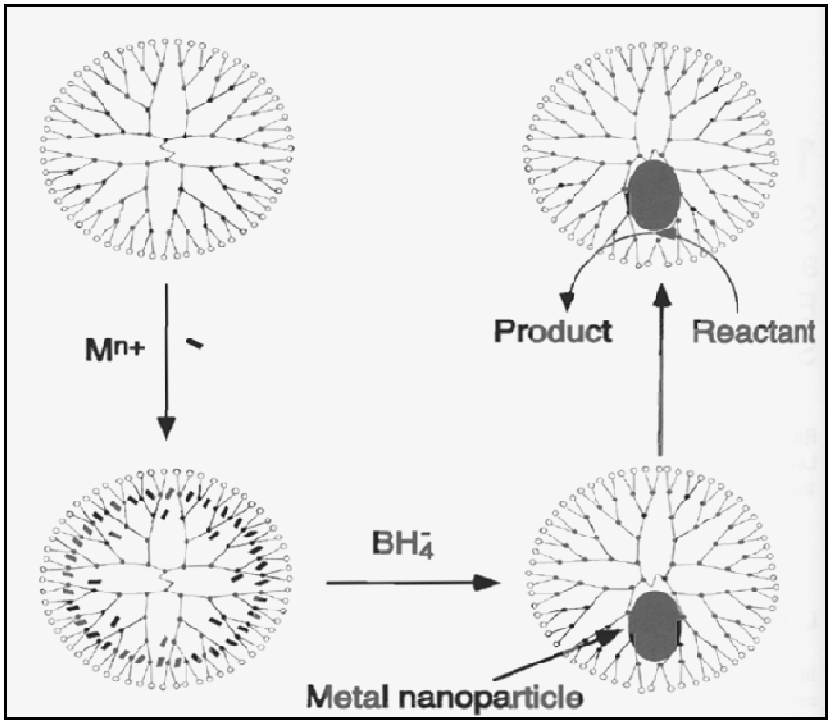

Figure 1.19. Schematic of the synthesis of metal nanoparticles within dendrimer templates [47].

1.3.2.1.2 Alcohol Reduction

The ability of small metal particles in catalyzing the oxidation of alcohols to aldehydes or acids has long been known in organic chemistry. The fine metal particles that catalyse these reactions get reduced during the course of the reaction and are deposited as spongy precipitates. This reaction is further catalyzed by a base and requires the presence of α-hydrogen in the alcohol [8]. By making use of polymeric capping agents such as PVP, the growth of metal particles can be arrested. Palladium acetate refluxed with ethanol in the presence of PVP yields Pd nanocrystals of 6.0nm diameter [50].

1.3.2.1.3 Citrate Reduction

Synthesis by the citrate method involves the addition of chloroauric acid to a boiling solution of sodium citrate. A wine red color indicates the beginning of reduction. The average diameter of the nanoparticles can be varied over a range of 10–

100 nm by varying the concentration ratio between chloroauric acid and sodium citrate [8].

1.3.2.2 Solvothermal Synthesis

The solvothermal method provides a means of using solvents at temperatures well above their boiling points, by carrying out the reaction in a sealed vessel. The pressure generated in the vessel due to the solvent vapors elevates the boiling point of the solvent. Typically, solvothermal methods make use of solvents such as ethanol, toluene, and water, and are widely used to synthesize zeolites, inorganic open-framework structures, and other solid materials. In the past few years, solvothermal synthesis has emerged to become the chosen method to synthesize nanocrystals of inorganic materials. Numerous solvothermal schemes have been employed to produce nanocrystalline powders as well as nanocrystals dispersible in a liquid [51].

A surfactant-assisted solvothermal procedure has been employed to prepare PbS nanocrystals at 85 ^{o}C. Other nanostructures are also obtained by this preparation [52]. A solvothermal reaction in the presence of octadecylamine yields monodisperse PbSe nanocrystals of controllable size [53].

By using surfactants such as cetyltrimethylammonium bromide (CTAB), the size of the nanocrystals could be controlled. CoO nanoparticles with diameters in 4.5–18 nm range have been prepared by the decomposition of cobalt cupferronate in decalin at 270 ^{o}C under solvothermal conditions. Cubic and hexagonal CoO nanocrystals have also been obtained starting from $Co(acac)_3$ [54].

1.3.2.3 Photochemical Synthesis

Photochemical synthesis of nanoparticles is carried out by the light-induced decomposition of a metal complex or the reduction of a metal salt by photo generated reducing agents such as solvated electrons. The former is called photolysis and the latter radiolysis. PVP-covered Au nanocrystals are produced by the reduction of HAuCl4 in formamide by UV-irradiation [55].

1.3.2.4 Electrochemical Synthesis

Reetz et al. [56] has pioneered the electrochemical synthesis of metal nanocrystals. Their method represents a refinement of the classical electrorefining

process and consists of six elementary steps they are oxidative dissolution of anode, migration of metal ions to the cathodes, reduction of ions to zero-valent state, formation of particles by nucleation and growth, arrest of growth by capping agents, and precipitation of particles. The steps are schematically illustrated in Figure 1.20. The capping agents are typically quaternary ammonium salts containing long-chain alkanes such as tetraoctylammonium bromide. The size of the nanocrystals could be tuned by altering the current density, the distance between the electrodes, the reaction time, the temperature, and the polarity of the solvent. Thus, using tetraoctylammonium bromide as stabilizer, Pd nanocrystals in the size range of 1–5nm have been obtained. Low current densities yield larger particles (~ 4.8 nm) while large current densities yield smaller particles (~ 1.4 nm). Larger Pd nanoparticles stabilized by the solvent (propylene carbonate) have also been obtained. This method has been used to synthesize Ni, Co, Fe, Ti, Ag, and Au nanoparticles [8].

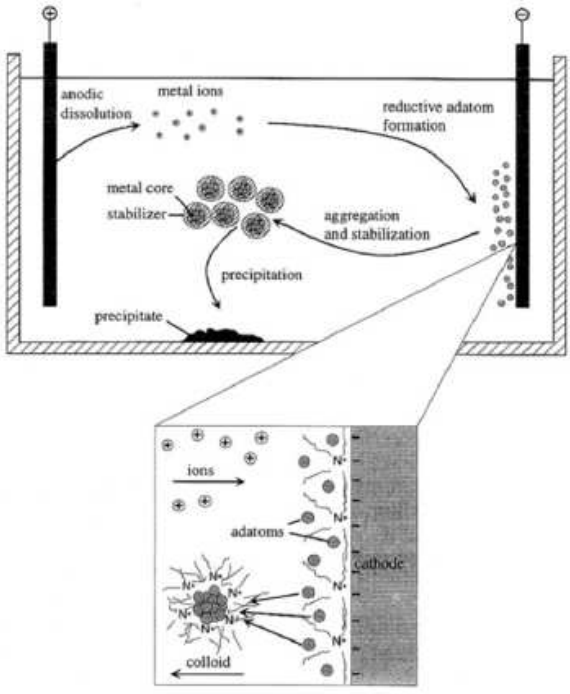

Figure 1.20. Schematic illustration of the steps involved in the electrochemical reduction of metalnanocrystals by the Reetz method [8].

1.3.2.5 Thermolysis Routes

Thermolysis routes are related to chemical vapor deposition (CVD)-based methods to prepare thin films. By carrying out thermolysis reactions in high boiling solvents in the presence of capping agents, nanocrystals of various materials are obtained. Thermal decomposition provides remarkable control over size and is well suited for scale up to gram quantities. Various metal nanoparticles have been prepared by the method. By using capping agents such as carboxylic acids and alkyl amines the size of the nanoparticles can be tuned to be in the range of 3–20nm [57].

Nanocrystals of metal oxides are prepared by controlled oxidation of the corresponding metal particles. Alivisatos and coworkers [58] prepared metal oxide nanoparticles by the decomposition of cupferron complexes in trioctylamine solution containing octylamine. Cupferron (*N*-nitrosophenylhydroxylamine) is a versatile ligand that forms complexes with several transition metal ions. By using this method, nanoparticles of Mn_3O_4 [58], Fe_3O_4 [59] and Co_3O_4 [59] have been made.

1.3.2.6 Sonochemical Routes

Various methods have been discussed in the literature for the sonochemical synthesis of nanosized particles. In order to carry out sonochemical reactions, a mix of reagents dissolved in a solvent is subjected to ultrasound radiation (20 kHz–10 MHz). Acoustic cavitation leads to the creation, growth, and collapse of bubbles in the liquid medium. The creation of bubbles is due to the suspended particulate matter and impurities in the solvent. The growth of a bubble by expansion leads to the creation of a vacuum that induces the diffusion of volatile reagents into the bubble. The growth step is followed by the collapse of the bubble which takes places rapidly accompanied by a temperature change of 5,000–25,000K in about a nanosecond. Collapse of the bubble triggers the decomposition of the matter within the bubble. The rapid cooling rate often hinders crystallization, and amorphous products are usually obtained. The collapse of the bubble does not signal the end of the reaction. The collapse is frequently accompanied by the formation of free radicals that cause further reactions. A few of the sonochemical reactions are, in fact, mediated by free radicals [8].

The introduction of alcohols in the reducing mixture, enhances the rate of formation of the Au particles [60]. At high alcohol concentrations, smaller nanoparticles are formed. A mechanism based on the ability of alcohols to scavenge the H and the OH radicals has been proposed to account for these observations. Increasing the hydrophobicity of alcohols reduces the size of the nanoparticles due to the increasing ability of the hydrophobic alcohols to cap the produced nanoparticles [8].

1.3.2.7 Michelles and Microemulsions

Reverse or inverted micelles formed by the dispersion of water in oil, stabilized by surfactants are useful templates to synthesize nanoscale particles of metals, semiconductors, and oxides [61]. This method relies on the ability of surfactants in the shape of truncated cones (like cork stopper), to trap spherical droplets of water in the oil medium, and thereby forming micelles. A micelle is designated inverse or reverses when the hydrophilic end of the surfactant points inward rather than outward as in a normal micelle. The dimensions of the water droplet can be suitably altered by changing the concentration of the surfactant and water. An inverted micelle is also called a microemulsion if larger water droplets are present.The mechanism associated with the formation of nanoparticles by the microemulsion technique is schematically described in Fig.1.21. Conceptually, one makes two reactants A and B in the aqueous phases (droplets) of two different W/O microemulsions (Fig 1.21a). When mixed (Fig 1.21b), because of collision and coalescence of the droplets, reactants A and B are exchanged between the water droplets. This interchange of the reactants is very fast, so that for the most commonly used microemulsions it occurs just during the mixing process. As the reactants come in contact with each other, they react and form precipitate AB (Figure 1.21c) [14].

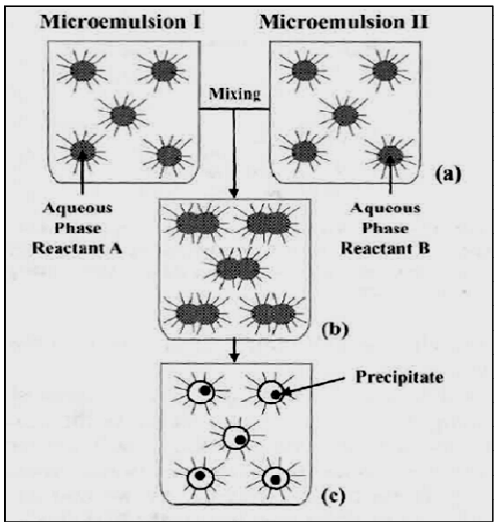

Figure 1.21. Schematic diagram showing the mechanism of formation of nanoparticles withmicroemulsion technology [14].

Moumen and coworkers [62] have pioneered the use of oil in water micelles to prepare particles of $CoFe_2O_4$, γ-Fe_2O_3, and Fe_3O_4. The basic reaction involving hydrolysis is now templated by a micellar droplet. The reactants are introduced in the form of a salt of a surfactant such as SDS. Thus, by adding CH_3NH_3OH to a micelle made of calculated quantities of $Fe(SDS)_2$ and $Co(SDS)_2$, nanoparticles of $CoFe_2O_4$ are obtained. By increasing the concentration of metal salts, the size of the nanoparticles can be increased [63].

1.3.2.8 The Liquid- liquid Interface

Rao and coworkers [64] have used reactions taking place at the interface of two liquids such as toluene and water to produce nanocrystals and films of metals, semiconductors, and oxides. In this method, a suitable organic derivative of the metal taken in the organic layer reacts at the interface with the appropriate reagent present in the aqueous layer to yield the desired product. For example, by reacting $Au(PPh_3)Cl$ in toluene with THPC in water, nanocrystals of Au can be obtained at the interface of two liquids. This method has been extended to prepare nanocrystals of Ag and Pd, Au–Ag alloys, semiconducting sulphides such as CdS, ZnS, and CoS, and oxides such as Fe_2O_3 and CuO (Figure 1.22) [64b-64e]. By varying parameters such as the reaction

temperature, and the reactant concentrations, the size of the nanocrystals and the coverage of the films can be modified. Thus, a change in the reaction temperature from 298 to 348 K, increases the size of Au nanocrystals from 7 to 16nm [64e].

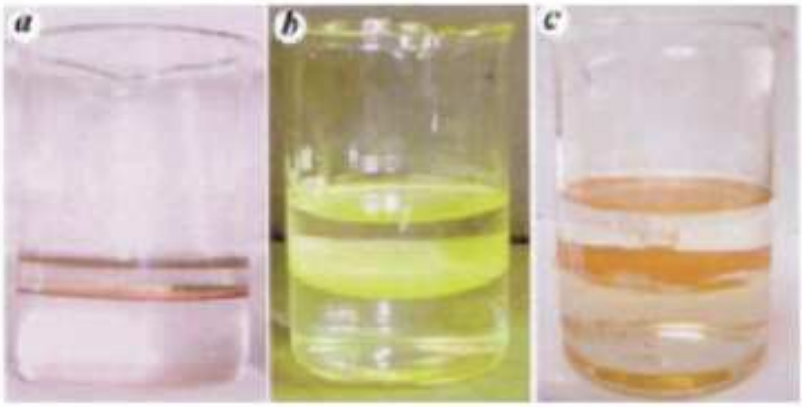

Figure 1.22. Nanocrystals of: (**a**) Au, (**b**) CdS, and (**c**) γ–Fe_2O_3 formed at the toluene water interface [64].

1.3.3 Size Tuning

In the case of crystalline nanoparticles with a size in the range of 3 to 10 nm and consisting of ~10^2 to 10^4 atoms, nearly continuous size tunability is possible, as an addition or removal of a unit cell requires only a small variation of the nanocrystal free energy. The method used to control the size depends on peculiarities of the concrete synthesis. For instance, $MnFe_2O_4$ nanoparticles with a rather narrow size distribution can be synthesized inside water-in-toluene reverse micelles playing in the role of nanoreactors. The size of micelles depends on the water-to-toluene volume ratio and determines the size of spinel ferrite nanoparticles [65]. Any synthesis of colloidal particles employing soluble precursors involves two consecutive stages: nucleation and growth [66]. The narrow size distribution of the resulting nanocrystals can be achieved only if the nucleation stage is temporally separated from the further growth. The nuclei grow by consuming dissolved molecular species (monomers) from the surrounding solution. When all molecular precursors are consumed, the reaction mixture has two scenarios for further evolution. If the addition of a monomer to a nanocrystal is a reversible process (i.e., a nanocrystal can both consume and release the monomer), the nanocrystals grow via the so-called [67].

A typical colloidal organometallic synthesis is carried out as shown in Figure 1.23 on an example of $CoPt_3$ nanocrystals [68].

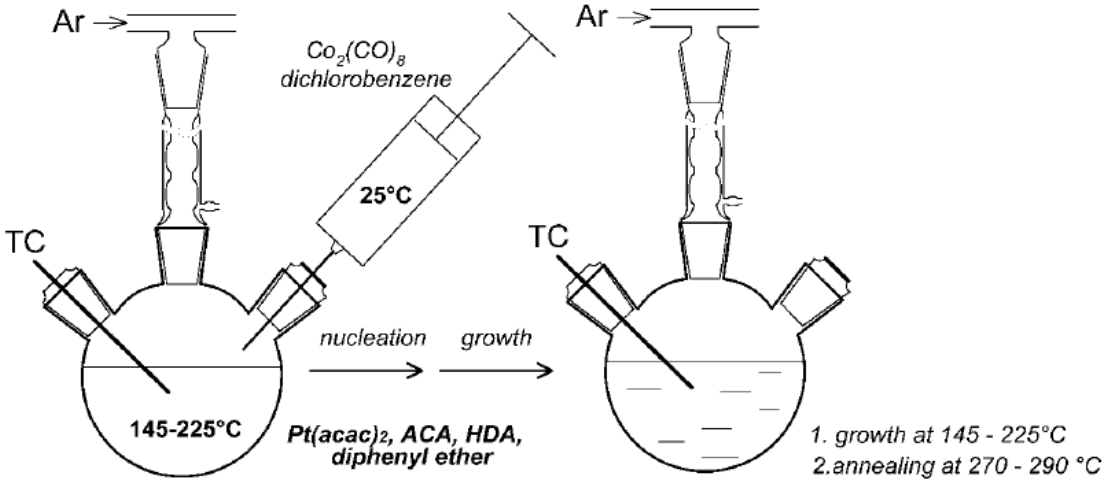

Figure 1.23. Organometallic synthesis of $CoPt_3$ nanocrystals [68].

Ostwald ripening, when smaller particles evolve monomers and dissolve, whereas larger particles consume monomers and grow. If the transformation of molecular precursors to nanoparticles is irreversible, no changes of the particle size via Ostwald ripening is possible and the reaction comes to saturation. If the first scenario is realized, the Ostwald ripening provides a possibility of a slow and controllable increase of the mean particle size in the course of heating. Moreover, Ostwald ripening of nanometer-sized particles results in much narrower size distributions than those observed for micrometer-sized particles. If the Ostwald ripening in a given system is impossible or very slow, the tuning of the nanocrystal size can be achieved only by control over nucleation and growth rates, as illustrated in Figure 1.24. Fast nucleation provides a high concentration of nuclei, finally yielding smaller nanocrystals, whereas slow nucleation provides a low concentration of seeds consuming the same amount of monomer, resulting in larger particles [67].

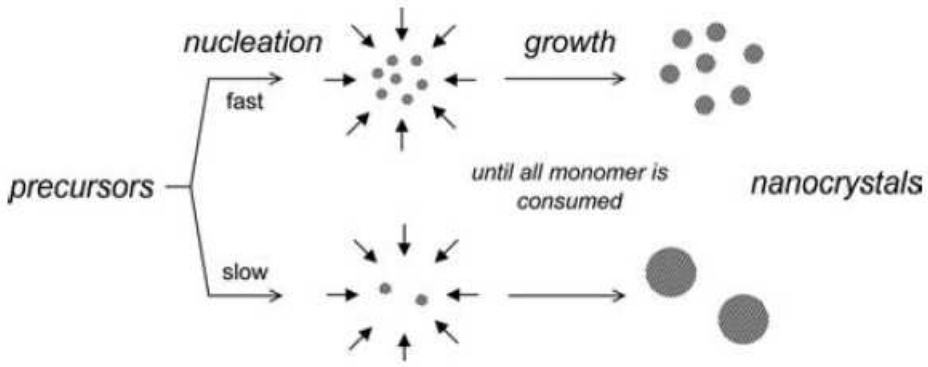

Figure 1.24. Synthesis of nanoparticles in the absence of Ostwald ripening [67].

1.3.3.1 Effect of Heating Time

The influence of the reaction time on the size of magnetic nanocrystals is studiedseveral works. For practically important FePt and $CoPt_3$ magnetic alloy nanocrystals, no pronounced influence of the reaction time on size was found (Figure 1.25). FePt and $CoPt_3$ nanocrystals were prepared via organometallic route in OA–oleyl amine and ACA–HDA coordinating mixtures, respectively. In contrast, prolonged heating resulted in progressive decomposition of the stabilizing agent molecules rather than in nanocrystal growth [67].

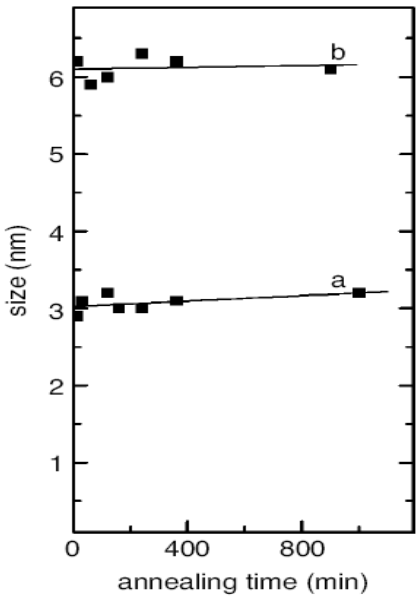

Figure 1.25. Dependence of FePt (a) and $CoPt_3$ (b) nanocrystal size on duration of heating during the synthesis [67].

1.3.3.2 Effect of Reaction Temperature

The reaction temperature affects both the nucleation and the growth rates in any colloidal synthesis of nanocrystals. In the absence of Ostwald ripening, the variation of the reaction temperature was used for tuning the size of Co nanocrystals. An increase of the nanocrystal size, with an increase in the reaction temperature from 170 to 200°C, was observed for Co nanocrystals [69]. The opposite behavior was reported for Co nanocrystals prepared via thermal decomposition of $Co_2(CO)_8$ [70].

A detailed study on the dependence of nanocrystal size on the reaction temperature was performed for $CoPt_3$ magnetic alloy nanocrystals (Figure 1.26 and Figure 1.27). An increase of temperature from 145 to 220 °C led to a decrease of average final particle size from ~10 to 3 nm. This can be explained by taking into account the temperature dependencies of the nanocrystal nucleation and growth rates. The activation energy for the nucleation process is usually much higher than that for the particle growth, which makes the nucleation rate more sensitive to changes in temperature than the growth rate. The reaction temperature can thus be used to adjust the balance between nucleation and growth rates. At higher temperatures, more nuclei are formed and the final particle size is smaller (Fig.1.26).

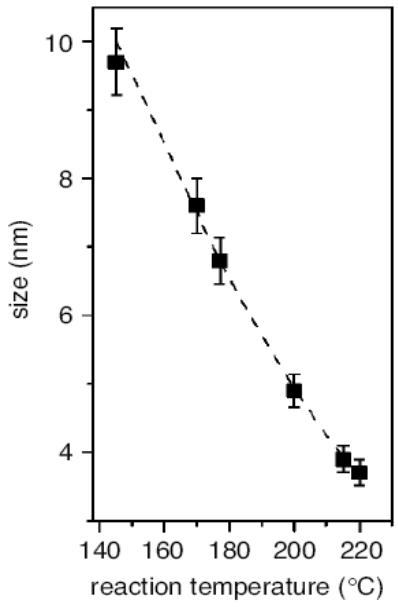

Figure 1.26. Dependence of $CoPt_3$ nanocrystal size on the reaction temperature [67].

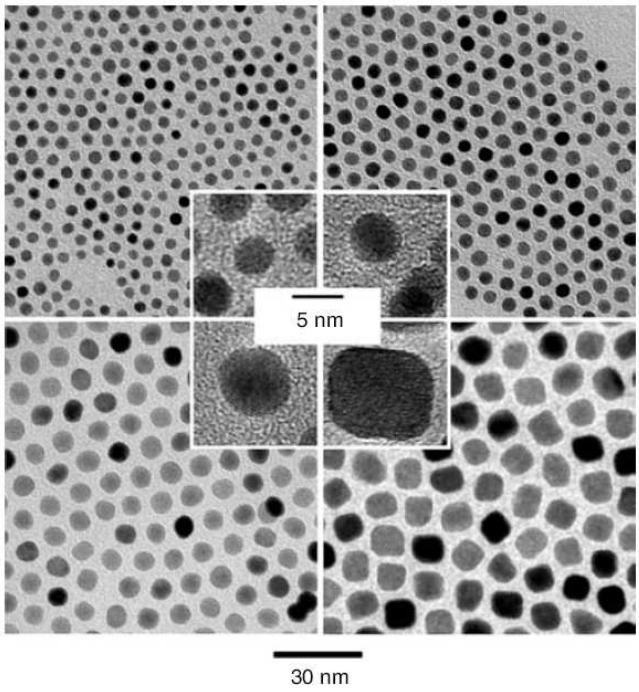

Figure 1.27. TEM and HRTEM images showing effect of the reaction temperature on the mean size and size distribution of $CoPt_3$ nanocrystals: 3.7-, 4.9-, 6.3-, and 9.3 nm large particles were prepared at 220, 200, 170 and 145°C, respectively [67].

1.1.4 Shape Control of Nanoparticles

The ability to grow nanocrystals of controlled shapes adds an significant dimension to the tuning of nanoscalar properties. In addition to size-dependent properties, nanomaterials have shape-dependent properties.

Synthetic schemes make use of templates or seeds to influence the growth process. The seed-mediated method has been adapted to produce nanorods [71], nanowires [72], and other shapes. The method involves two steps. In the first step, small citrate capped Au or Ag nanocrystals are produced by borohydride reduction for use as seeds. In the second step, the particles are introduced into a solution containing the metal salt, CTAB (a structure directing agent), and a mild reducing agent such as ascorbic acid. The use of a mild reducing agent is the key to achieve seed-mediated growth. Under the reaction conditions, ascorbic acid is not sufficiently powerful to reduce the salt on its own. In the presence of seeds, reduction mediated by the seed occures producing nanorods [71] and nanowires [72]. A TEM image of Au nanorods

produced by this method is revealed in Figure 1.28. The nanorod and nanowire structures are directed by the micellar structures adopted by CTAB. The chain length of the structure-directing agent plays an important role in determining the aspect ratio of the rod-shaped particles [72b]. The presence of a small quantity of organic solvents leads to the formation of needle shaped crystallites [72c]. Addition of NaOH to the reaction mixture before reduction brings about dramatic changes in the product morphology. Hexagons, cubes, and branched structures have been produced by using NaOH and varying the experimental parameters (Figure 1.29) [73]. In the experiment, the concentration of CTAB increases from 1.6 $\times 10^{-2}$M (A) to 9.5 $\times 10^{-2}$ M (B, C, D). [Au^{3+}] decreases from (B) to (C), whereas the seed concentration increases from C to D.

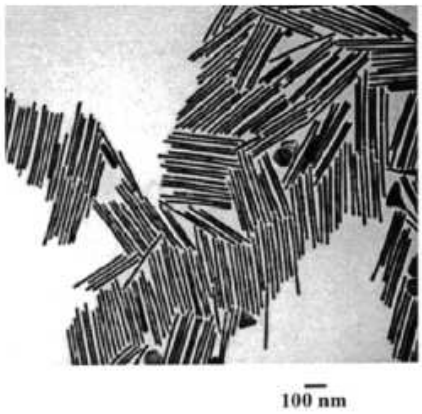

Figure 1.28. TEM image of Au nanorods prepared by the seed mediated growth method [73].

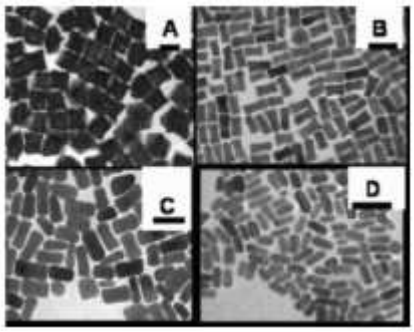

Figure 1.29. TEM images showing cubic to rod-shaped gold particles produced with low concentrations of ascorbic acid in the presence of a small quantity of silver nitrate, by seed-mediated growth method [73].

1.4 Magnetic Nanoparticles (MNPs)

Magnetic nanoparticles (MNPs) have been the focus of an increasing amount of the recent literature, which was chronicled research into both the fabrication and applications of MNPs. The explosion of research in this area is driven by the extensive technological applications of MNPs which includes single-bit elements in high-density magnetic data storage arrays, magneto-optical switches, and novel photoluminescent materials. In biomedicine, MNPs serve as contrast enhancement agents for Magnetic Resonance Imaging, selective probes for biomolecular interactions, and cell sorters. Nanoparticles of magnetic metals are also finding applications as catalysts, nucleators for the growth of high-aspect- ratio nanomaterials, and toxic waste remediation. Methodologies for the synthesis of MNPs are being developed by scientists working in the fields spanning Biology, Chemistry, and Materials Science. In the last decade, these efforts have provided access to nanoscale magnetic materials ranging from inorganic metal clusters to custom-built Single Molecule Magnets [74].

1.4.1 Synthesis of MNPs

An ideal synthesis of nanocrystals has to provide the achievement of desired particle sizes over the largest possible range, narrow size distributions, high crystallinity, control of shape, and desired surface properties. For potential application of nanocrystals, a relatively low cost of the final product becomes an additional requirement. Numerous methods such as vacuum deposition techniques, chemical vapor deposition, normal incidence pulsed laser deposition colloidal syntheses utilizing thermal or sonochemical, decomposition of organometallic precursors, high-temperature reduction of metal salts, and chemical reactions inside reverse micelles have been applied for preparation of magnetic metal nanoparticles [Fig.1.30].

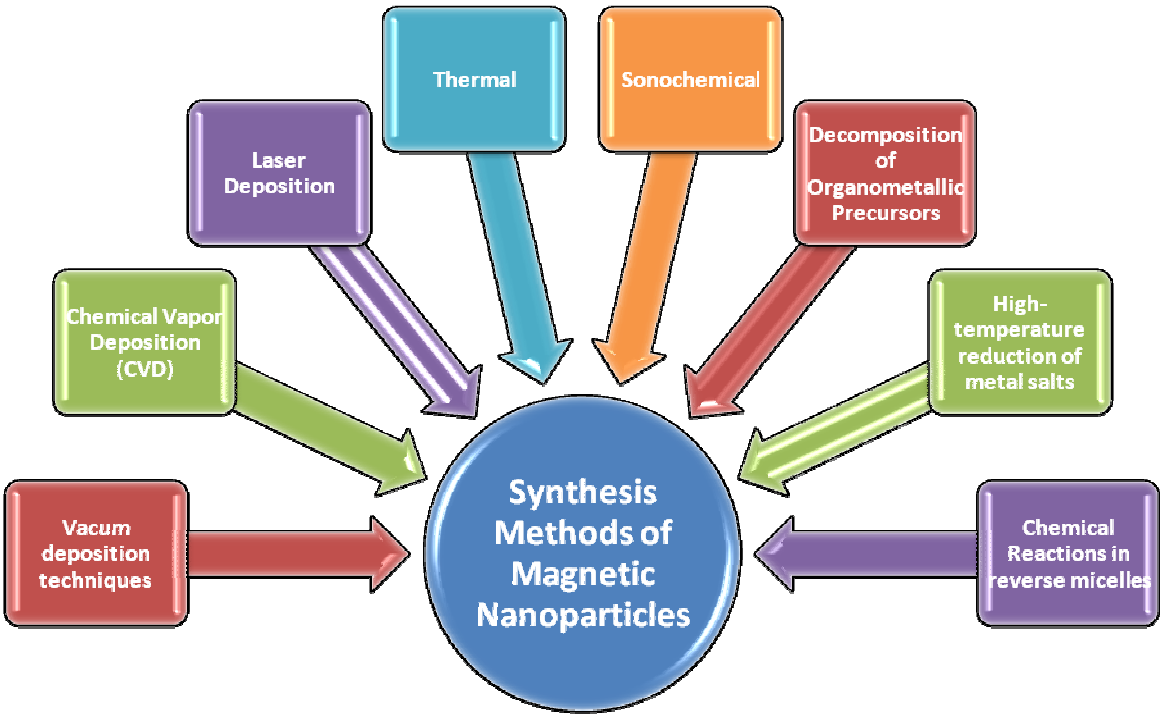

Figure 1.30. Schematically illustration of synthesizing methods of MNPs.

1.4.1.1 Synthesis of Single Metal MNPs

Solution phase synthesis of transition metal nanoparticles is accomplished via two generic pathways: the reduction of metal salt or decomposition of an organometallic complex. Two of the largest concerns regarding MNP synthesis are the ability to both tune the size of the nanoparticle and control particle size dispersity. In the case of metal ion reduction, successful strategies include conducting the reaction in a confined environment or in the presence of of a suitable capping ligand. For the case of organometallic decomposition, size control and dispersity is usually attained by conducting the reactions at high temperature, which ensures a high rate of nanoparticle nucleation and growth. Capping ligands, which form a self-assembled monolayer of the nanoparticle, can also be used to mediate particle growth.

Water-in-oil microemulsion (w/o microemulsion) and inverse micelles are often employed as nanoconfined reactors in the synthesis of many varieties of nanoparticles [75]. For both , the size of the confined space can be defined by varying the amounts of both surfactant and solvent, which allows for direct control over the size of resulting MNPs. Typically, MNP preparation in w/o microemulsions is achieved by mixing an emulsion containing metal salts with an emulsion containing a suitable reducing agent

($NaBH_4$ or N_2H_4). This produces surfactant capped metal nanoparticles with diameters of less than 10 nm (Figure 1.31). Similarly, aqueous solutions of reducing agents can be added to inverse micellar solutions of metal salts in nonpolar solvents. Using these methodologies, MNPs of Fe [76], Co [77], and Ni [78] have been prepared.

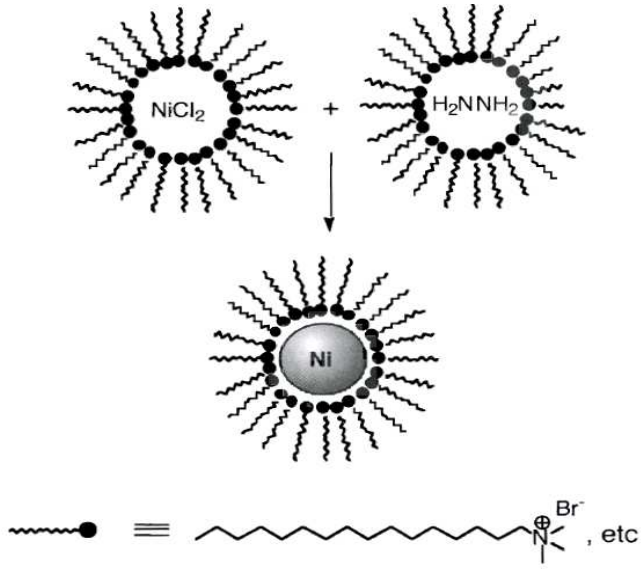

Figure 1.31. Example of the production of Ni MNPs by H_2NNH_2 reduction of $NiCl_2$ in a w/o microemulsion system [74].

Thermal decomposition of organometallic complexes is of great interest as many of the synthetic procedures produce highly monodisperse nanoparticles. Metal carbonyl complexes represent the most common organometallic precursor for this reaction Fe MNPs, for example, are produced by the thermal decomposition of $Fe(CO)_5$ in trioctylphosphine oxide (TOPO) solutions containing oleic acid, which acts to passivate the product nanoparticles (Figure 1.32a) [79]. Polymer-coated Fe MNPs have also been prepared by thermal decomposition of $Fe(CO)_5$ in the presence of poly (styrene) functionalized with tetraethylenepentamine [80]. Thermal decomposition of $Co_2(CO)_8$ in hot toluene solutions containing TOPO produces ε-Co MNPs [52]. Similar reactions carried out in *o*-dichlorobenzene in the presence of various ligands allows for MNPs morphological control (Fig.1.32b) [81].

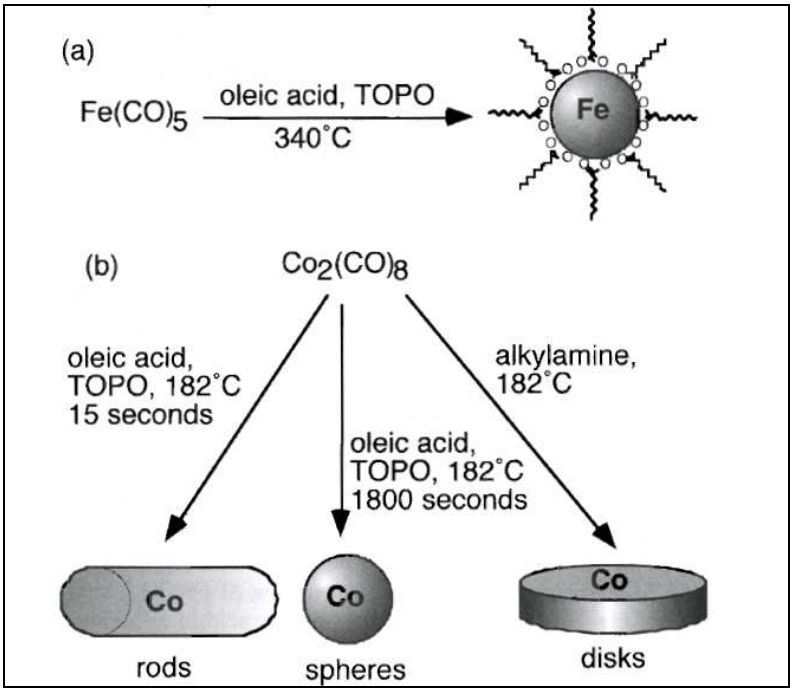

Figure 1.32. (a) Thermal decomposition of $Fe(CO)_5$ in the presence of oleic acid and TOPO to produce Fe MNPs and [79] (b) use of varying ligands to produce Co MNPs with spherical , rod, disk morphologies from $Co_2(CO)_8$ [81].

1.4.1.2 Synthesis of Alloyed Metal Nanoparticles

MNPs of alloyed transition metals can be prepared by reactions in which two metal precursors are decomposed in tandem, producing solid solution nanoparticles, or sequentially to give core-shell nanoparticles. The most heavily studied alloy MNPs are FePt and CoPt, both of which are interest for applications in data storage. FePt MNPs are prepared by simultaneous thermal decomposition of $Fe(CO)_5$ to Fe and polyol reduction of $Pt(acac)_2$ by 1,2-dodecanediol to Pt at 250 ^oC in solutions containing oleic acid and oleyl amine (Fig.1.33) [82]. This process yields monodisperse, solid solution FePt MNPs coated by a monolayer of oleyl amine and oleic acid that can be exchanged for shorter or longer acids or amines after synthesis. The composition of the MNP core can be controlled by varying the relative concentrations of the iron and platinum precursors. Further, the diameter of these MNPs can be adjusted between 3-10 nm.

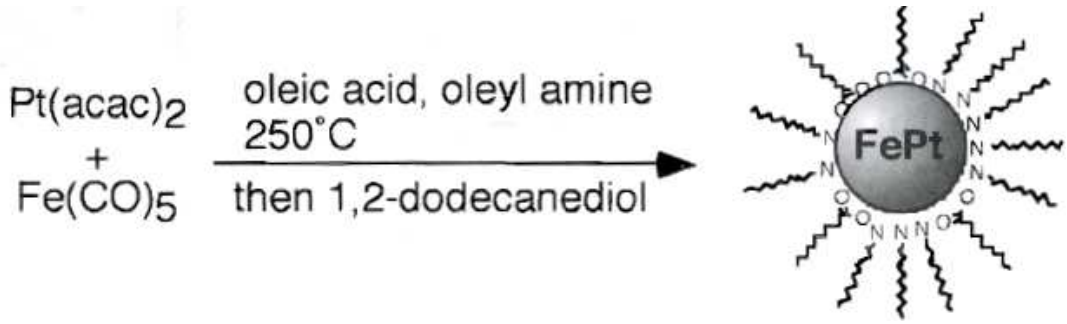

Figure 1.33. Synthesis of solid solution FePt MNPs [82].

1.4.1.3 Synthesis of Metal Oxide Nanoparticles

Ferrofluids, aqueous suspensions of iron oxide nanoparticles, are well known members of this class of MNPs. The iron oxide nanoparticles that comprise ferrofluids, typicallay Fe_3O_4 are prepared by either coprecipitation of mixtures of Fe^{2+} and Fe^{3+} ions in the presence of base or the precipitation/oxidation of Fe^{2+} ions by the action of base and oxidant (Figure 1.34) [74]. Recent advances in these techniques include the use of iron precursors which form micelles or synthesis within w/o microemulsions. These reactions produce MNPs resistant to agglomeration and allow for the synthesis of small (<10 nm diameter) nanoparticles with controllable size.

Figure 1.34. Aqueous preparative methods for synthesis of iron oxide MNPs [74].

1.4.1.4 Preparation of Bioconjugates MNPs

Many biomedical applications involve the conjugation of biomacromolecules to iron oxide MNPs. Amino crosslinked iron oxide (CLIO-NH_2) nanoparticles, iron oxide MNPs coated with crosslinked dextran and functionalized with amino groups, are the

most common strating material for the production of bioconjugated MNPs. The amine functionality is reached with heterobiofunctional crosslinking agents such as succinimidyl iodoacetate (Figure 1.35a) or N-succidinimidyl 3-(pyridyldithiol) propionate (Figure 1.35b), which then allows for the attachment of biomacromolecules. Amine functionality can also be introduced by sol-gel coating of MNPs with 3-aminopropyltrimethoxysilane, which can then be similarly derivitized [83]. Other methods for the production of bioconjugated or biocompatible MNPs include magnetoliposomes bearing functional groups in the lipid layer,direct adsorption of proteins onto the nanoparticle surface, and the coating the MNPs with nonionic surfactants.

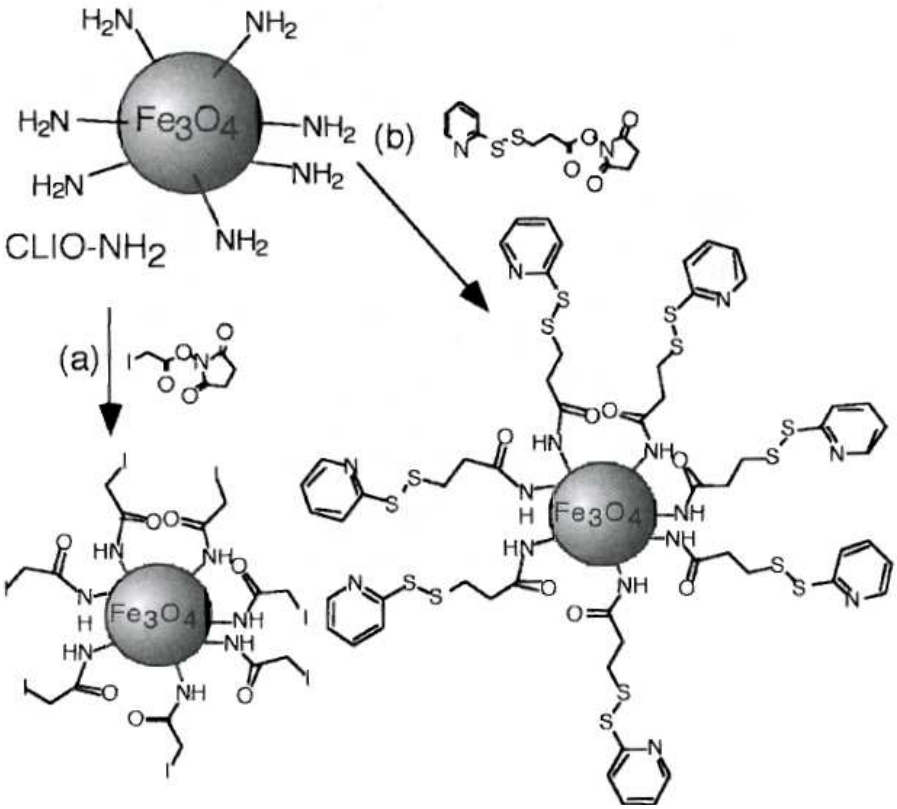

Figure 1.35. Reaction of CLIO-NH_2 with heterobifunctional crosslinkers, producing nanoparticles that are starting points for the creation of bioconjugated MNPs [83].

1.4.1.5 Biosynthetic Routes to MNPs

MNPs, typically iron oxide, are also common products of Nature's synthetic labotatories. For example, several bacteria are known to produce Fe_3O_4 nanoparticles encapsulated in a phoshpholipid bilayer (magnetoliposomes) Synthetic magnetoliposomes can be formed by coating iron oxide nanoparticle core. Here, Fe^{2+} and Fe^{3+} are first coprecipitated with base and stabilized by lauric acid. These particles are then coated with dimyristoylphosphateidylcholine (DMPC), producing the magnetoliposome (Fig.1.36a). Alternatively, preformed liposomes can be employed as microreactors in which Fe^{2+} is first sequestered inside of the liposome followed by the addition of base to produce iron oxide MNPs (Fig.1.36b) [74].

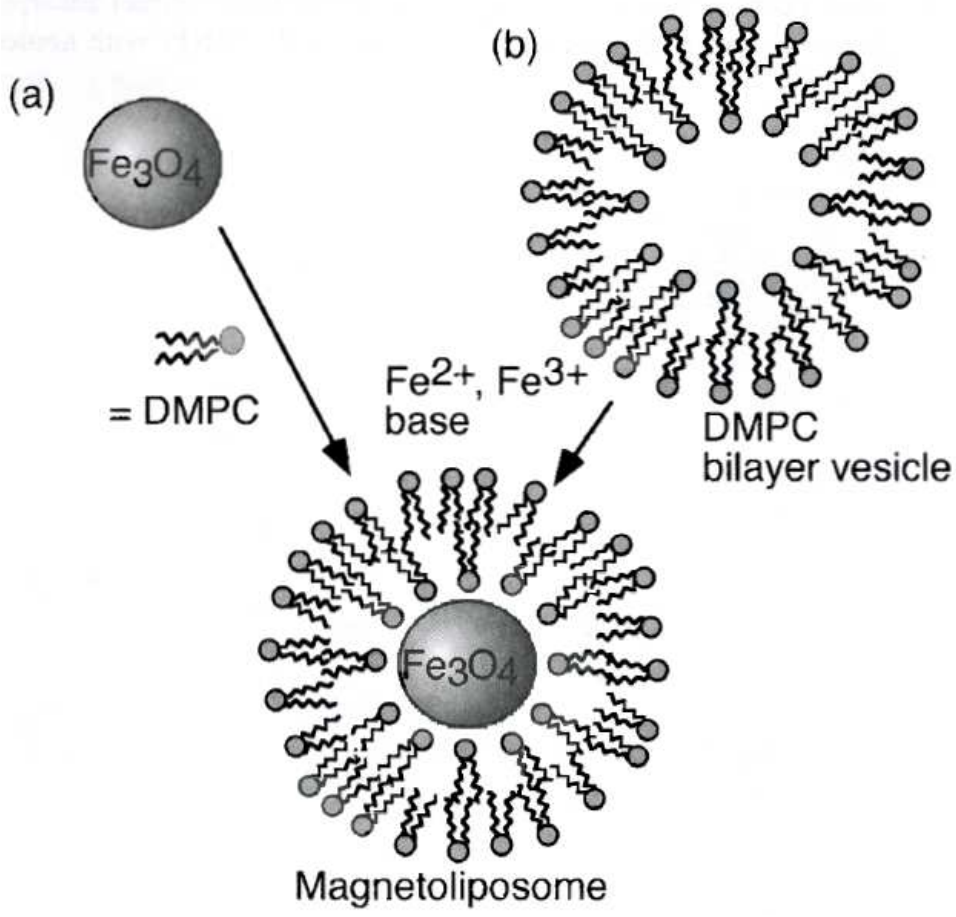

Figure 1.36. Synthesis of magnetoliposomes (a) by employing a lipid bilayer as reactor and (b) lipid coating of Fe_3O_4 MNPs [74].

1.4.2 Physical Properties of MNPs

1.4.2.1 Spinel Crystal Structure

Several of the commercially important magnetic oxides have the spinel structure (AB_2O_4) (Fig.1.37). The parent spinel is $MgAl_2O_4$. It has an essentially cubic closed packed array of oxide ions with Mg^{2+}, Al^{3+} in tetrahedral and octahedral interstices, respectively. There are well over a hundred compounds with the spinel structure such as oxides, sulphides and tellurides. The other divalent cation can be many different transition metal species including Fe^{2+}, Co^{2+}, Ni^{2+} and Zn^{2+} among others. The structure as illustrated in Fig.1.37 can be thought of as a face centered cubic lattice of oxygen anions with metal cations distributed on the tetrahedral and octahedral sites, sometimes denoted as the A and B sites respectively.

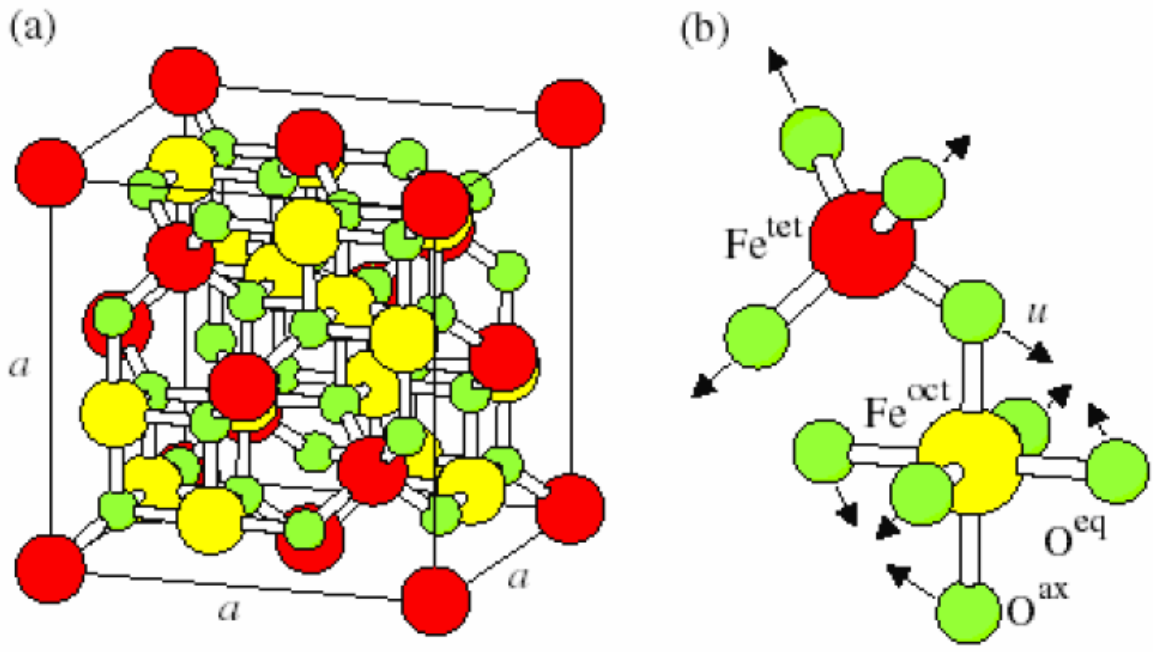

Figure 1.37. Crystal structures of magnetite (Fe_3O_4). (a) Face-centered cubic inverse spinel structure of magnetite. (b) Magnification of one tetrahedron and one adjacent octahedron sharing an oxygen atom. Fe^{2+}, Fe^{3+} occupy A site (red) which is a tetrahedral site with four nearest oxygen atoms and Fe^{3+} occupy B site yellow) which is a octahedral site with six nearest oxygen atoms (green) [84a].

Normal spinel: $(Me^{2+})[Fe^{3+}{}_2]O_4$ (Me^{2+} = Fe^{2+}, Zn^{2+}, Mn^{2+}, Ni^{2+}, Co^{2+}, etc.)

Inverse spinel: $(Fe^{3+})[Me^{2+}{}_XFe^{3+}]O_4$ (Some examples are shown in Fig.1.38)

General formula: $(Me^{2+}{}_{1-x}Fe^{3+}{}_x)[Me^{2+}{}_xFe^{3+}{}_{2-x}]O_4$

(x ⟶ degree of inversion - proportion of 3-valent cation (Fe^{3+}) at tetrahedral lattice sites)

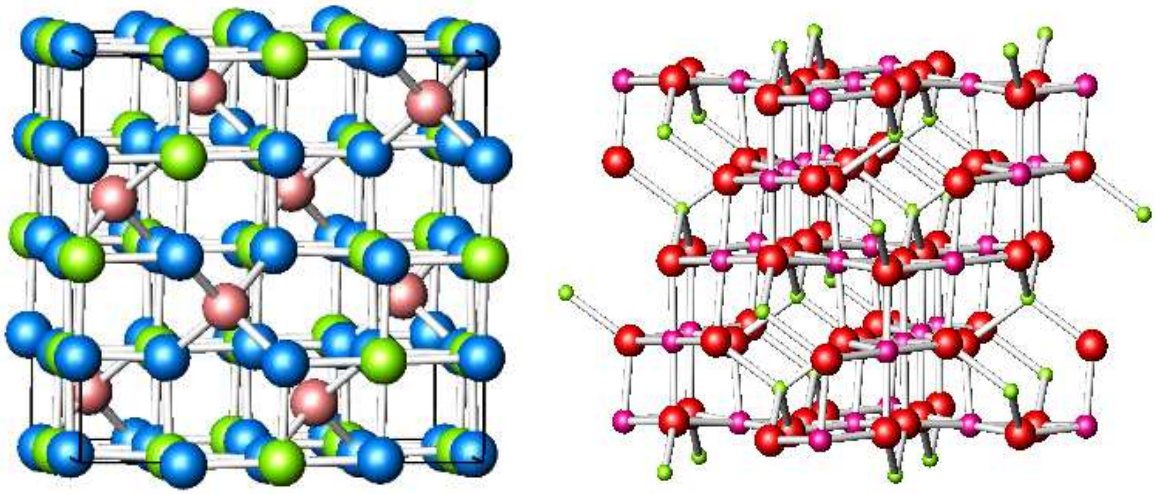

Figure 1.38 a) $CoFe_2O_4$. The green atoms are Co, pink atoms are Fe, and blue atoms are O. b) $LiMn_2O_4$. The green atoms are Lithium, the pink atoms are Manganese, and the red atoms are oxygen [84b].

1.4.3 Characterization Techniques of MNPs

Transmission electron microscopy (TEM) and high-resolution transmission electron microscopy (HRTEM) are among the most important tools used to image the particle size, distribution, and the internal structure of nanoparticles. It works by passing electrons that are accelerated to 100 KeV or higher, through the sample and using condenser lens system to focus the image of the structure.The samples used for TEM must be very thin (usually less than 100 nm), so that electrons can be transmitted across the specimen (Fig.1.39).

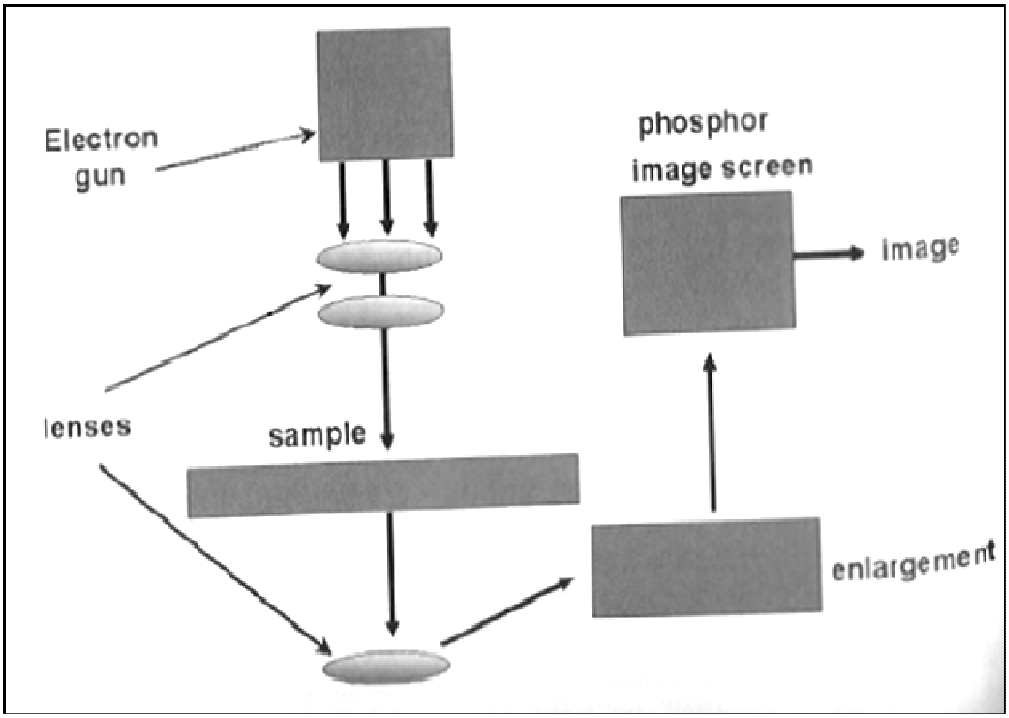

Figure 1.39. Highly simplified view of structure of TEM [85].

Scanning electron microscopy (SEM) is a useful technique to provide images of surface features of magnetic nanoparticles. A beam of electrons is concentrated on a spot of approximately 5 nm in diameter on the specimen surface and scanned back and forth across the surface. As the electrons strike and penetrate the surface, a number of interactions occur that result in the emission of electrons and photons from the specimen, and the surface topography is revealed by collecting the emitted electrons [Fig.1.40] [85].

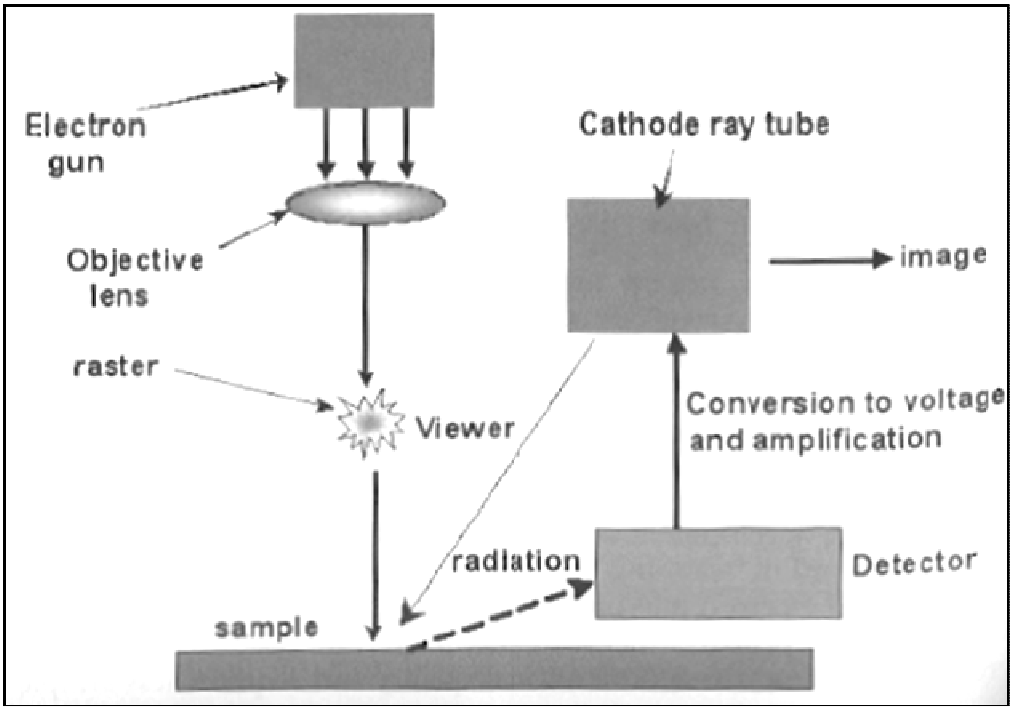

Figure 1.40. Highly simplified view of structure of SEM [85].

X-ray diffraction (XRD) has been widely employed to determine the crystal structure, crystallinity and lattice constants of nanocrystals. In XRD, a collimated beam of X-rays is incident on a specimen and is diffracted by the crystalline phases in the specimen according to Bragg's law. The crystalline phases of the specimen are identified by the diffraction pattern.

Scanning probe microscopy (SPM) is a relatively new characterization technique, which uses the interaction between a sharp tip and a surface, to produce a three-dimentional topographic image with atomic resolution. The two major members of the SPM family are scanning tunneling microscopy (STM) for electrically conductive materials and atomic force microscopy (AFM) for dielectrics. STM monitors the tunneling current between the electrically conductive surface of the sample and conductive tip, whereas AFM measures a variety of tip-sample interactions.

Magnetic measurements on magnetic nanoparticles are performed with use of a superconducting quantum interference device (SQUID). SQUID technique allows the most detailed study of the magnetization reversal of nanoparticles. The magnetic nanoparticle is placed on the SQUID loop. The SQUID detects the flux through its loop produced by the specimen magnetization.The vibrating sample magnetometer (VSM) is

another standard equipment for the magnetic characterization of thin magnetic films and structures. After a calibration it is an absolute measure of the sample magnetization as a function of applied magnetic field and temperature with a sensitivity of 10^{-8} Am^2 (corresponds to 10^{-5} emu or the magnetic moment of a iron monolayer with an area of 25 mm^2).

Fourier transform-infrared (FTIR) spectroscopy, ultraviolet-visible (UV-Vis) spectroscopy, nuclear magnetic resonance (NMR), and mass spectrometry (MS) are particularly informative about the structure and the content of magnetic nanoparticles' protective ligands.

Thermogravimetric analysis (TGA) and elemental analysis are methods that allow determination of the composition of the particles, the C/Fe ratio. TGA provides the valuable information about the binding stability of capping ligands at the surface of nanoparticles.

Sometimes thought of as a 'charge' measurement, measurement of zeta potential is used to assess the charge stability of a disperse system, and assist in the formulation of stable products. Zeta potential may be related to the surface charge in a simple system, but equally well may not. The zeta potential can even be of opposite charge sign to the surface charge. (Fig.1.41). One of the most important lessons is that it is the zeta potential that controls charge interactions, not the charge at the surface. Zeta potential is one of the main forces that mediate interparticle interactions. Particles with a high zeta potential of the same charge sign, either positive or negative, will repel each other. Zeta potential is measured by applying an electric field across the dispersion. Particles within the dispersion with a zeta potential will migrate toward the electrode of opposite charge with a velocity proportional to the magnitude of the zeta potential [86].

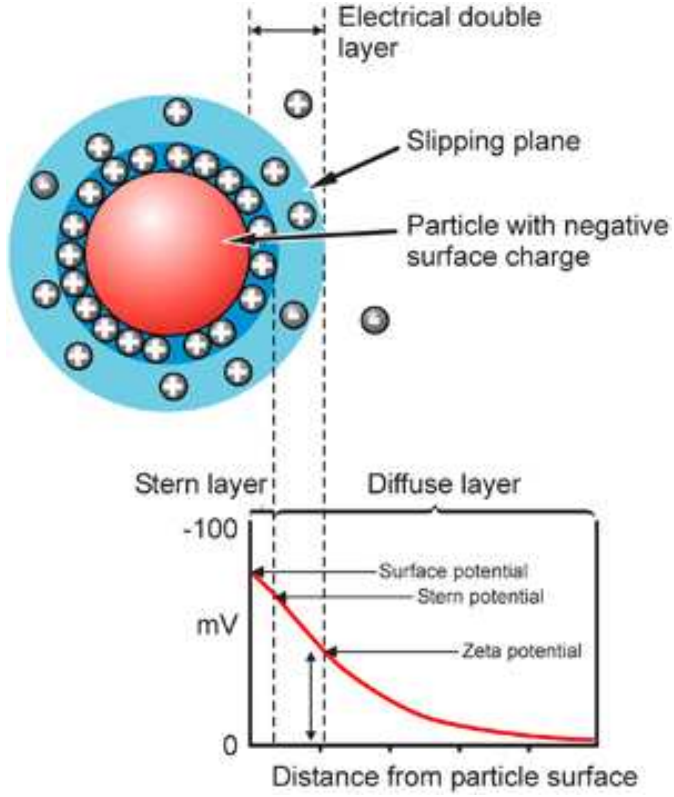

Figure 1.41. Schematic representation of zeta potential [86].

1.5 Magnetism of MNPs

Magnetism is a group of phenomena associated with magnetic fields which exist around a magnetic body or a current-carrying conductor. Whenever an electric current flows a magnetic field is produced. As the orbital motion and the spin of atomic electrons are equivalent to tiny current loops, individual atoms create magnetic fields around them. The magnetic moment of an atom is the vector sum of the magnetic moments of the orbital motions and the spins of all the electrons in the atom. This vector sum of magnetic moments can be either strong or weak depending on their alignment which is dominated by the magnetic interactions.

1.5.1 Type of Magnetism

The magnetic behavior of materials can be classified into the following five major groups which are Diamagnetism, Paramagnetism, Ferromagnetism, Ferrimagnetism, and Antiferromagnetism. Diamagnetism and paramagnetism are the two most common types of magnetism which account for the magnetic properties of most of the periodic table of elements at room temperature as shown in Figure 1.42. These elements are usually referred to as weak- or non-magnetic because they exhibit no collective magnetic interactions and they are not magnetically ordered.

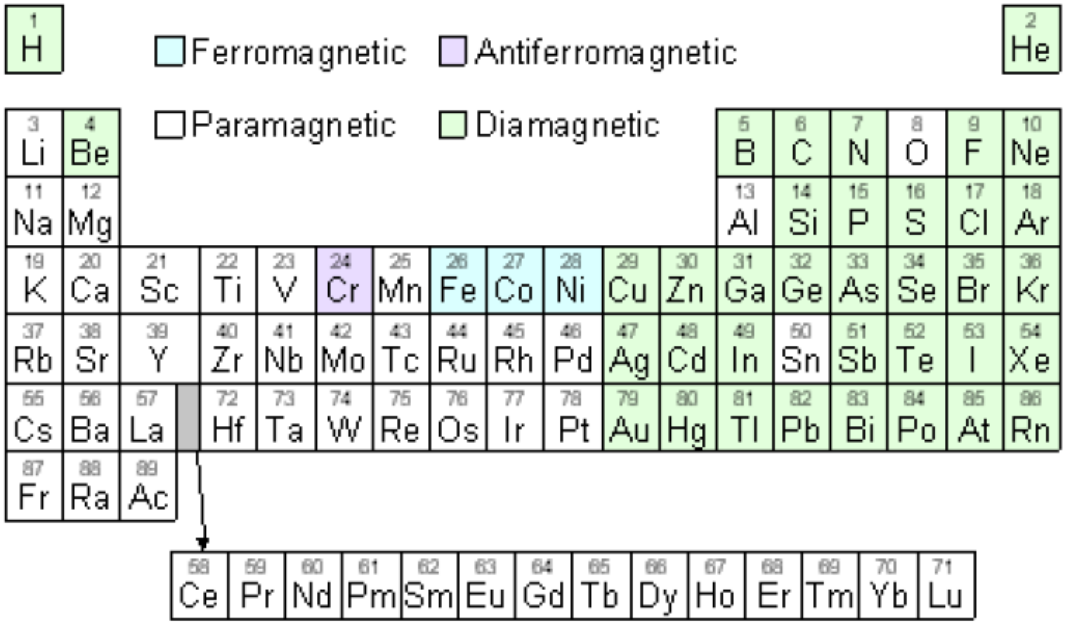

Figure 1.42. A periodic table showing the type of magnetic behavior of each element at room temperature [87].

1.5.1.1 Diamagnetism and paramagnetism

Diamagnetic materials and paramagnetic materials are weakly magnetic or non magnetic because their induced magnetization is weak and can be ignored compared to ferromagnetic and ferrimagnetic materials. Their responses to an applied field differ in the direction of the induced magnetization as shown in Fig.1.43.

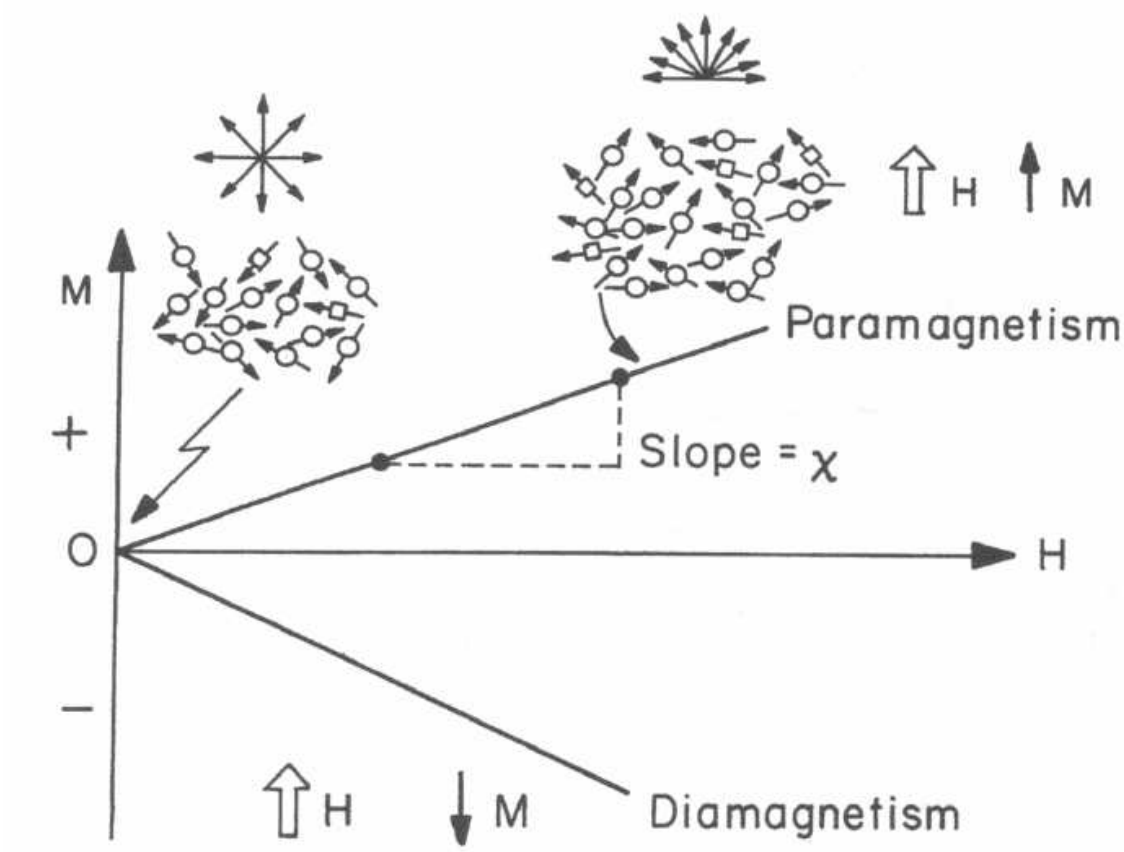

Figure 1.43. Field dependence of magnetization in paramagnetic and diamagnetic materials.Local moments in the paramagnetic materials align slightly to the direction of magnetic field [88].

A diamagnetic induction is opposed to the applied field and has a negative component in that direction. On the other hand, a paramagnetic induction is in the same direction as the applied field and has a positive component in that direction. The induced magnetizations in both diamagnetic and paramagnetic materials are normally more than six orders of magnitude less than that in ferromagnetic materials.

In a diamagnetic material, the atoms have no net magnetic moment when there is no applied field. Under the influence of an applied field (H) the spinning electrons

process and this motion, which is a type of electric current, produces a magnetization (M) in the opposite direction to that of the applied field. Diamagnetism is not a matter of aligning preexisting atomic moments due to the applied field, but rather an electronic response to the field which creates a new atomic or molecular magnetic moment.

In paramagnetism the atoms or molecules of the substance have net orbital or spin magnetic moments that are capable of being aligned in the direction of the applied field. When the magnetic field is applied, there is a tendency for each atomic moment to turn toward the direction of the applied field. But, the thermal agitation of the atoms opposes this tendency and tends to keep the atomic moments pointed at random directions. The result is only partial alignment of the moment in the field direction as shown in Fig.1.43, and therefore a small positive susceptibility. The effect of an increase in temperature is to increase the randomizing effect of thermal agitation and therefore to decrease the susceptibility.

1.5.1.2 Ferromagnetism

There are three types of magnetic ordering including ferromagnetic, antiferromagnetic, and ferrimagnetic orderings which are illustrated schematically in Fig.1.44 and many magnetic structures are so complex that it is better to describe them explicitly rather than using one of the above three categories [89].

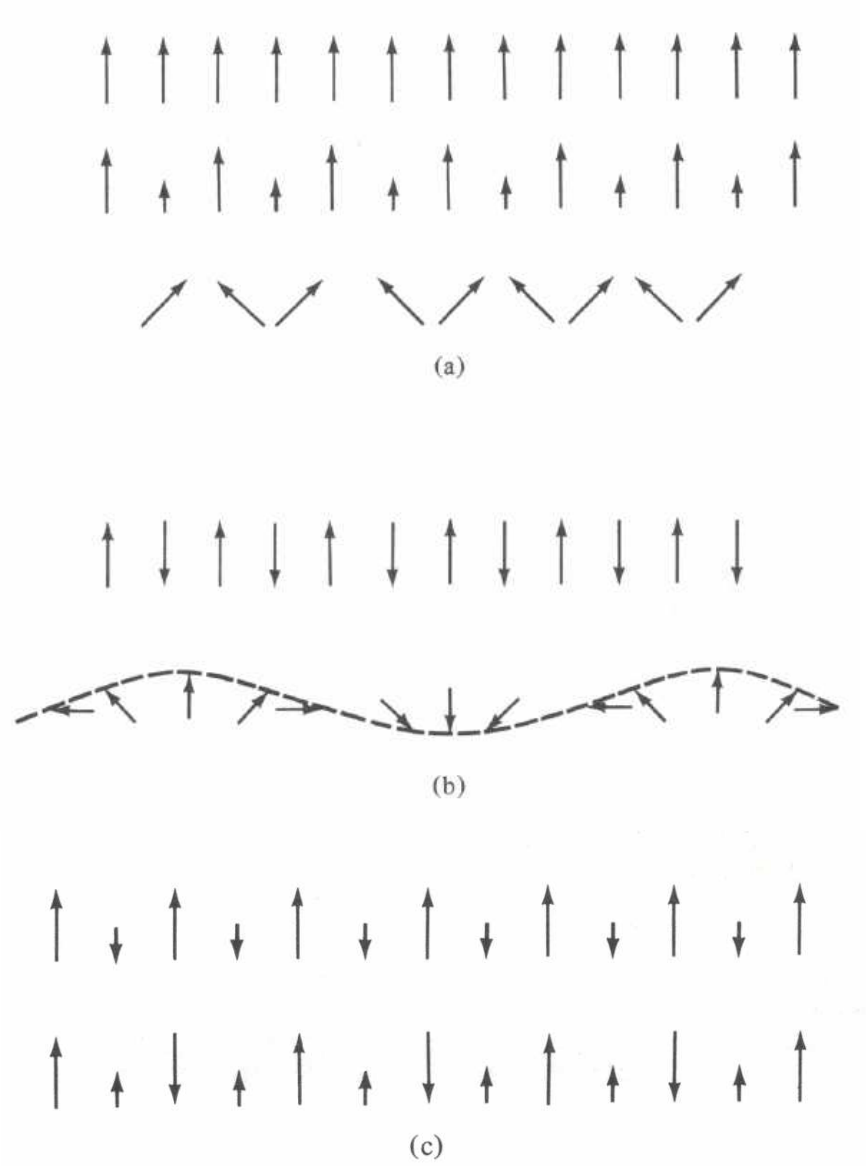

Figure 1.44. Linear arrays of spins illustrating possible (a) ferromagnetic, (b)antiferromagnetic, and (c) ferrimagnetic orderings [89].

In ferromagnetic substances, within a certain temperature range, there are net atomic magnetic moments, which line up in such a way that magnetization persists after the removal of the applied field. Below a certain temperature called the “Curie point” (or “Curie temperature”, Tc), an increasing magnetic field applied to a ferromagnetic substance will cause increasing magnetization to a higher value, called saturation magnetization. Magnetization curves of iron, cobalt, and nickel are shown in Fig.1.45 and the experimental values of the saturation magnetization (Ms) are given for each metal without a field value on the x-axis [90].

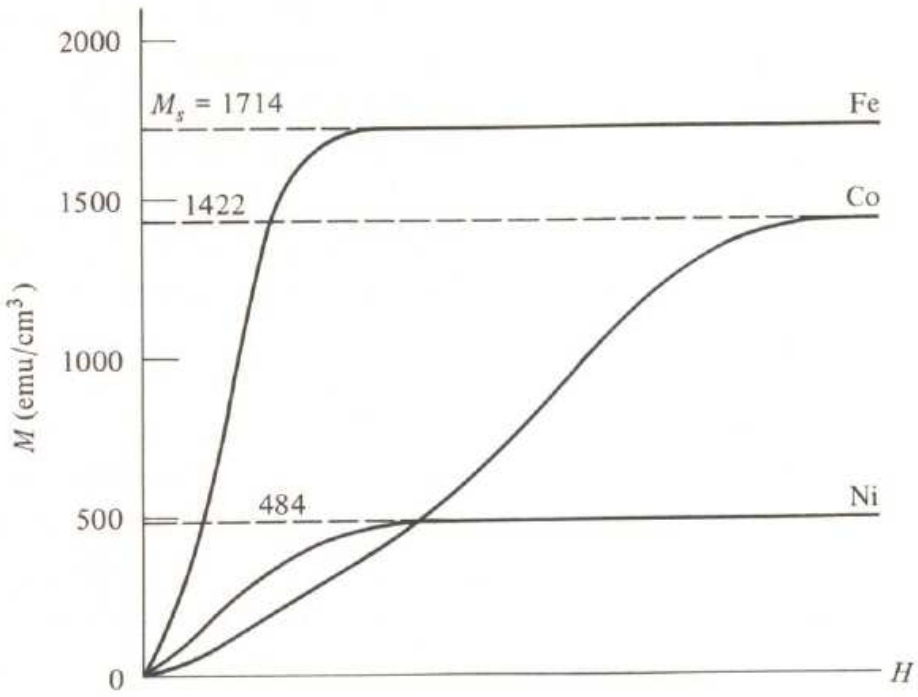

Figure 1.45. Magnetization curve of iron, cobalt, and nickel at room temperature [90].

Three distinct characteristics of ferromagnetic materials are their ; 1) Spontaneous Magnetization, 2) Curie Temperature, 3) Hysteresis.

Spontaneous Magnetization

The spontaneous magnetization is the net magnetization that exists inside a uniformly magnetized microscopic volume in the absence of a field. The magnitude of this magnetization, at 0 K, is dependent on the spin magnetic moments of electrons. A related term is the saturation magnetization which can be measured in the laboratory. The saturation magnetization is the maximum induced magnetic moment that can be obtained in a magnetic field (H_{sat}); beyond this field no further increase in magnetization occurs.The difference between spontaneous magnetization and the saturation magnetization has to do with magnetic domains. Saturation magnetization is an intrinsic property, independent of particle size but dependent on temperature.

Curie Temperature

Even though electronic exchange forces in ferromagnets are very large, thermal energy eventually overcomes the exchange and produces a randomizing effect. This occurs at a particular temperature called the Curie temperature (T_C). Below the Curie temperature, the ferromagnet is ordered and above it, disordered. The saturation magnetization goes to zero at the Curie temperature. A typical plot of magnetization vs temperature for magnetite is shown below (Fig.1.46):

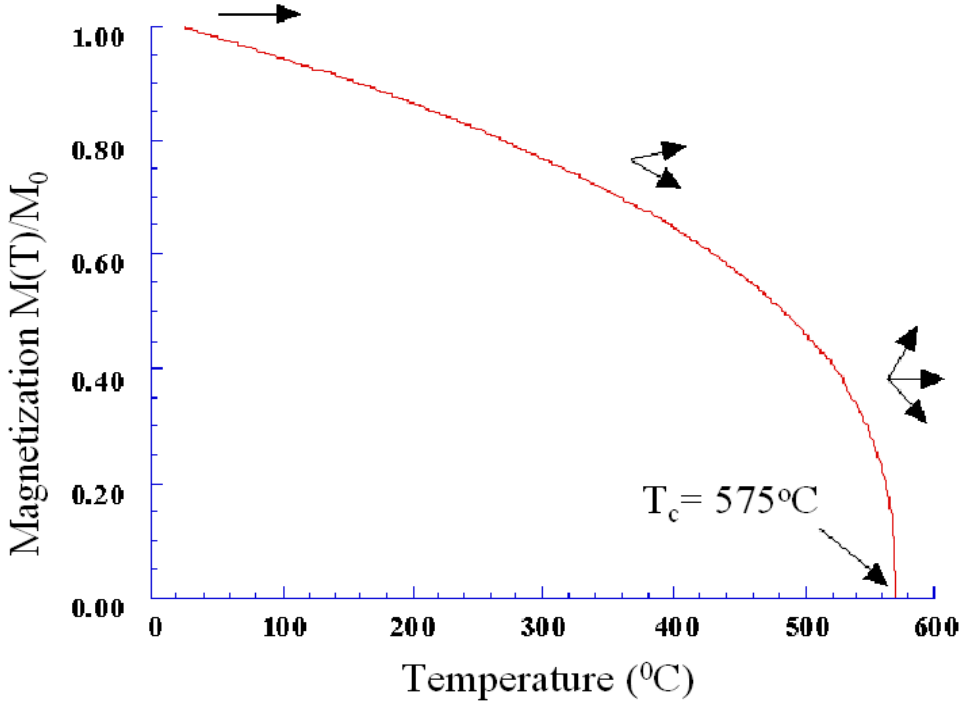

Figure 1.46. Magnetization vs Temperature plot [91].

The Curie temperature is also an intrinsic property and is a diagnostic parameter that can be used for mineral identification. However, it is not foolproof because different magnetic minerals, in principle, can have the same Curie temperature.

Hysteresis

In addition to the Curie temperature and saturation magnetization, ferromagnets can retain a memory of an applied field once it is removed. This behavior is called

hysteresis and a plot of the variation of magnetization with magnetic field is called a hysteresis loop.

A hysteresis loop shows the relationship between the induced magnetic flux density **B** and the magnetizing force **H.** It is often referred to as the B-H loop. An example hysteresis loop is given (Fig.1.47).

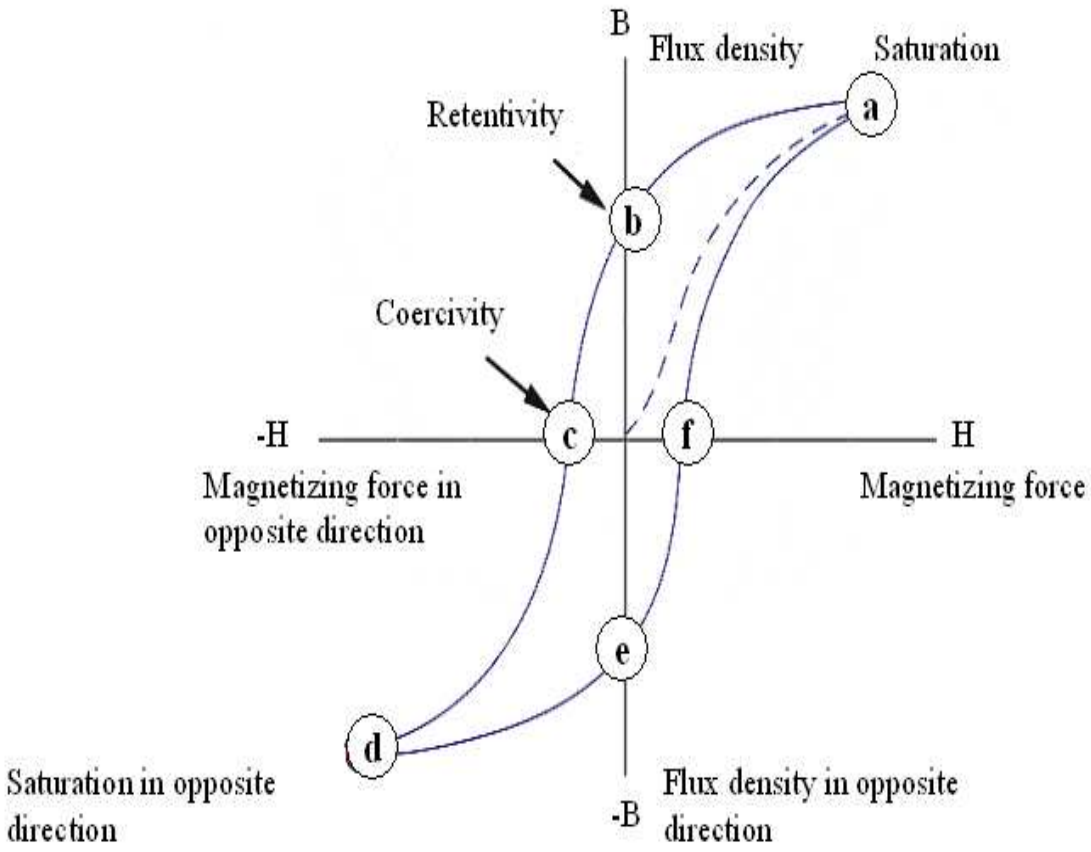

Figure 1.47. Hysteresis loop [92].

The loop is generated by measuring the magnetic flux **B** of a ferromagnetic material while the magnetizing force **H** is changed. A ferromagnetic material that has never been previously magnetized or has been thoroughly demagnetized will follow the dashed line as **H** is increased. As the line demonstrates, the greater the amount of current applied **(H+)**, the stronger the magnetic field in the component **(B+)**. At point "a" almost all of the magnetic domains are aligned and an additional increase in the magnetizing force will produce very little increase in magnetic flux. The material has

reached the point of magnetic saturation. When **H** is reduced back down to zero, the curve will move from point "a" to point "b." At this point, it can be seen that some magnetic flux remains in the material even though the magnetizing force is zero. This is referred to as the point of retentivity on the graph and indicates the remanence or level of residual magnetism in the material (Some of the magnetic domains remain aligned but some have lost there alignment). As the magnetizing force is reversed, the curve moves to point "c", where the flux has been reduced to zero. This is called the point of coercivity on the curve (The reversed magnetizing force has flipped enough of the domains so that the net flux within the material is zero). The force required to remove the residual magnetism from the material, is called the coercive force or coercivity of the material.

As the magnetizing force is increased in the negative direction, the material will again become magnetically saturated but in the opposite direction (point "d"). Reducing **H** to zero brings the curve to point "e." It will have a level of residual magnetism equal to that achieved in the other direction. Increasing **H** back in the positive direction will return **B** to zero. The curve do not return to the origin of the graph because some force is required to remove the residual magnetism. The curve will take a different path from point "f" back the saturation point where it with complete the loop [92].

Hysteresis parameters are not solely intrinsic properties but are dependent on grain size, domain state, stresses, and temperature. Because hysteresis parameters are dependent on grain size, they are useful for magnetic grain sizing of natural samples [91].

1.5.1.3 Antiferromagnetism

In an antiferromagnet, the spins are ordered in an antiparallel arrangement with zero net moment at temperatures below the ordering or Néel temperature. Temperature dependence of the magnetic susceptibility in antiferromagnets is shown in Fig.1.48 in comparison with those in paramagnets and ferromagnets. Below the Néel temperature of an antiferromagnet, the spins have antiparallel orientations and the susceptibility attains its maximum value at TN where there is a well-defined kink in the curve of χ versus T. The transition is also marked by peaks in the heat capacity and the thermal expansion coefficient.

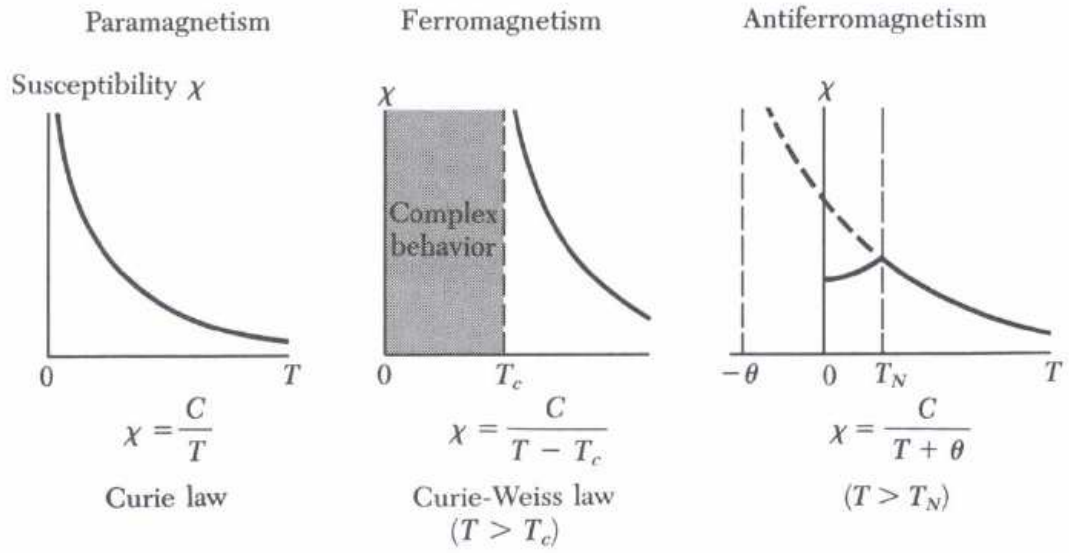

Figure 1.48. Temperature dependence of the magnetic susceptibility in paramagnets, ferromagnets, and antiferromagnets [93].

1.5.1.4 Ferrimagnetism

In ferrimagnets, the spins are ordered in an antiparallel arrangement like antiferromagnets, but their net moments are not zero. So, ferrimagnetism is the special form of antiferromagnetism and is exhibited by the ferrites which have a spinel structure. In these materials the magnetic moments of adjacent ions are antiparallel and of unequal strength, or the number of magnetic moments in one direction is greater than those in the opposite direction.

1.6 Applications of MNPs

High-density magnetic data storage arrays provide a major technological driving force for the exploration of MNPs. MNPs have also been demonstrated to be functional elements in magneto- optical switches, sensors based on Giant Magnetoresistance, and magnetically controllable Single Electron Transistor devices or photonic crystals. Three dimensional nanoparticle assemblies with complex structures can also be fabricated by

the slow evaporation technique in the presence of applied magnetic field. These technological applications are all in addition to the numerous known and developed applications of aqueous suspensions of MNPs (ferrofluids).

Doping magnetic ions into semiconductors to produce Dilute Magnetic Semiconductors (DMS) has long been used to alter the electronic and optical properties of the parent materials. DMS nanoparticles have applications in the fabrication of novel optical materials. For example both Ni: ZnS and Co: ZnS DMS nanoparticles display strong photoluminescent emission of green light.

MNPs are also finding a multitude of biomedical applications, the most prevalent of which is Magnetic Resonance Imaging (MRI) contrast agents. Recent work has involved the development of bioconjugated MNPs, which facilitate specific targeting of these MRI probes to brain tumors, and enabled real-time monitoring of both gene expression and T-cell or progenitor cell migration. Bioconjugate MNPs are also useful as probes for *in vitro* detection of biomolecular interactions using a variety of techniques, including the detection of DNA hybridization by NMR [74].

MNPs are also used as highly active catalysts which have long been demonstrated bye the use of finely divided metals in several reactions. Recent synthetic advances have resulted in the preparation of catalysts based on smaller particles or matrix supported nanoparticle catalysts. Applications of MNPs are summarized in Fig.1.49.

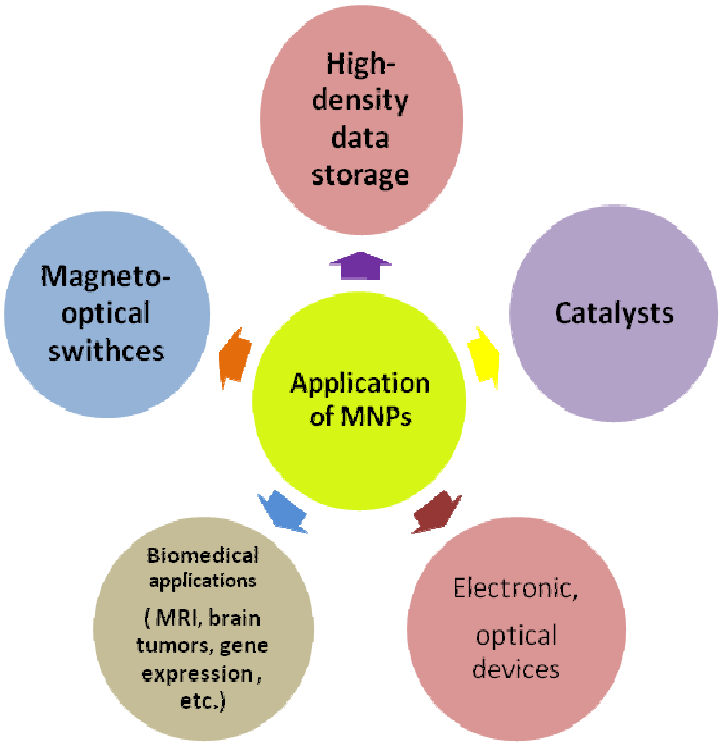

Figure 1.49. Schematic illustration of some applications of MNPs.

1.7 Purpose of the Thesis

The purpose of this study is to synthesize and characterize M_3O_4 (M= Fe, Co, and Mn) type of magnetic spinel nanoparticles by various methods using surfactant and without surfactant. By using these methods, these materials will be synthesized for the first time in this study.

CHAPTER 2

EXPERIMENTAL

2.1 Instrumentation

2.1.1 X-ray Powder Diffraction (XRD)

X-ray powder diffraction analysis (XRD), was used for the characterization of the crystalline product. Philips diffractometer with PW 3020 goniometer (Cu K_{α}).

2.1.2 Electron Microscopy

2.1.2.1 Scanning Electron Microscopy (SEM)

Scanning Electron Microscopy (SEM) analysis was performed, in order to investigate the microstructure of the sample, using FEI XL40 Sirion FEG Digital Scanning Microscope. Samples were coated with gold at 10 mA for 2 min prior to SEM analysis.

2.1.2.2 Transmission Electron Microscopy (TEM)

Transmission Electron Microscopy (TEM), analysis was performed using a FEI Tecnai G2 Sphera Microscope. A drop of diluted sample in ethanol was deposited on a TEM grid and alcohol was evaporated. Particle size distribution was obtained from several micrographs, counting a minimum of 150 particles.

2.1.3 Fourier Transform Infrared Spectroscopy (FTIR)

For FTIR measurements, Mattson Satellite Infrared Spectrometer FTIR was used in the region 400-4000 cm-1. Spectra of solid samples were obtained from KBr pellets using KBr / sample weight ratio of 100/3 mg.

2.1.4 Vibrating Sample Magnetometer (VSM)

Magnetic measurements were carried out with the Quantum Design Model 6000 Vibrating Sample Magnetometer (VSM) option for the Physical Property Measurement System (PPMS) and parameters like specific saturation magnetization (Ms), coercive force (Hc) and remanence Mr) were deduced. In order to eliminate the interaction of the particles in the samples, the powder was dispersed in paraffin for measurement.

2.1.5 Zeta Potential

Zeta potential measurements were performed using a Zetasizer Nano (Malvern Instruments) in folded capillary zeta potential cells, and pH titrations were performed using 0.25 M NaOH and 0.25 M HCl solutions in the auto-titrator unit.

2.2 Procedure

2.2.1 Fe_3O_4 Nanoparticles

All chemicals were obtained from Sigma-Aldrich, as analytical grade and used without any further purification.

2.2.1.1 Cost- effective gel-to-crystalline Method *(Tev13)*

A 0.2 M aqueous solution of ferrous chloride ($FeCl_2.4H_2O$) was prepared in deionized water. A 2M aqueous solution of NH_4OH is added dropwise to precipitate metals as hydroxide gel. The hydrated iron gel is thoroughly washed and transferred to a flask fitted with a water condenser. It is to be noted that the presence of anion contaminants, such as Cl^-, NO_3^-, might impede the reaction by forming soluble salts with Fe^{2+}. The gel was stirred under reflux for 4h at 100 °C under N_2 flow to ensure

inert atmosphere (Fig.2.1). The continuous influx of the solvent during the reflux process breaks the gel network into more energetically favorable small crystalline iron-oxide regions [94]. The solid product after refluxing was filtered and oven-dried.

Figure 2.1. Scheme of synthesizing Fe_3O_4 nanoparticles by reflux method.

2.2.1.2 Co-precipitation *(Tev 9)* and Hydrothermal Synthesis *(Tev19)*

In a typical procedure for preparation of Fe_3O_4 nanoparticles, ferric chloride hexahydrate ($FeCl_3.6H_2O$) and $FeCl_2.4H_2O$ are used as iron sources, and NH_4OH (5 mL) is used as the precipitator. Distilled water is used as the solvent. The solution of $FeCl_3$ and $FeCl_2$ was mixed with certain molar ratio. The corresponding phase NH_4OH was slowly injected into the mixture of $FeCl_3$ and $FeCl_2$ under vigorous stirring under N_2 gas. The mixture was heated to 90 ^oC for 1/2 hour. After black precipitation, the supernatant was removed by applying a permanent magnet. Then Fe_3O_4 particles were repeatedly washed with ethanol and dried under N_2 gas (Tev9).

For experiment Tev19, 1 g of cationic surfactant cetyltrimethylammonium bromide (CTAB) was dissolved in 35 mL deionized water. The 1 g of ferric chloride hexahydrate ($FeCl_3.6H_2O$) was added to solution. After 15 min stirring, stoichiometric amount of ferrous chloride tetrahydrate ($FeCl_2.4H_2O$) was introduced into the mix solution while vigorous stirring. Deionized water was added to make the solution for a

total volume of 40 mL , and the pH of the solution was adjusted to 11.0. Before being transferred to a Teflon-lined autoclave of 50 mL capacity, the solution mixture was pretreated under an ultrasonic water bath for 45 min. Hydrothermal synthesis was carried out at 130 ^{o}C for 12h in an electric oven. Afterwards, the autoclave was allowed to cool to room temperature gradually. The black precipitate was collected and washed with water several times. Then product was dried.

2.2.1.3. Oxidation-Reduction Method *(Tev14a & Tev25)*

Iron sulfate heptahydrate, sodium nitrate and NaOH were dissolved in de-ionized H_2O to prepare Fe^{+2}, $NaNO_3$ and NaOH solutions that were 0.8 (2.224 g/10mL), 0.8 (0.68 g/ 10mL) and 3.2 mol/L respectively. Then a predetermined volume of NaOH that was pre-treated with N_2 to remove oxygen under 10 min heating. When the temperature of the sodium hydroxide went up 90 ^{o}C, a stoichiometric volume of iron sulphate solution was added dropwise at 10 mL/min rate into the three-neck flask while stirring. After exhausting the volume of sodium sulfate solution in 5 min, a pre determined sodium nitrate solution was dropped into the flask and the reaction was kept over night and then it was decant and dried (Tev14a). For experiment Tev25, the same procedure was used except that hydrolyzing agent was changed from NaOH to NH_3 (saturated aqueous ammonia solution).

2.2.1.4 PEG-asisted Route *(Te2 & Te3)*

In a typical experiment, 2.79 g of $FeCl_3.6H_2O$ and 1 g of $FeCl_2.4H_2O$ were added dropwise into a 50 mL Teflon-lined stainless autoclave, then 30 mL PEG-400, heated and melted, was injected to the autoclave, followed by a certain amount of NaOH. After continuous stirring, a homogeneous solution could be obtained. The autoclave was kept at certain temperatures for 12 h, then cooled to room temperature naturally. The products were filtered and washed several times with distilled water and absolute ethanol, and finally dried in a vacuum oven at 25 ^{o}C for 12 h. For Te2, pH is 11.4. On the other hand, for Te3, The conditions are approximately same, except NH_3 gas was used instead of NaOH (pH = 10.4).

2.2.2 Co_3O_4 Nanoparticles

2.2.2.1. Reflux method *(Tev37)*

A 4.74 g of $CoCl_2.4H_2O$ is dissolved in deinozed H_2O to form 0.2M solution. A 2M NaOH is added to that dropwise to precipitate metals as a blue hydroxide gel. The hydrated cobalt gel is throughly washed free of anions and transferred to a flask fitted with a water condenser. The gel was continuosly stirred for 2h maintaining the temperature at 100 ^oC. The color changed from blue to pink. Then pink gel was continuosly stirred for 1h. Experiments were performed under N_2 gas until the formation of a crystalline solid product. Then black crystalline powder formed was filtered and oven-dried.

2.2.2.2. Oxidation-Reduction Method *(Tev11b)*

Cobalt sulfate heptahydrate, sodium nitrate and NaOH were dissolved in de-ionized H_2O to prepare Co^{2+}, $NaNO_3$ and NaOH solutions that were 0.8, 0.8 and 3.2 mol/L respectively. Then a predetermined volume of NaOH that was pre-treated with N_2 to remove oxygen under 10 min heating. When the temperature of the sodium hydroxide went up to approximately 90 ^oC, a stoichiometric volume of cobalt sulphate solution was added dropwise at 10 mL/min rate into the three-neck flask while stirring. After exhausting the volume of sodium sulfate solution in 5 min, a pre determined sodium nitrate solution was dropped into the flask and the reaction was kept overnight.

2.2.2.3 Simple Route Using Egg White (*Te19*)

$Co(ac)_2.4H_2O$ and $Co(acac)_3.4H_2O$ and freshly extracted egg white (ovalbumin) were used as the starting materials. 40 mL of egg white was first mixed with 40 mL deionized water with vigorous stirring at 300 K until a homogeneous solution was obtained. Subsequently, 0.5 g of $Co(ac)_2.4H_2O$ and 0.72 g of $Co(acac)_3.4H_2O$ (a mole ratio corresponding to the nominal composition of Co^{2+} : Co^{3+} ratio of 1:2) were added slowly to the egg white solution with vigorous stirring at 300 K for 2 h to obtain a well-dissolved solution. Throughout the whole process described above, no pH adjustment

was made. Then, the mixed solution was evaporated by heating in a high temperature oven at 353 K for 3h until a dried precursor was obtained. The dried precursor was crushed into powder using a mortar and pestle.

2.2.3 Mn_3O_4 Nanoparticles

2.2.3.1 Thermal Decomposition Method *(Tev 29)*

In a typical procedure for the preparation of Mn_3O_4 nanoparticles, in a 20 mL portion of 2-pyrrolidone containing 2 mmol (0.50632 g) $Mn(acac)_2$ was heated with vigorous stirring at 250 ^oC. After being refluxed for 12 h, the reaction system was cooled to room temperature. Addition of methanol into 2-pyrrolidone solution resulted in a dark-brown precipitate which was washed with acetone for several times and then dried. The final brown powder was proven to be soluble in water and 2-pyrrolidone.

2.2.3.2 Oxidation-Reduction Method *(Tev12a & Tev21)*

The concentration of $MnSO_4.5H_2O$, $NaNO_3$ and NaOH solutions were 0.8, 0.8 and 3.2 mol/L. A predetermined volume of NaOH was placed into three-neck flask and was heated for 10 min. When the temperature of NaOH reached to 100 ^oC, a stoichiometric volume of $MnSO_4.5H_2O$ solution was added dropwise at 10mL/min into the three-neck flask under continuous stirring (Fig.2.2). After exhausting the sodium sulfate solution in 6 min, a predetermined sodium nitrate solution (as an oxidant) was added at a rate of 10 ml/min into the flask and the reaction was kept overnight under stirring (Tev12a). For experiment Tev21, the same procedure was used except that hydrolyzing agent was changed from NaOH to NH_3 (saturated aqueous ammonia solution). Thus formed two dark brown crystalline products were washed with distilled water and acetone respectively, filtered and then oven dried overnight at 110 ^oC.

Figure 2.2. Scheme of synthesizing Mn_3O_4 nanoparticles by oxidation-reduction method.

2.2.3.3 PEG- assisted Route *(Te5)*

In a typical experiment, 1 g of $Mn(acac)_2$ was added dropwise into three neckled bottom flask , then 16.7 mL PEG-400, heated and melted, was injected to the flask under NH_3 gas (pH=11). After continuous stirring , a homogeneous solution could be obtained. Then it was put in the autoclave and was kept at certain temperatures for 12 h, then cooled to room temperature naturally. The products were filtered and washed several times with distilled water and absolute ethanol, and finally dried in a vacuum oven at 25 ^oC for 12 h.

CHAPTER 3

RESULTS AND DISCUSSIONS

3.1 Fe_3O_4 analysis

3.1.1 Fe_3O_4 nanoparticles by cost-effective gel-to-crystalline method *(Tev13)*[1]

Alkalization reaction of ferrous ions has been extensively studied by Refait and Olowe [95, 96] and they proposed the following reactions for the mechanism of formation of Fe_3O_4.

$$Fe^{2+} + 2OH^- \rightarrow Fe(OH)_2 \quad [1]$$

$$3Fe(OH)_2 + 1/2O_2 \rightarrow Fe(OH)_2 + 2FeOOH + H_2O \quad [2]$$

$$Fe(OH)_2 + 2FeOOH \rightarrow Fe_3O_4 + 2H_2O \quad [3]$$

Thus, in the synthesis with ferrous ions alone, as in our case, Fe_3O_4 is formed as a result of the dehydration reaction of ferrous hydroxide and ferric oxyhydroxide (reaction 3) in which the latter compound is produced by the partial oxidation of ferrous hydroxide by O_2 dissolved in air (reaction 2). This is the mechanism controlling the transformation of iron hydroxide phases to the final phase of magnetite.

[1] T. Ozkaya, M.S. Toprak, A. Baykal, H. Kavas, Y. Köseoğlu, B. Aktaş, **"Synthesis of Fe_3O_4 nanoparticles at 100^{o}C and Its Magnetic Characterization"**, doi:10.1016/j.jallcom.2008.04.101.

3.1.1.1. XRD Analysis

Phase investigation of the crystallized product was performed by XRD and the pattern is shown in Figure 3.1. The XRD pattern indicates that the product is iron oxide, Fe_3O_4, and the diffraction peaks are broadened owing to small crystallite size. All the observed diffraction peaks could be indexed by the cubic structure of Fe_3O_4 (JCPDS no 19-629) indicating a high phase purity of iron oxide. The lattice parameter "a" for the synthesized iron oxide nanoparticles was refined using TREOR 90 program [100] and "a" was obtained as 8.388±0.002 Å. This value is between the lattice parameters of magnetite, Fe_3O_4 (8.393 Å, JCPDS file no: 19-629), and maghemite, γ-Fe_2O_3 (8.3515 Å, JCPDS file no: 39-1346), both of which have spinel structure. Maghemite has basically the same crystal as magnetite, however it can also be considered as an Fe^{2+}-deficient magnetite with formula $(Fe_8^{3+})_A[Fe_{\frac{40}{3}}^{3+}\square_{\frac{8}{3}}]_BO_{32}$, where $\square$ represents a vacancy, A indicates tetrahedral positioning and B octahedral. The obtained phase has an intermediate lattice parameter which could be defined as non-stoichiometric magnetite, showing that a partial oxidation probably occurs in air. Indeed, Fe^{2+} cations in nanoparticles are not thermodynamically stable in air. Because of the high reactivity of nanoparticles, they are easily oxidized into Fe^{3+} in air. The cell parameter decreases linearly as the deviation, δ, from stoichiometry (in $Fe_{3-\delta}O_4$) increases [97-100]. Calculations of δ purely based on the lattice parameter for our case yielded δ as 0.15 ($Fe_{2.85}O_4$). Although the crystalline phase has lattice parameter very close to magnetite, this deviation in stoichiometry may be attributed to a surface oxidation of approximately 30% of Fe^{2+} ions. On the basis of the Scherrer equation [101], using the width of most intense diffraction line, the average crystallite size for Fe_3O_4 was found as ~11 nm, however it is found as unreliable at estimating particle size, because the assumption of an underlying crystal structure (translational symmetry) is often invalid. [102]. Therefore, in order to test the reliability of estimated crystallite size from Scherrer equation, we use the difraction profile fitting to estimate the size using Equation 1 in Wejrzanowski et.al. [103,104]. The line profile, shown in Figure 3.1, is fitted for 5 peaks (220, 311, 400, 511 and 440) and the average crystallite size, $D \pm \sigma$, is obtained as 11 ± 6 nm.

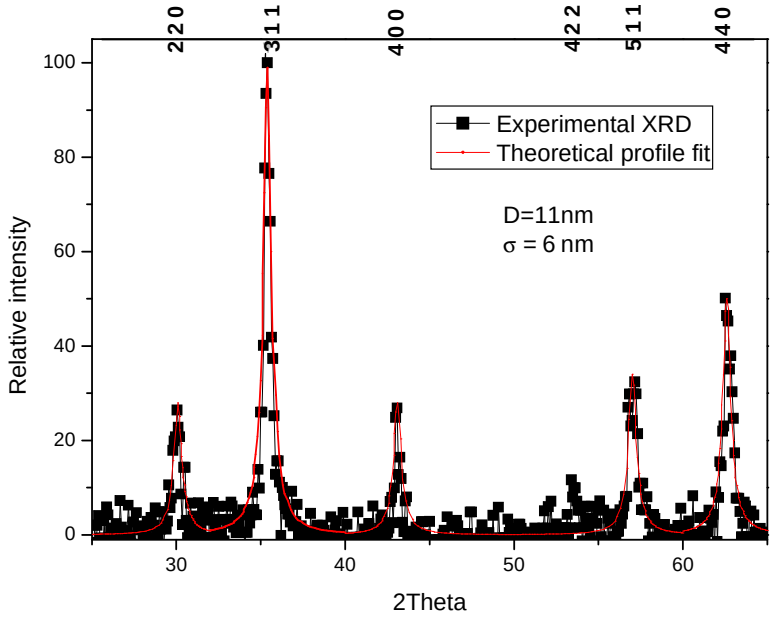

Figure 3.1 X-ray powder diffraction pattern and theoretical profile fit of as-synthesized Fe_3O_4 nanoparticles.

3.1.1.2. FTIR Analysis

FTIR spectra of commercial Fe_3O_4 powder and as synthesized Fe_3O_4 nanoparticles are shown in Fig.3.2. As prepared powder presents characteristic peaks that are exhibited by the commercial magnetite powder: metal-oxygen band, observed at v_1 (590 cm^{-1}) corresponds to intrinsic stretching vibrations of the metal at tetrahedral site (Fe_{tetra}↔O), whereas metal-oxygen band observed at v_2 (445 $cm^{-1)}$, is assigned to octahedral-metal stretching (Fe_{octa}↔O) [105-107]. Characteristic peaks for maghemite are not observed probably due to the overlap with wide absorption peaks of dominant magnetite phase.

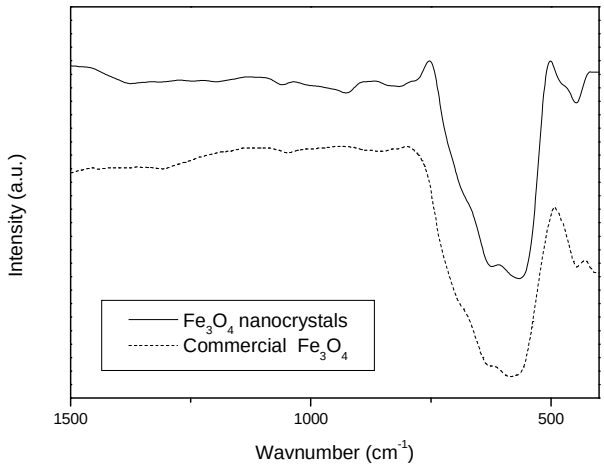

Figure 3.2. FTIR spectrum of iron oxide nanoparticles and commerical magnetite powder.

3.1.1.3. TEM Analysis

(a)

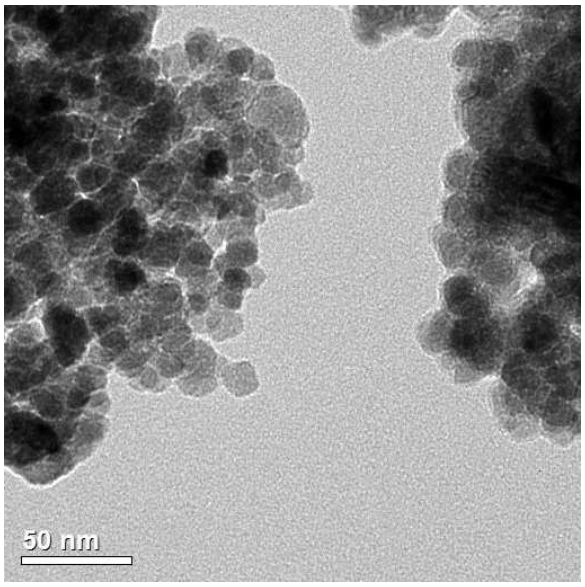

(b)

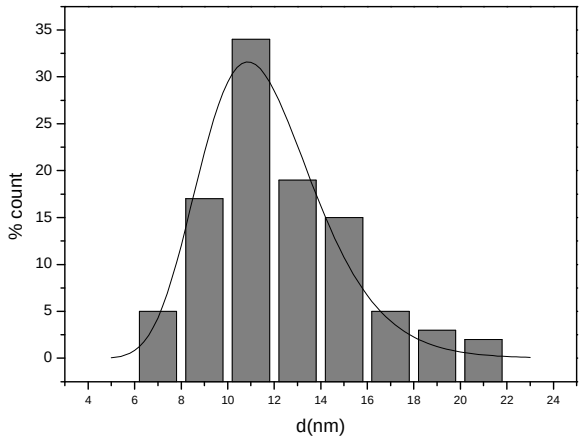

(c)

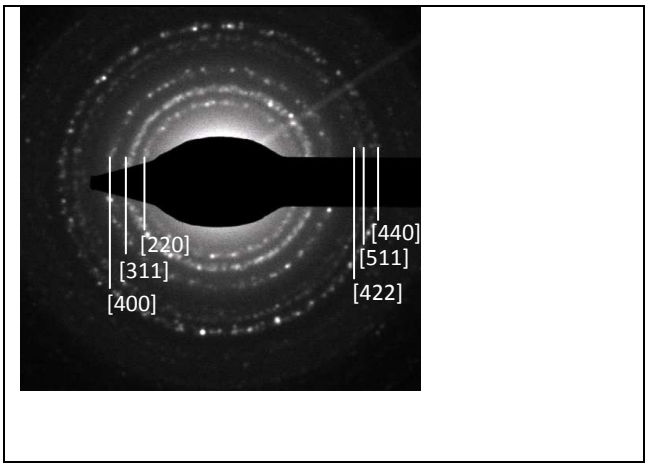

Figure 3.3. TEM micrograph **(a),** calculated histogram **(b),** and Electron diffraction pattern, **(c)** for as-synthesized iron oxide nanoparticles.

TEM micrograph of as-synthesized iron oxide nanoparticles is shown in Fig.3.3(a) and their particle size distribution is shown in Fig.3.3(b). Particles have approximately spherical shapes and their size (diameters) changes in the range of 7-21 nm. In order to analyze the size distribution quantitatively, the particle size distribution was fitted using a log-normal function [108].

$$P(D) = \frac{A}{D\sigma_D\sqrt{2\pi}} \exp\left(-\frac{1}{2\sigma_D^2} \ln^2(\frac{D}{D_O}) \right) \quad (1)$$

where σ_D is the standard deviation of the diameter and D_0 is the mean diameter. A mean diameter D_o , of 11.4±0.22 nm was obtained using Eq. (1), showing a good agreement with the crystallite size obtained from XRD peak broadening. Selected area electron diffraction (SAED) pattern of nanoparticles exhibits spots and rings indicating that nanoparticles are well crystallized (Fig. 3.3(c)). Observed diffraction rings are indexed for the magnetite system using the calculated lattice parameter, “a”.

3.1.1.4. Magnetization

Magnetization measurements of iron oxide nanoparticles were performed using VSM technique and results at 10K and 300 K are shown in Fig.3.4. The saturation magnetization (M_s calculated from a plot of M vs 1/H (M at 1/H≥ 0)) value of the sample is measured as 390 emu/cm^3 at room temperature and 440 emu/ cm^3 at 10 K, respectively. These values are comparatively lower than that of bulk magnetite with an M_s of 480-500 emu/cm^3 [109, 110-112]. The magnetization of Fe_3O_4 nanoparticles increases with external magnetic field strength, however, it did not reach the saturation state yet under a high magnetic field of 5 kOe, as observed in earlier works [113-116]. The reduction of the M_s in Fe_3O_4 with a particle size of 11 nm can be attributed partly to the presence of non-magnetic (dead) surface layer, perhaps due to compositional variations, super-paramagnetic relaxation and spin canting because of antiferromagnetic interactions among the Fe spins in the nanostructured material [116,117]. As the temperature is decreased down to 10 K, the magnetization of the sample increases, exhibiting a symmetric hysteresis loop, and the sample experiences a phase transition from superparamagnetic to ferromagnetic-like state. The hysteresis curve has an immeasurable coercivity at room temperature while it exhibits a coercivity of 274 Oe at 10 K.

Below the transition temperature, the sample shows ferrimagnetic behavior with an increase in remnant magnetization (M_r) and coercivity (H_c). An external field is required to bring the total sample moment to zero since the thermal energy of the system (k_BT) is less than the energy barrier and there is no other mechanism other than the external field to rotate the particle/domain orientations to randomize the system. In the paramagnetic phase, k_BT is greater than the energy barrier, and thus thermal energy can ‘‘randomize’’ the system and bring the average moment to zero. It is naturally expected that H_c and M_r are greater than zero for ferrimagnetic and zero for superparamagnetic systems [118]. M_r also changes with the temperature: the area under M-H curve, which is the work done by the magnetic field, also changes. In the superparamagnetic case, given the fact that k_BT is greater than the energy barrier, only thermal energy is required to reorient the domains/particles and thus diminishing hysteresis is observed as expected in the superparamagnetic behavior. At room temperature, the absence of hysteresis,

immesurable M_r and H_c, and the no saturation at a high field of 5 kOe indicate the presence of superparamagnetic behavior at temperatures T ≥ 300 K.

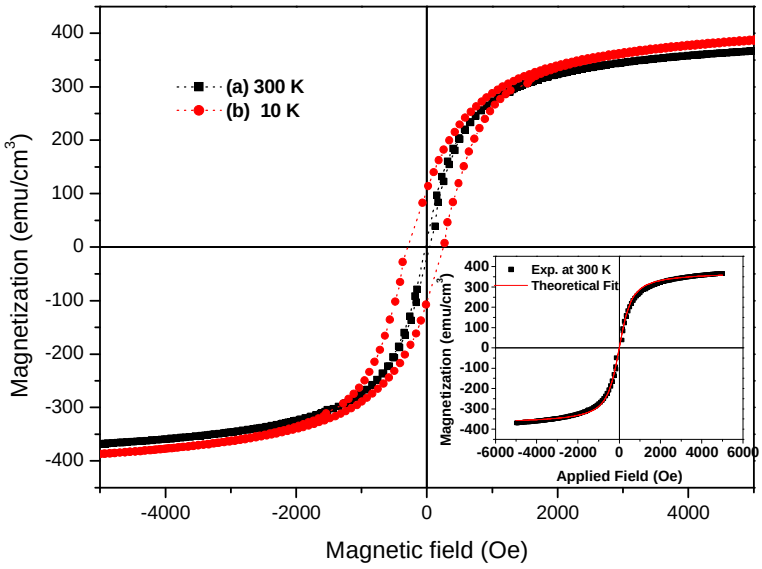

Figure 3.4. Magnetization versus magnetic field curves for iron oxide nanoparticles at (a) 300 K and (b) 10 K. The inset shows experimental (solid rectangle) and calculated (solid line) data representing the best fit for the Langevin function (Eqn.1) for iron oxide nanoparticles at 300 K.

The magnetic domain size can be calculated from these magnetization curves using the following formula [119]:

$$D_m = \left(\frac{18 k_B T}{\pi} \frac{\chi_i}{M_s^2} \right) \qquad (2)$$

where, χ_i is the initial magnetic susceptibility $\chi_i = \left(\frac{dM}{dH} \right)_{H \to 0}$ and ρ is the density of Fe_3O_4 (5.18 g/cm^3). The initial slope near the origin was determined from the hysteresis plots by curve-fitting the linear portion (H~0) of the magnetization data. The

saturation magnetization M_s is 390 emu/cm^3 at 300 K, shown in Fig. 3.4. Using this M_s value, a magnetic domain size D_m of 9.7 nm is obtained at 300 K for the sample.

For superparamagnetic particles, the true magnetic moment at a particular temperature can be calculated using the Langevin function [120]:

$$M = M_s\left(\coth(\frac{\mu H}{k_B T}) - \frac{k_B T}{\mu H}\right) \quad (3)$$

where ($\mu = M_s \pi D^3 / 6$) is the true (total) magnetic moment of each particle, k_B is the Boltzmann constant, T is the absolute temperature and M_s is the saturation magnetization. The simulated data obtained by using the Langevin function in Eq. (2) are also given in inset in Fig. 3.4. There is a near perfect fit between experimental and theoretical values. The mean-magnetic moment per particle is found to be 19300 μ_B from this simulation.

The M_s of bulk Fe_3O_4 is reported to be 500 emu/cm^3 at room temperature [112,113], however, our sample shows an M_s of ~70 % of its theoretical bulk value. Moreover, the domain size of the sample determined from the magnetization curve by using Eq. 2 is 12% smaller than the physical size determined from XRD and TEM techniques. Two possibilities could explain these differences: First possibility is related to the stoichiometry, that is, chemical composition of nanoparticles varies from Fe_3O_4 to γ-Fe_2O_3. Maghemite (γ-Fe_2O_3) has a magnetic moment of 2.3 μ_B per unit molecule while that of magnetite is 4.1 μ_B per unit molecule [111]. Therefore transformation of magnetite to maghemite might cause the decrease in the average saturation magnetization. The second possibility is the finite size effects on the magnetic properties of nanoparticles of magnetite and other ferrites [110, 121-124]. In this case, the decrease of M_S value in nanoparticles can be attributed to the canted spins in the surface layers due to a decrease in the exchange coupling which is caused by the lack of oxygen mediating super exchange mechanism between nearest iron ions at the surface. Thus magnetically dead surface layers can appear [121,125]. Since 30% of the magnetic ions lie within the outer shell of thickness about four atomic layers (around 6.5 Å), this

dead layer can account for the decrease of saturation magnetization down to 70% of that of the bulk samples. This means that as the particles become smaller (or magnetically disordered) the dead layer shell could entirely dominate over the magnetic property of the single domain nano-particles.

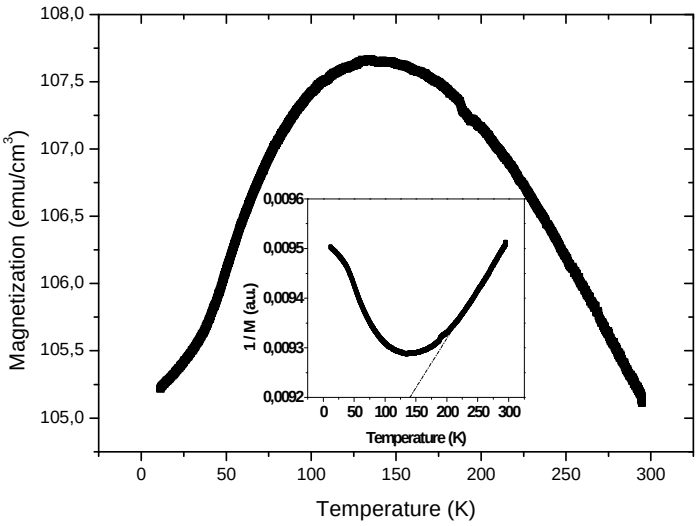

Figure 3.5 M-T curves for as-synthesized iron oxide nanoparticles recorded in the presence of 200 Oe field.

The temperature dependence of magnetization (Fig. 3.5) of nanoparticles exhibits a cusp that corresponds to the blocking temperature, T_B around 134 K. There are various T_B values reported for magnetite nanoparticles prepared by different techniques. Shufeng et. al. [126] reported monodisperse magnetite nanoparticles with an average diameter of 12.7 nm, synthesized via the reaction between Fe powder and $FeCl_3.6H_2O$, exhibited a T_B of 95 K. Magnetite nanoparticles with an average diameter of 13 nm, synthesized via a facile room temperature coprecipitation route in the presence of poly(vinyl pyrrolidone) (PVP), has been reported to have a T_B of 140 K [127]. Yanglong Hou et al. [128] reported T_B of 180 K and 225 K for magnetite nanoparticles, synthesized by solvothermal reduction, with average diameters of 8 and 11 nm respectively. The difference in T_B is attributed to the size difference and the existence of a broadened distribution of energy barriers. Furthermore, Kim et. al. [129] reported T_B of 150 K for 6 nm Fe_3O_4 particles, synthesized by solution chemical method. They studied the effect of surface coating on the blocking temperature. Without

coating, due to the increase in the surface area to volume ratio, the attractive force between nanoparticles will increase, and agglomeration of the nanoparticles will take place. These agglomerated nanoparticles act as a cluster, resulting in an increase of the blocking temperature. Measured T_B of 134 K for iron oxide nanoparticles synthesized in this work is in agreement with literature values for comparable sized magnetic nanoparticles [129].

As it is well known, above T_B, superparamagnetic (giant) moment of particles becomes thermally unstable and magnetizations exponentially decrease as $M_V.H/k_BT$ become smaller than 1. The superparamagnetic particles deflect uniquely to the strong field side of the gradient magnet, but this effect decreases as a function of increasing temperature. Above the blocking temperature T_B, the thermal fluctuation energy (k_BT) is larger than the uniaxial anisotropy energy (KV), because the critical volume for nanoparticles behaving as a single domain is larger than the studied magnetic particles [130]. At high temperature regime, assuming an equilibrium state, the magnetic susceptibility follows a Curie-Weiss law [131] with a ferromagnetic transition temperature T_c. H_c and M_r have shown superparamagnetic behaviors by increasing the temperature above the blocking temperature. Below the blocking temperature, T_B, the uniaxial anisotropy energy (KV) is larger than the thermal fluctuation energy (k_BT) and the magnetic moments of the particles are magnetically frozen along their anisotropy axes. Consequently, the magnetization of the nanoparticles has a hysteretic feature. The decrease in magnetization below T_B should be attributed to this spin frustration in spin-glass like phase. A spin glass like ordering of magnetic moments may be thought of for the random distribution of magnetic dipoles. This is consistent with spin-canting due to the decrease in effective super exchange interactions among magnetic spins at the surface regions, which reflects itself as 30% decrease of average magnetization of single particle domain as mentioned above.

The inset in Fig. 3.5 shows the temperature dependence of inverse magnetization. The inverse magnetization varies almost linearly in the temperature range of 200-300 K indicating super-paramagnetic nature of iron oxide nanoparticles. The straight line extrapolation to 0 K yields finite intercept on the positive 1/M axis. However, for an assembly of non-interacting single domain particles in the superparamagnetic regime the susceptibility is usually expressed by the simplified

Langevin function, $\chi = \mu^2_{ave}/3k_BT$, where μ_{ave} is the mean particle moment; and k_B is the Boltzmann's constant. These results indicate the existence of interparticle interactions in the thermomagnetic characteristics of Fe_3O_4 spinels at lower field strengths.

3.1.2 Fe_3O_4 nanoparticles by hydrothermal synthesis *(Tev9 & Tev19)*

3.1.2.1 XRD analysis

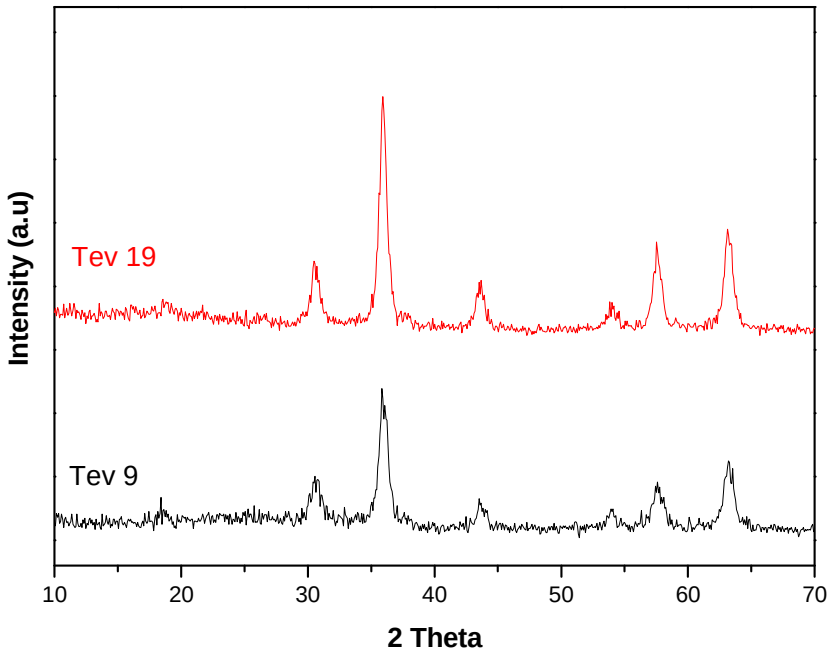

Figure 3.6 XRD patterns of Fe_3O_4 nanoparticles with and without CTAB.

Iron oxide was identified from the XRD pattern of, as shown in Figure 3.6 and 3.7 with peak positions at 30.00 (2 2 0), 35.5 (3 1 1), 43.1 (4 0 0), 53.4 (4 2 2), 57 (5 1 1), and 63 (4 4 0). These characteristic peaks correspond very well to standard card of magnetite (JCPDS card no 19-629). The patterns showed that the samples are pure Fe_3O_4 without impurity phases. However, the reflection peaks become sharper and narrower along with the increasing hydrothermal temperature, indicating the improvement of crystallinity. The particle size were calculated using Debye-Scherrer

formula from the reflection of (3 1 1). The average particle sizes of Tev9 and Tev19 were 10.71 and 11.95 nm respectively.

3.1.2.2 FTIR analysis

The singlets at 962 cm^{-1} for pure CTAB and 1004 cm^{-1} for bond CTAB belong to C-N^{+} stretching bands, and the frequency shift is believed to be caused also bay interactions between N-containing group and the metal surface. The change of CH_2 rocking mode from a doublet at 730 and 719 cm^{-1} for pure CTAB to a singlet at 717 cm^{-1} in the product also denotes a confinement effect of CTAB in capping structure (Fig.3.7). All these experimental observations illuminate that CTAB molecules cap Fe_3O_4 via their headgroups.

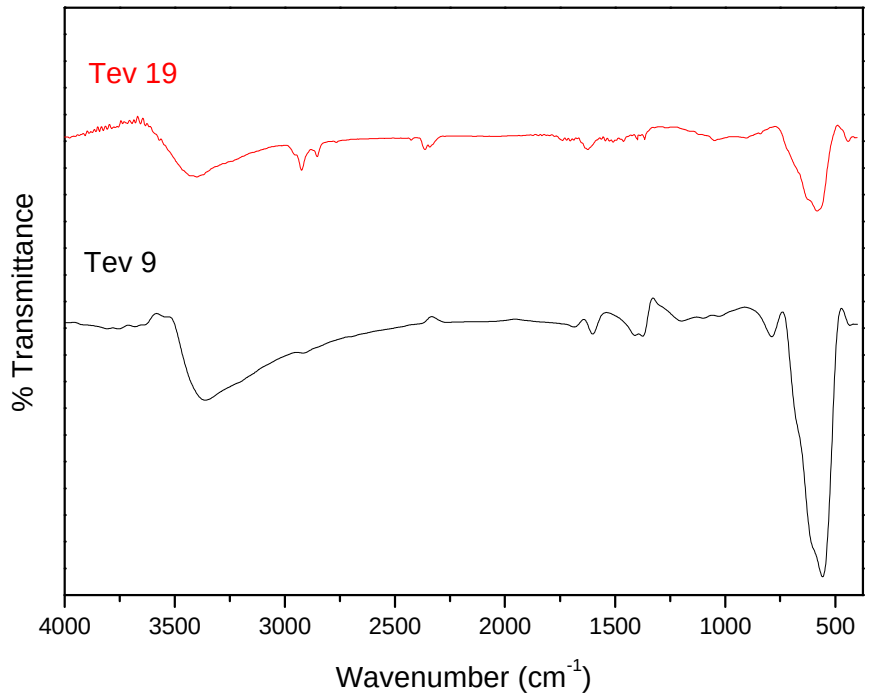

Figure 3.7. FTIR spectra of Fe_3O_4 nanoparticles with (Tev19) and without CTAB (Tev9).

3.1.2.3 SEM & TEM analysis

TEM and SEM micrographs of the two products are given in Fig.8-Fig.11. According to TEM, the product which was obtained without CTAB (Tev9) has a hexagonal shape and with CTAB (Tev19) somehow nanorod shape is true.

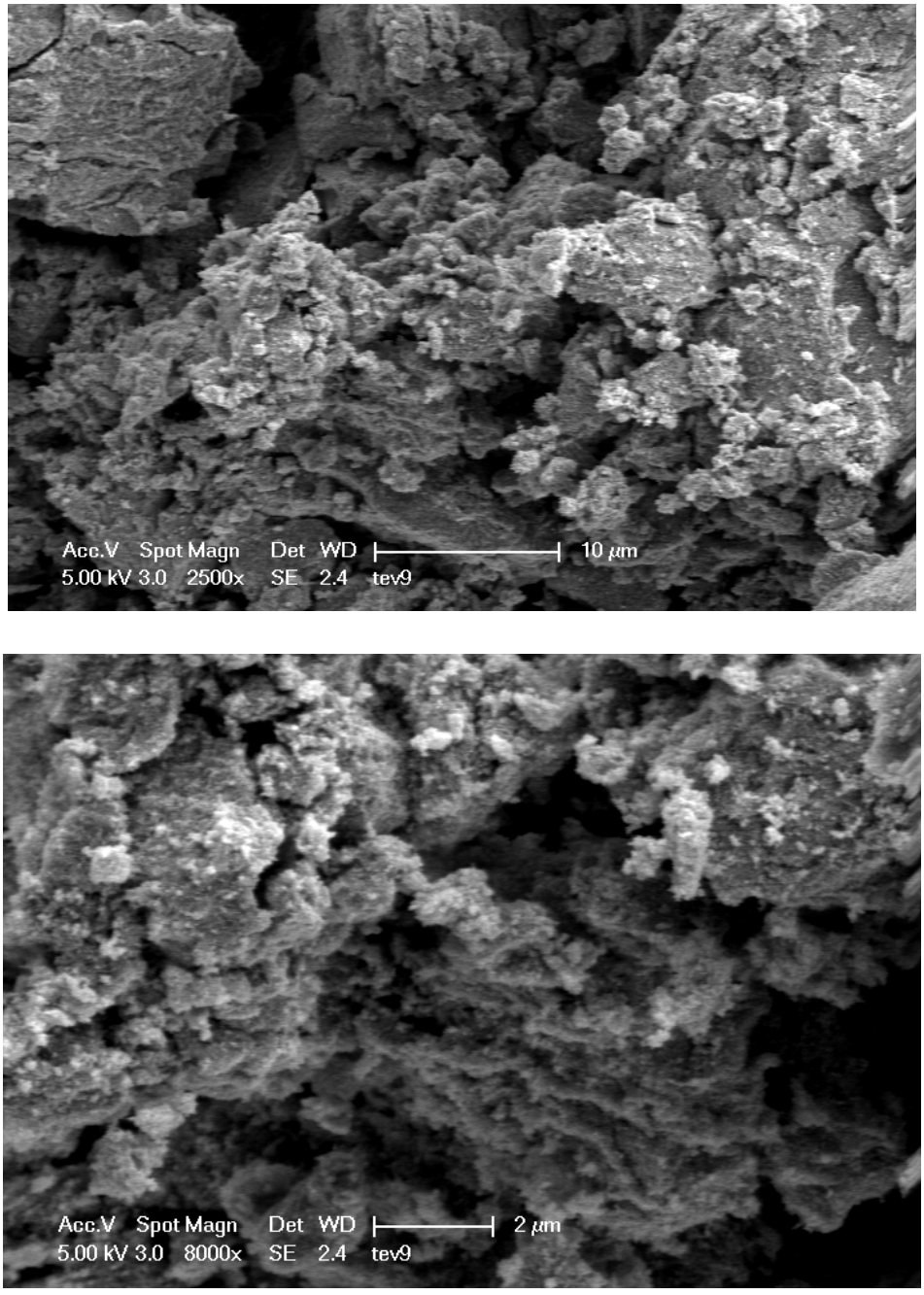

Figure 3.8. SEM micrographs iron oxide nanoparticles without CTAB (Tev9).

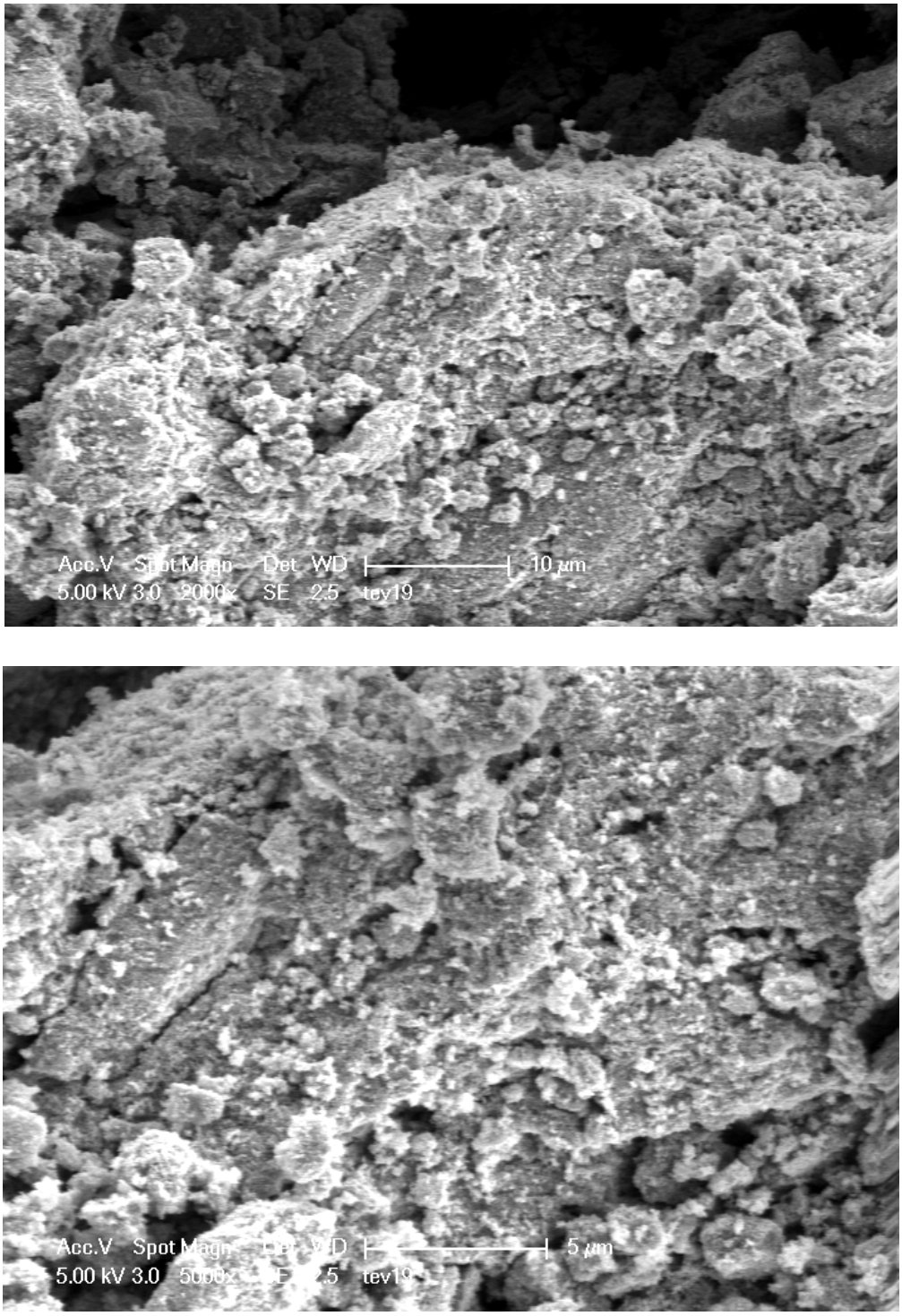

Figure 3.9. SEM micrographs iron oxide nanoparticles with CTAB (Tev19).

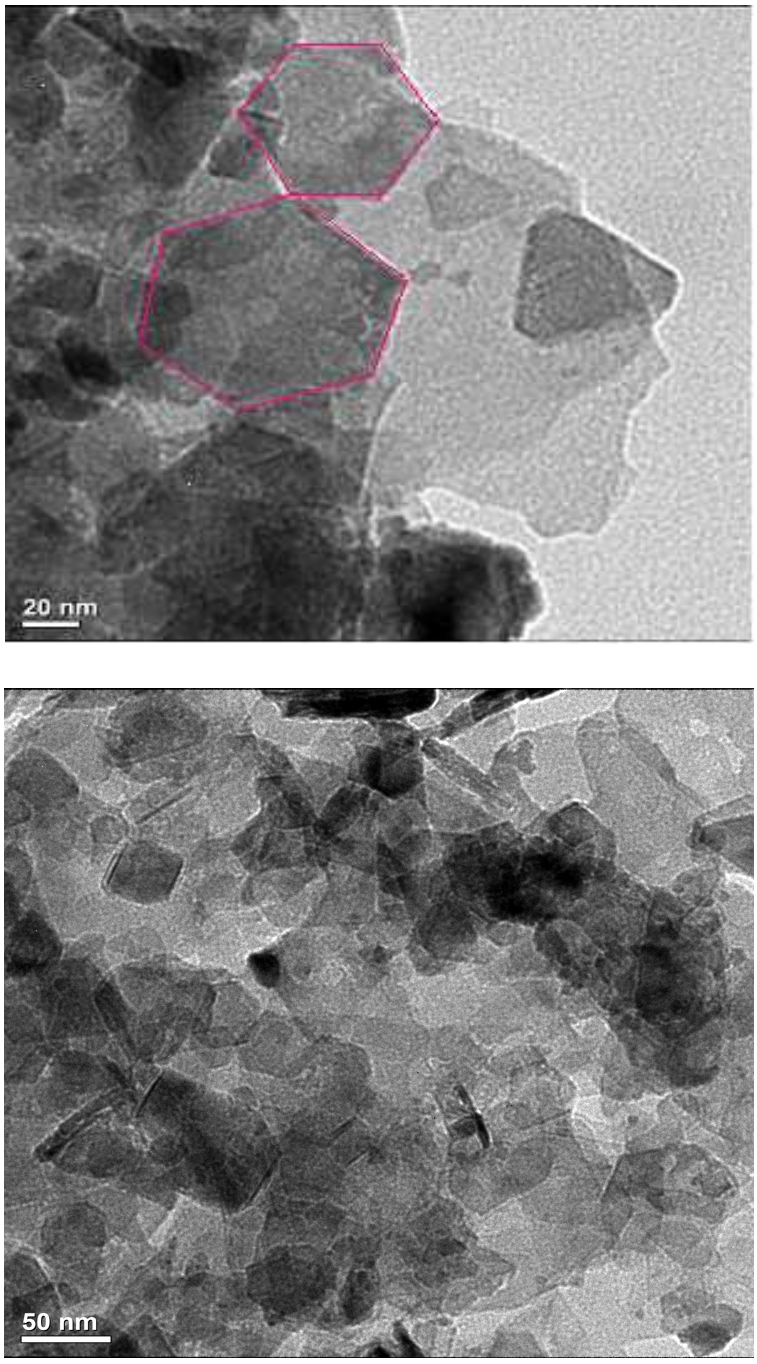

Figure 3.10. TEM micrographs of iron oxide nanoparticles without CTAB (Tev9).

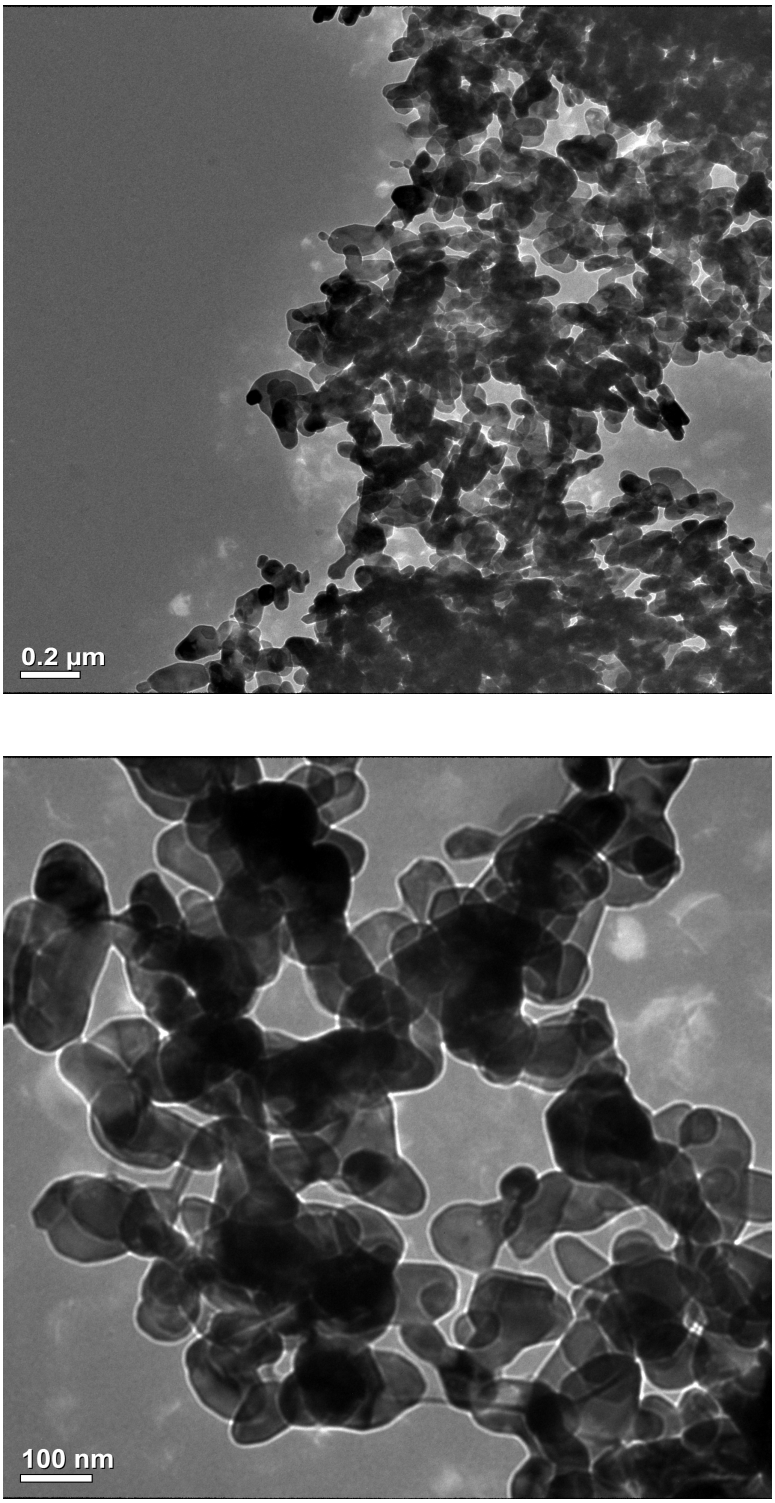

Figure 3.11. TEM micrograph iron oxide nanoparticles with CTAB (Tev19).

3.1.3 Fe_3O_4 nanoparticles by oxidation-reduction method (Tev14a & Tev25)

3.1.3.1 XRD analysis

Phase investigation of the crystallized products was performed by XRD and the patterns are shown in Fig. 3.12. The XRD patterns indicate that the products are iron oxide, Fe_3O_4. All the observed diffraction peaks could be indexed by the cubic structure of Fe_3O_4 (JCPDS no 19-629) indicating a high phase purity of iron oxide. The crystallite size of the samples were calculated with the Scherrer's equation, and the average diameters of nanoparticles by NaOH and NH_3 are 37.96 and 33.13 nm respectively.

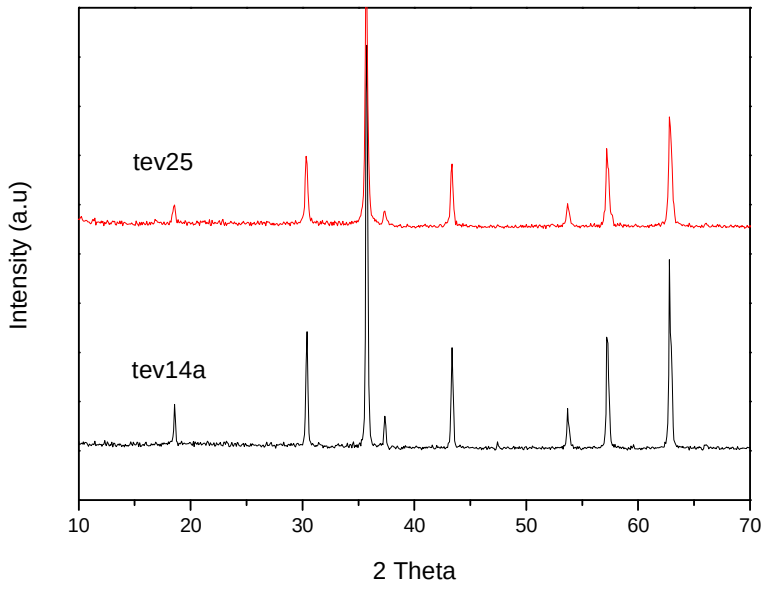

Figure 3.12 X-ray powder diffraction patterns of Fe_3O_4 nanoparticles.

For Tev25, we used NH_4OH instead of NaOH. Ammonia is not a strong base, where as sodium hydroxide is a strong base. The increase in the pH will increase the crystallinity of the product [132].

3.1.3.2 FTIR analysis

The FTIR spectra of as synthesized Fe_3O_4 nanocrystals are shown in Fig.3.13 (Tev14a & Tev25). As prepared powder presents characteristic peaks that are exhibited by the commercial magnetite powder: metal-oxygen band, v_1, observed at 590 cm^{-1} corresponds to intrinsic stretching vibrations of the metal at tetrahedral site ($Fe_{tetra}\leftrightarrow O$), whereas metal-oxygen band observed at 445 cm^{-1}, v_2, is assigned to octahedral-metal stretching ($Fe_{octa}\leftrightarrow O$) [105,133,134].

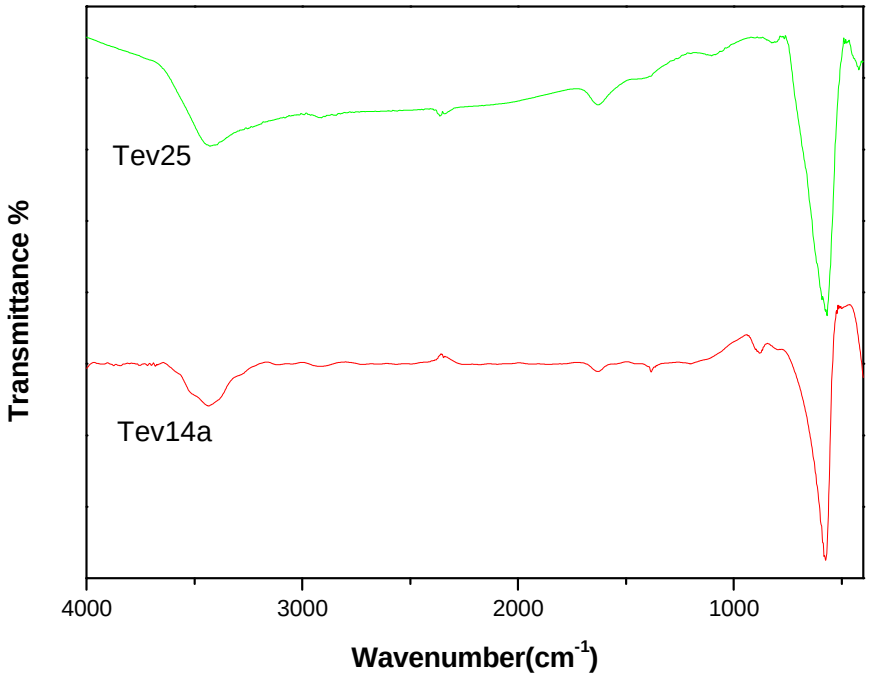

Figure 3.13. FTIR spectra of Fe_3O_4 nanoparticles.

3.1.4 Fe_3O_4 nanoparticles by PEG-asisted route (Te2 & Te3)

3.1.4.1 XRD analysis

Phase investigation of the crystallized product was performed by XRD and the pattern is shown in Fig. 3.14. The XRD pattern indicates that the product is iron oxide, Fe_3O_4, and the diffraction peaks are broadened owing to small crystallite size. All the observed diffraction peaks could be indexed by the cubic structure of Fe_3O_4 (JCPDS no 19-629) indicating a high phase purity of iron oxide. The crystallite size of the samples were calculated with the Scherrer's equation, and the average diameters of nanoparticles by NaOH and NH_3 are 8.71 and 10.68 nm respectively.

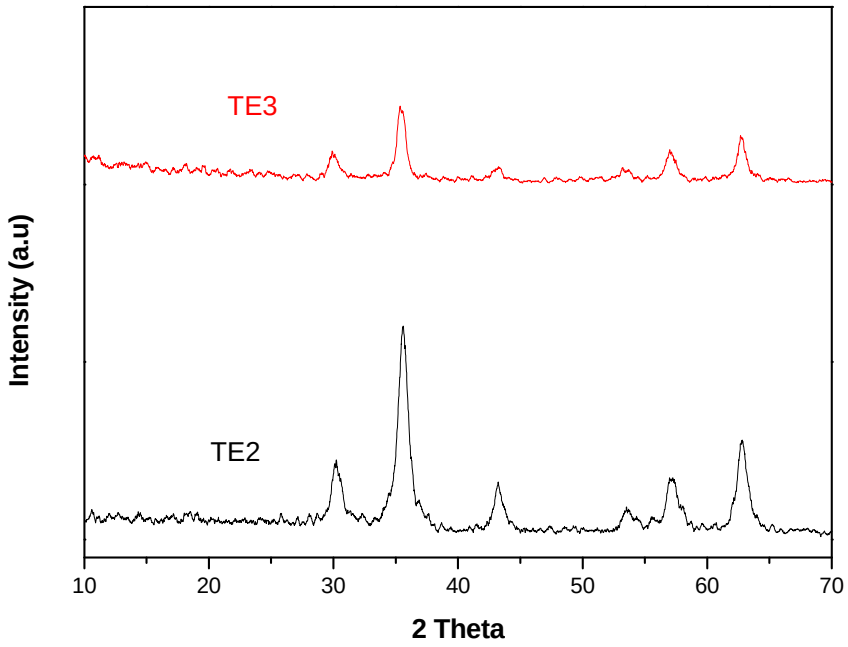

Figure 3.14. X-ray powder diffraction patterns of PEG-Fe_3O_4 nanoparticles.

3.1.4.2 FTIR analysis

FTIR spectra of commercial Fe_3O_4 powder and as synthesized Fe_3O_4 nanocrystals are shown in Fig.3.15. As prepared powder presents characteristic peaks that are exhibited by the commercial magnetite powder: metal-oxygen band, observed at v_1 (590 cm^{-1}) corresponds to intrinsic stretching vibrations of the metal at tetrahedral site (Fe_{tetra}↔O), whereas metal-oxygen band observed at v_2 (445 cm^{-1}) is assigned to octahedral-metal stretching (Fe_{octa}↔O) [105,133,134]. The presence of C-O (~1106 cm^{-1}), -CH_2 (~2900 cm^{-1}) and –CH (~2800 cm^{-1}) peaks were strong evidence that PEG was chemically bonded to the surface of nanoparticles.

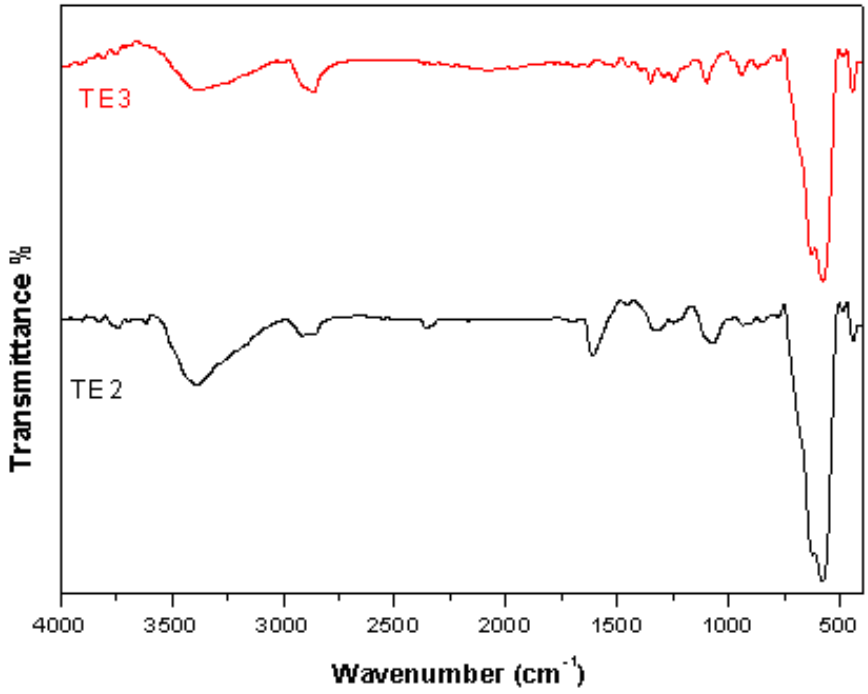

Figure 3.15. FTIR spectra of PEG-Fe_3O_4 nanoparticles.

3.2. Co_3O_4 analysis

3.2.1. Co_3O_4 nanoparticles reflux and oxidation-reduction method *(Tev37 & Tev11b)*

Alkalization reaction of cobalt ions has been extensively studied by Refait and Olowe [95,96] and they proposed the following reactions for the mechanism of formation of Co_3O_4.

$$Co^{2+} + 2NaOH^{-} \rightarrow Co(OH)_2 + Na_2SO_4 \quad [1]$$

$$3Co(OH)_2 + NO_3^{-} \rightarrow Co(OH)_2 + 2CoOOH + H_2O + NO_2 \quad [2]$$

$$Co(OH)_2 + 2CoOOH \rightarrow Co_3O_4 + 2H_2O \quad [3]$$

Thus, in the synthesis with ferrous ions alone, as in our case, Co_3O_4 is formed as a result of the dehydration reaction of cobalt hydroxide and cobalt oxyhydroxide (reaction 3) in which the latter compound is produced by the partial oxidation of cobalt hydroxide by O_2 dissolved in air (reaction 2). This is the mechanism controlling the transformation of cobalt hydroxide phases to the final phase of Co_3O_4.

3.2.1.1. XRD Analysis

XRD analysis performed on the nanoparticles obtained by two different methods revealed that the only phase observed was Co_3O_4 spinel oxide nanoparticles with ICDD card no of 42-1467. No secondary phases or impurities were observed.

We use the diffraction profile fitting to estimate the size using eqn.1 in Wejrzanowski et.al. [103,104]. The line profile, shown in Fig.3.16, is fitted for 9 peaks (111, 220, 311, 400, 422, 511, 440, 620 and 533) and the average crystallite size, *D* and σ, is estimated as 28±7 nm and 30±6 nm, respectively.

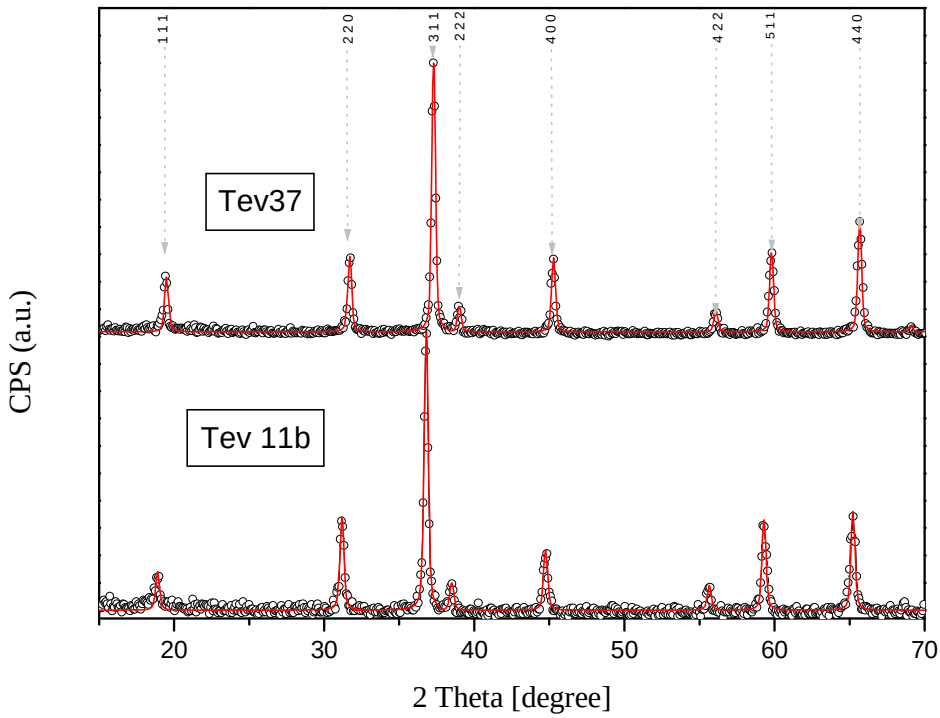

Figure 3.16. XRD patterns of Co_3O_4 nanoparticles with the line profiles fitting.

3.2.1.2. FTIR Analysis

The FTIR spectra of Tev11b and Tev37 are represented in Fig.3.17. The IR bands at 1384 cm^{-1} can be assigned to ν_1 vibration of carbondioxide molecule [134]. The IR spectrum displays two distinct and sharp bands at ν_1 (578 cm^{-1}) and ν_1 (662 cm^{-1}), which originate from the stretching vibrations of the metal-oxygen bond and confirm the formation of Co_3O_4 spinel oxide also. [135-137]. The ν_1 band is characteristic of Co^{3+} vibration in the octahedral hole, and ν_2 bans is attributable Co^{2+} vibration in tetrahedral hole in the spinel lattice [138]. In the range of 4000–1000 cm^{-1}, vibrations of CO_3^{2-} , NO_3^- and moisture were observed. The intensive broadband at 3450 cm^{-1} and the less intensive band at 1620 cm^{-1} bending are due to O–H stretching vibration interacting through H bonds. Traces of adsorbed or atmospheric CO_2 are evidenced by the very

small absorption peak around 2340 cm^{-1}. The ν (C=O) stretching vibration of the carboxylate group (CO_2^-) is observed around 1380 cm^{-1}.

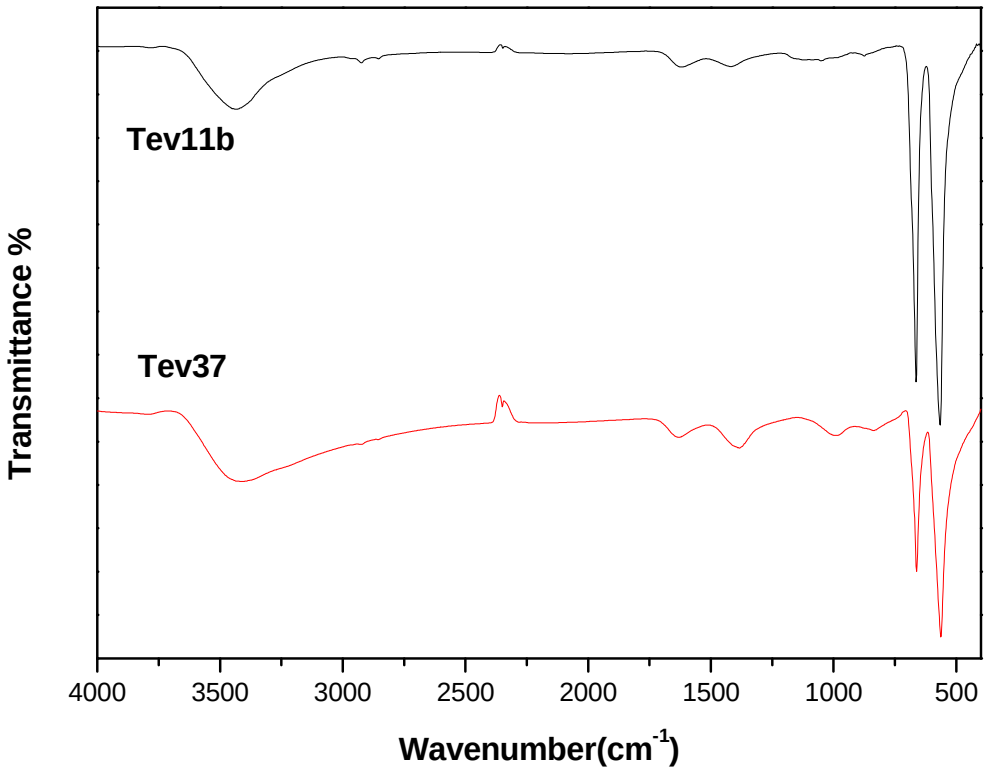

Figure 3.17. FTIR spectra of Co_3O_4 nanoparticles prepared by reflux method (Tev37) and oxidation- reduction method (Tev11b).

3.2.1.3. SEM & TEM analysis

TEM and SEM micrographs of the two products are given in Fig.18-Fig.21. According to TEM, in Fig. 3.20 has a hexagonal shape with reflux method (Tev11b).

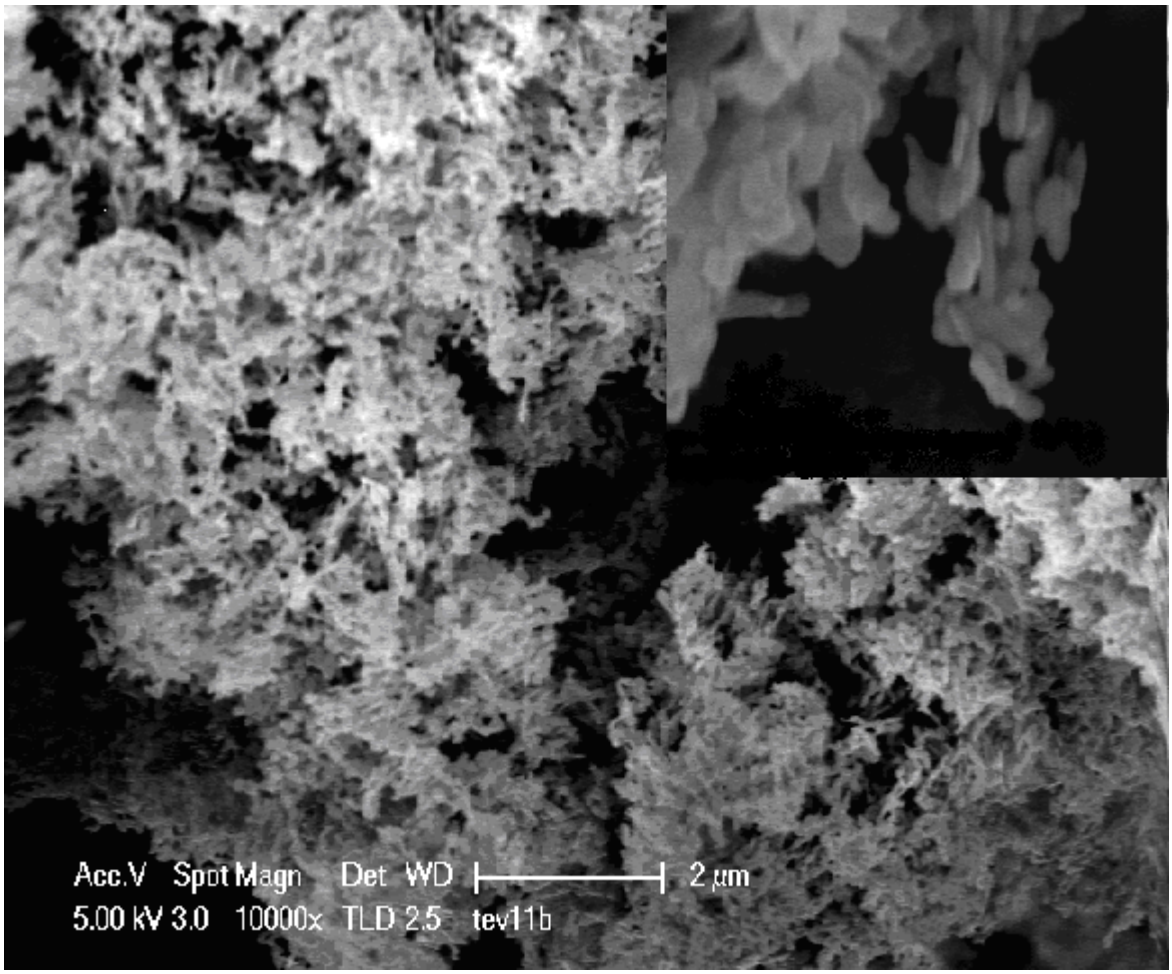

Figure 3.18. SEM micrographs of Co_3O_4 nanoparticles prepared by reflux method (Tev11b).

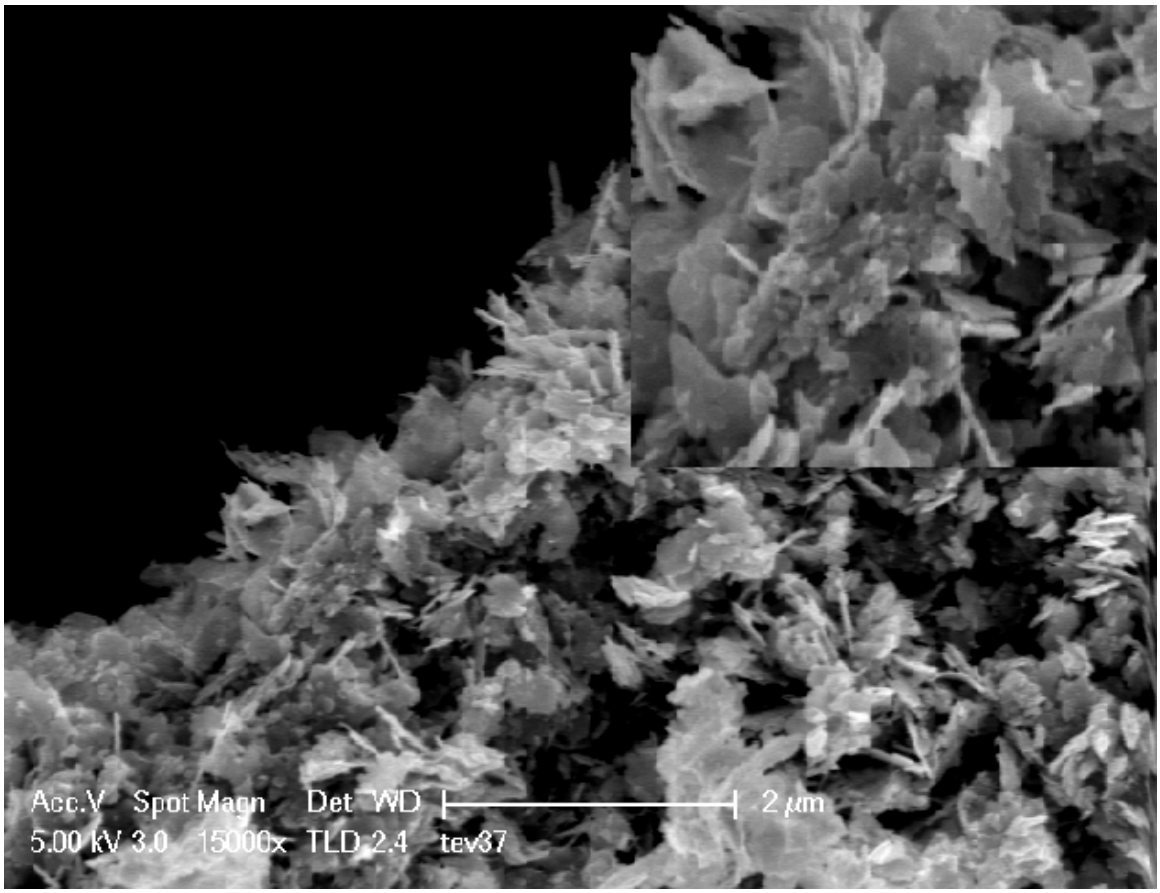

Figure 3.19. SEM micrographs of Co_3O_4 nanoparticles prepared by oxidation-reduction method (Tev37).

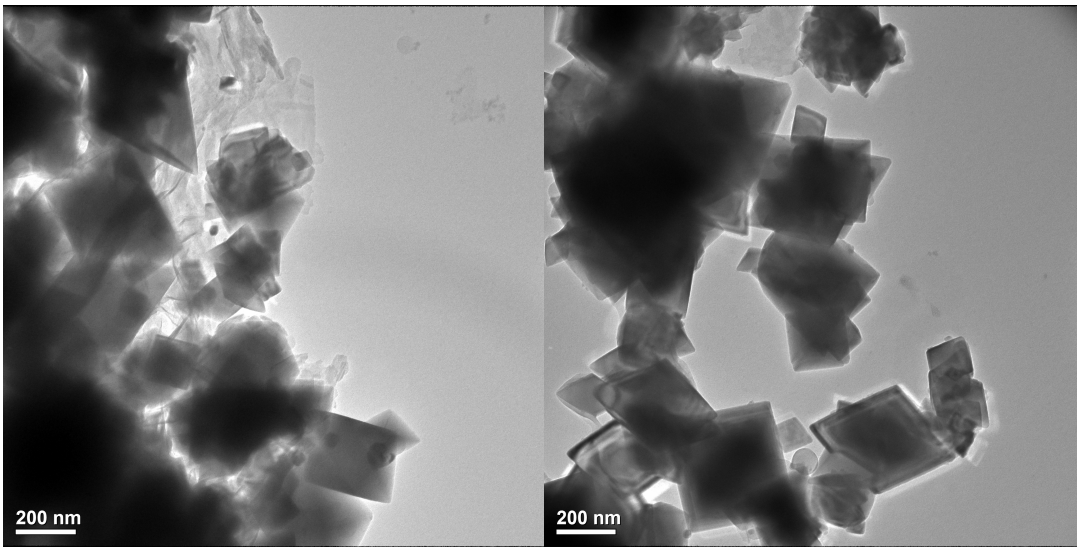

Figure 3.20. TEM micrographs of Co_3O_4 nanoparticles prepared by reflux method (Tev11b).

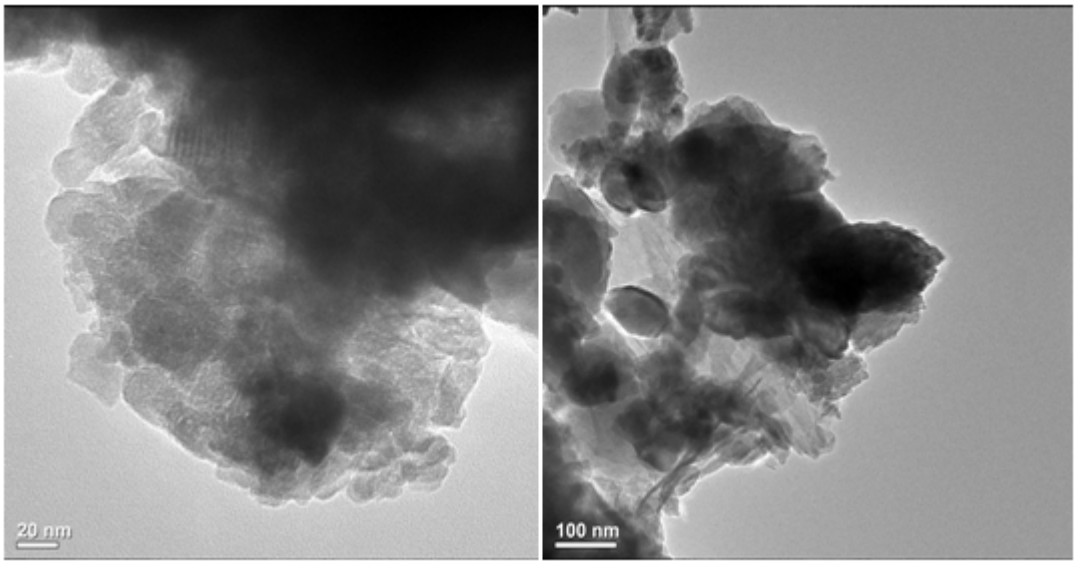

Figure 3.21. TEM micrographs of Co_3O_4 nanoparticles prepared by oxidation-reduction method (Tev37).

3.2.1.4. Magnetization

Magnetic measurements performed on Co_3O_4 nanoparticles prepared by (a) reflux method (Tev11b), (b) oxidation-reduction method (Tev37) are presented in Fig. 3.22 and 3.23. As it is seen from Fig.3.22, the room temperature M-H curves are linear with the field and has no coercivity and remenance. The samples can't reach the saturation even in the presence of 5 kOe magnetic field. Comparatively large coercivity and shifted hysteresis loops at 10 K are observed after field cooling (see Fig.3.23).

The loops are broadened and shifted in opposite to the cooling field direction; with coercive fields of 295 and 102 Oe, respectively. The loops are open up to 8 kOe and the magnetization is almost linear with the field. For a system with an open loop up to high field indicates the existence of high surface anisotropy and a spin-glass-like surface layer.

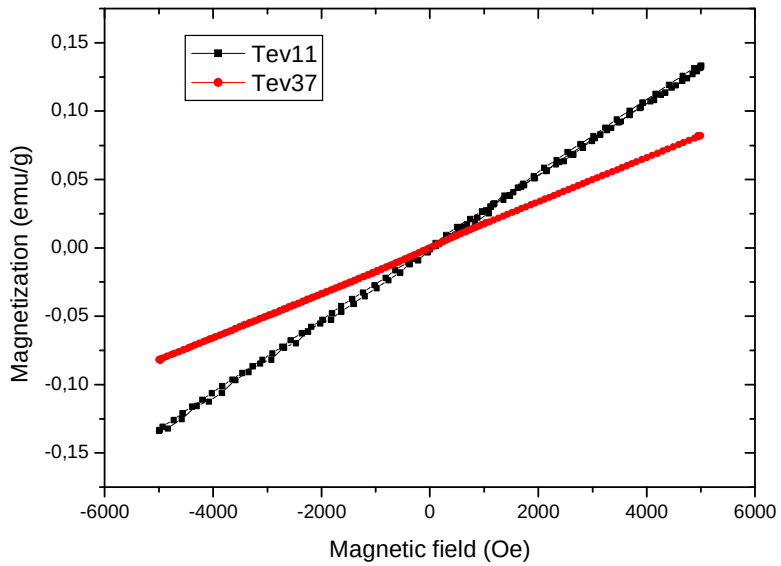

Figure 3.22. Room temperature M-H Curves of sample Tev11 (27nm) and Tev37 (29.730 nm).

When a sample is cooled through the antiferromagnetic (AF) Neel temperature in the presence of an applied field, the ferromagnetic (FM) layer displays a unidirectional anisotropy resulting in a shift of the hysteresis loop from zero on the field axis by an amout of exchange field, H_e. This exchange field could be attributed to the exchange coupling of the frozen moments associated with uncompansated surface spins and the AF core [140]. The loops are open up to 7.5 kOe and the magnetization increases almost linearly with applied field at higher fields up to 10 kOe. Also the magnetization of both samples can not reach the saturation even in the presence of 10 kOe magnetic field.

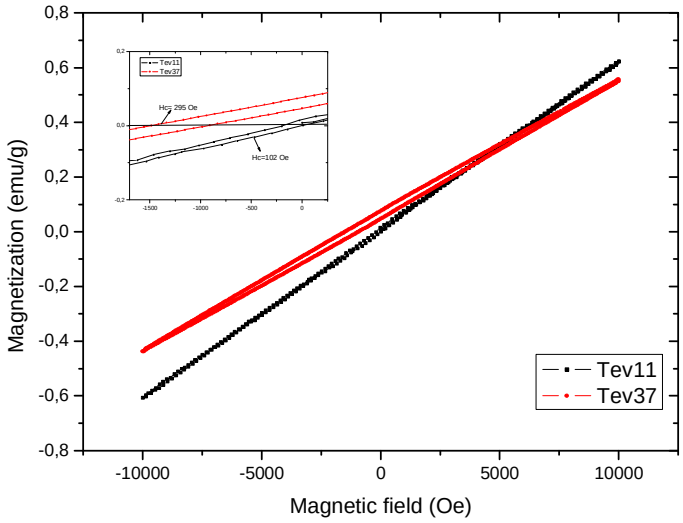

Figure 3.23. M-H Curve of sample Tev11 (27 nm) and Tev37 (29.7 nm) at 10 K. The inset shows an expansion of the central portions.

Fig.3.24 shows central portions of the FC loops at 10 K. The loops are broadened and shifted toward negative applied field, which exhibits the typical feature of an exchange bias system with an exchange bias field $H_{eb} = \left(H_{C1}^{FC} + H_{C2}^{FC}\right)/2$ around -1223 Oe for Tev37 and -49 Oe for Tev11, respectively. The exchange bias is an interfacial effect by the exchange coupling between AFM and FM layers which induces a unidirectional anisotropy of the FM layer. Both the loop shift and exchange bias field are measures of the unidirectional exchange anisotropy. The observation of the loop shift, enhanced coercivity, as well as the exchange bias field indicates the existence of

the AFM core and FM surface spin in our Co_3O_4 nanoparticles, which can be attributed to the uncompansated surface spin due to the reduction of the coordination number at the surface of the AFM Co_3O_4 nanoparticles.

As for the opening of the loop, a spin-glass-like surface system with multiple spin configurations is believed to be its origin [141]. According to Salaba et al. [141], the surface spins can be separated into two parts. One part is the frozen-in uncompensated spins which do not reverse during the field cycling. The other part is the free spins which can be aligned by an applied field. Thus, in one cycle of loop measurement, part of the magnetization (the frozen-in spins) is lost, leading to the opening of the loop. The existence of the spin-glass-like surface phase can be further confirmed by the training effect of the exchange bias field.

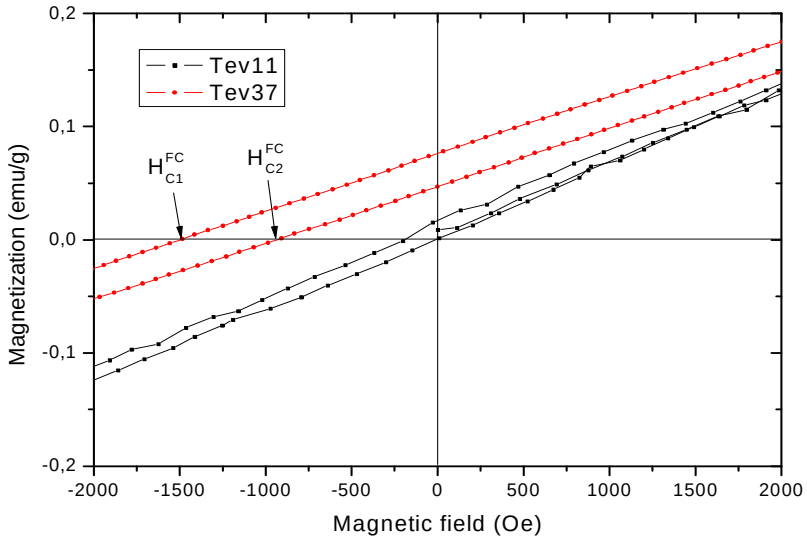

Figure 3.24. Central portions of FC hysteresis loops at low field showing an obvious loop shift.

It is known that Co_3O_4 has normal spinel structure with antiferromagnetic exchange between ions occupying tetrahedral A sites and octahedral B sites. From the neutron diffraction experiments it is found that the Co^{3+} ions have no moment on B sites and Co^{2+} ions on A sites have permanent moment of 3.25 μB [142].

Temperature dependence of the magnetization of samples in 200 Oe field-cooled (FC) cases are shown in Fig. 3.25 and 3.26. As seen in each FC curve, the

magnetization of the sample is slightly increases by the decrease of temperature down to 40 K and strongly increased at lower temperatures. For higher temperature region, $T \geq 40$ K, the plots of 1/M vs. T are linear indicating that the magnetizations of Tev11 and Tev37 obey the Curie–Weiss law with a negative θ value about 17 K and 110 K, respectively, while the Néel temperature of Co_3O_4 bulk crystal was known as $T_N = 33$ K [143]. This change of transition temperature may be ascribed to smaller particle size indicating a finite size effect of phase transition of present system. Simply applying the relation between anisotropy energy and thermal fluctuation $KV = k_BT$ to this case, particle size near the transition temperature, $T_t \approx 40$ K could be estimated as about 3.52 nm, assuming $K \approx 105$ J/m^3 though exact anisotropy constant is unknown [144].

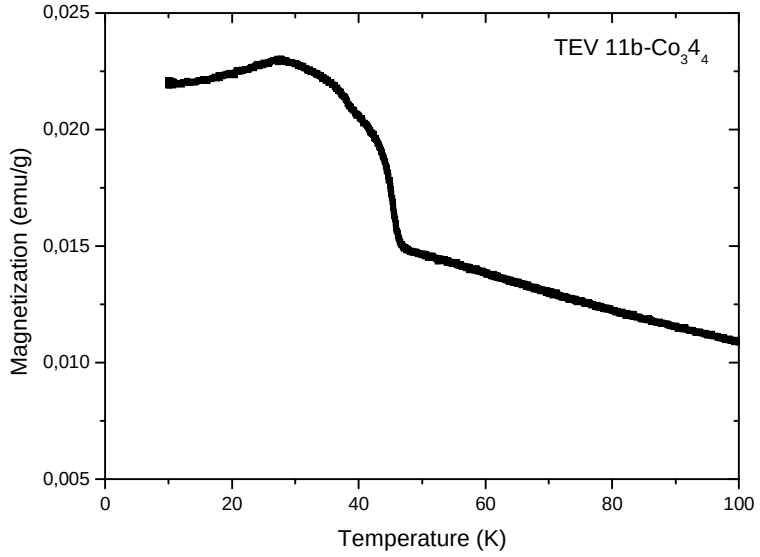

Figure 3.25. M-T curves of sample Tev11b with 200 Oe applied field.

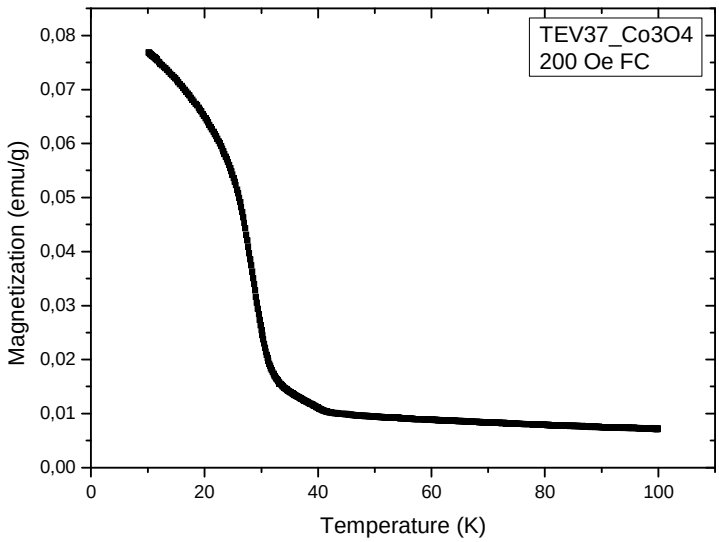

Figure 3.26. M-T curves of sample Tev37 with 200 Oe applied field.

From the M–H and M-T curves, paramagnetic behavior above 40 K, superparamagnetic behavior near the transition temperature, Tt, and the ferromagnetic behavior with slight hysteresis below Tt were observed. Thus These behaviors should be due to the uncompensated surface spins on the extremely small particle systems. From the inverse susceptibility, extremely larger effective magnetic moment per ion of 8.12 μB than expected as 4.14 μB was estimated. This result could be due to the exchange mechanism of Co^{3+} ion in complex octahedral symmetry of Co_3O_4 nanoparticles.

3.2.2 Co_3O_4 Simple Route Using Egg White *(Te19)*

3.2.2.1 XRD analysis

A new simplified route to prepare nanocrystalline Co_3O_4 powder is proposed. Egg white proteins are well known for thier gelling, foaming and emulsifying characteristics, in addition to their high nutrition quality [145-147]. Due to its solubility in water and its

ability to associate with metal ions in solution, egg white has been used with metal ions in solution, egg white has been used as a binder cum gel for shaping material, particularly bulk and porous ceramics [148-150]. Most recently, it was used as a matrix for entrapment of aluminum ions to generate a gelled precursor which resulted in α – alumina particles with crystallite size of 15-80 nm [151]. The use of egg white simplifies the process and would provide another alternative process for the simple and economical synthesis of nanocrystalline ceramic particles [152].

XRD analysis performed on the obtained Co_3O_4 revealed that the only phase observed was Co_3O_4 spinel oxide nanopartciles with ICDD card no of 42-1467. No secondary phases or impurities were observed. (Fig.3.27). The sharpness of XRD peaks reveal high crystallinity of the nanoparticles [153]. The average crystallite diameter L, was estimated by the Scherrer equation from the full-width at half maximum (FWHM) of the most intense peak (3 1 1). Average particle size, assuming spherical morphology, was estimated to be 11.95 nm.

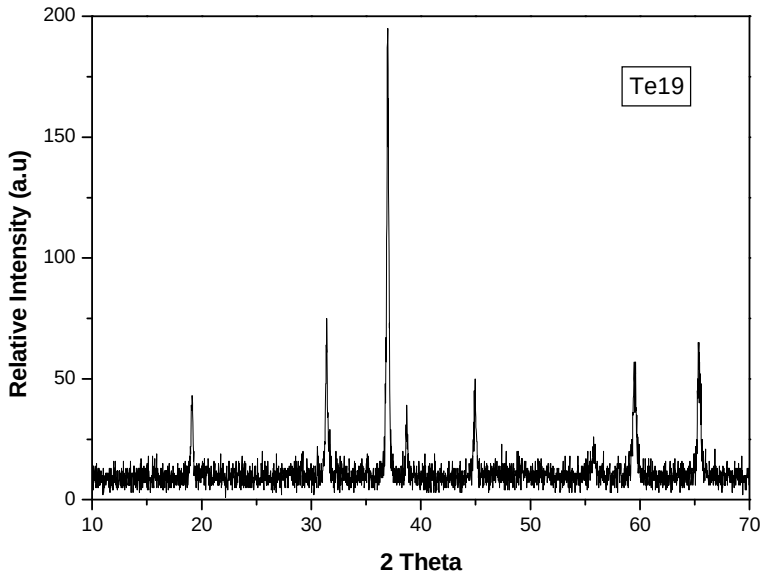

Figure 3.27 XRD Powder pattern of Co_3O_4 nanocrystals (Te19).

3.2.2.2 FTIR analysis

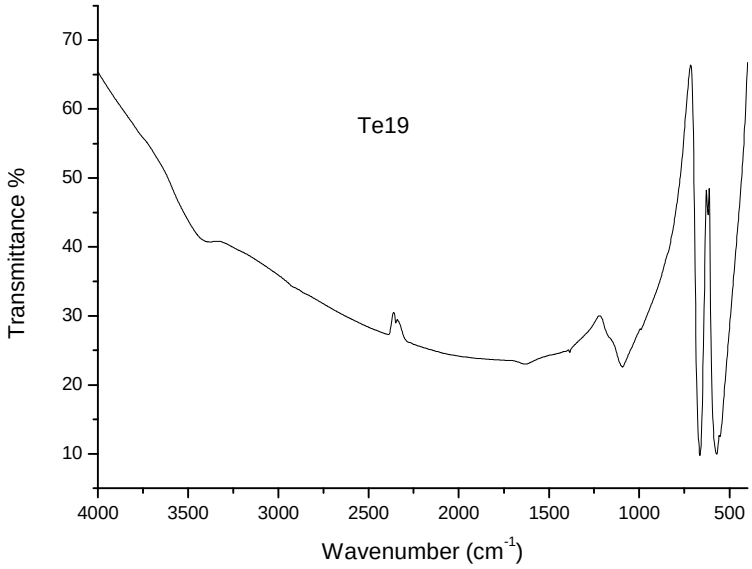

Figure 3.28. FTIR of Co_3O_4 nanocrystals (Te19).

The formation of the spinel Co_3O_4 structure was further supported by FT-IR spectra (Fig. 3.28). The intensive broadband at ~ 3450 cm^{-1} and the less intensive band at ~ 1620 cm^{-1} are due to O–H stretching vibration interacting through H bonds. Traces of adsorbed or atmospheric CO_2 are evidenced by the very small absorption peak around 2340 cm^{-1}. In the range of 1000–100 cm^{-1}, two main metal–oxygen bands at ~ 662 cm^{-1} (ν_1) and ~ 570 cm^{-1} (ν_2) were observed in the FT-IR spectra given in Fig.3.28. These two bands are usually assigned to vibration of ions in the crystal lattices. The band at ~ 662 cm^{-1} corresponds to intrinsic stretching vibrations of the metal at the tetrahedral site (Co↔O), whereas the band at ~ 397 cm^{-1} is assigned to octahedral-metal stretching (Co↔O) [154].

The gel formed by water - soluble egg white proteins serves as a perfect matrix for entrapment of metal ions that, upon the heat treatment, give rise to nanocrystalline Co_3O_4 powder.

3.3. Mn_3O_4 Analysis

3.3.1. Mn_3O_4 nanoparticles by thermal decomposition method *(Tev29)*[2]

Reaction scheme is presented in Fig.3.29, where acetyl acetone complex of Mn^{3+} and 2-pyrrolidone is refluxed at elevated temperatures, resulting in capped Mn_3O_4 particles.

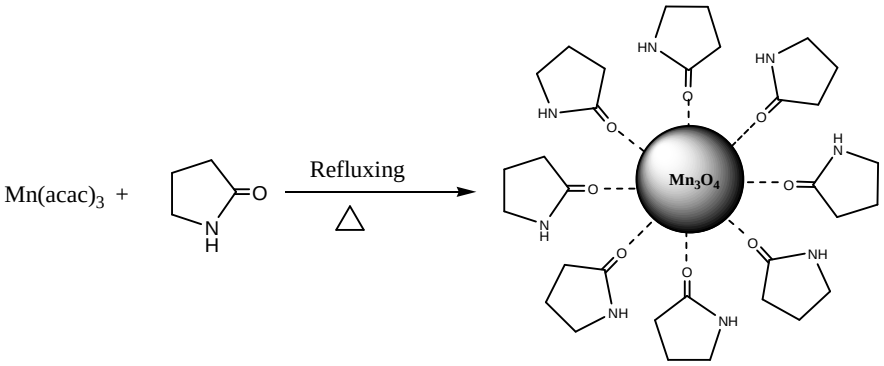

Figure 3.29. Reaction scheme for the synthesis of 2-pyrrolidone capped Mn_3O_4 nanoparticles.

The presence of alcohol is very important to initiate the particle formation. The rate of addition of alcohol affects the distribution of particle size. A stepwise addition results in a larger size and a wider size distribution, while a very fast addition results in a larger number of nuclei formed simultaneously thus yielding a narrower size distribution and better control over size. Refluxing the solution for extended periods before the addition of alcohol is effective in controlling the distribution of particle size.

3.3.1.1 XRD analysis

The X-ray powder diffraction pattern of the product is given in Figure 3.30. The XRD peaks attest to the formation of Mn_3O_4 as the major phase. All the experimental XRD peaks are in agreement with those reported in the literature for Mn_3O_4 (JCPDS card no 24-0734). Crystallite size was calculated from XRD peak broadening (i.e. full

[2] T. Ozkaya, A. Baykal,, M.S. Toprak, " **2-pyrrolidone - Capped Mn3O4 Nanocrystals" ,** CEJC, (inprint, 2008)

width at half maximum, FWHM) using the Scherrer equation as ~15 nm (based on 2 1 1 peak).

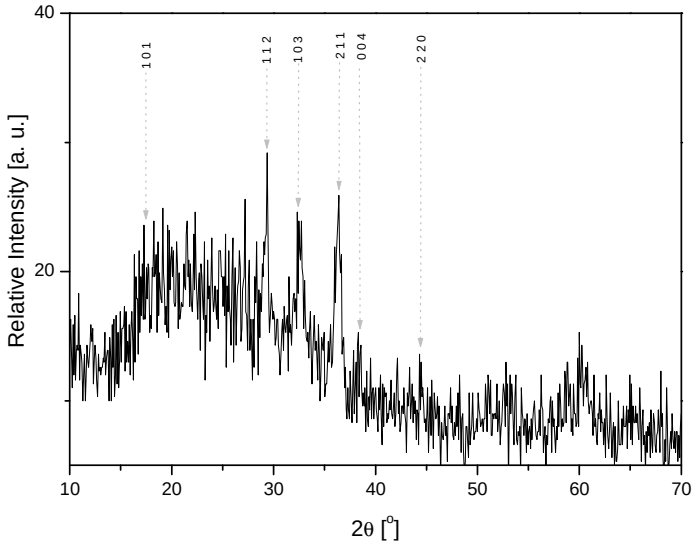

Figure 3.30. X-ray powder diffraction pattern of as-prepared capped Mn_3O_4 nanoparticles.

3.3.1.2 FTIR analysis

FTIR measurements were carried out on the pure 2-pyrrolidone and Mn_3O_4 nanoparticles capped with 2-pyrrolidone respectively: results are presented in Fig 3.31 and summarized in Table 1. A broad peak observed in the region 3000-3500 cm^{-1} originates from the overlap of amine groups and the stretching of the H bonded OH groups [155]. Hydrogen bonding is due to the conjugation of C=O group on 2-pyrrolidone with the OH bearing nanoparticles. The split of the peak into two is due to the N-H stretching vibrations of the unsubstituted amide groups on 2-pyrrolidone [156]. The broadness of the FTIR peak at around 3500 cm^{-1} also proves the existence of H-bonding among pyrrolidone molecules. The surfactant molecules in the adsorbed state were subject to the field of solid state nanoparticle surface. As a result the characteristic bands shifted to a lower frequency region and indicate that the surfactant surrounding the Mn_3O_4 nanoparticles are in a close-packed, crystalline state. It is worth noting that the C=O stretch band of pure 2-pyrrolidone which is present at 1679 cm^{-1} shifts to 1629

cm^{-1} for the current magnetic nanocrytals, which indicates the O that is coordinated in C=O presents a lower stretching frequency due to the attachment to nanoparticles' surface. The asymmetric CH_2 stretch (2952 cm^{-1}) and symmetric CH_2 stretch (2892 cm^{-1}) shifted to 2922 and 2852 cm^{-1}, respectively. In addition, FTIR spectra of the particles exhibit characteristic peaks of Mn_3O_4 at around ν_1 = 613 cm^{-1} ν_2 = 503 cm^{-1} respectively. The band at 1384 cm^{-1} can be assigned ν_1 vibrations of CO_2 molecules that are present in the sample chamber [157].

Table 1. Infrared Transmission Frequencies of 2-Pyrrolidone and the final product.

Observed Bands (cm^{-1})		
2-Pyrrolidone	**Product**	**Band Assignment**
3300-3250	3410, 3460	N-H strech
---	3570-3200	hydroxy group, H-bonded OH stretch
2962	2921	asymmetric CH_2 stretch
2892	2853	symmetric CH_2 stretch
1680	1637	C=O strech
1457, 1427	1383	C-H deformation
1286	1294	C-C-N streching
1168, 1064	1111	C-N streching
991	860	ring breathing
684	---	N-H out of plane bending
628	611	C=O out of plane bending
476	---	C-N-C bending

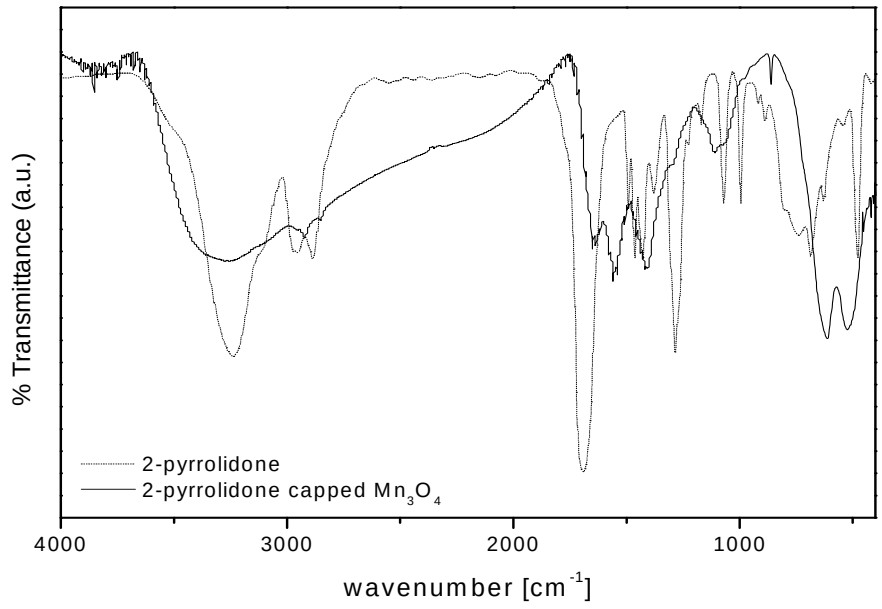

Figure 3.31. FTIR spectra of (a) pure 2-pyrrolidone, and (b) 2-pyrrolidone capped Mn_3O_4 nanoparticles.

3.3 SEM & TEM analysis

SEM and TEM analysis of as-prepared Mn_3O_4 sample was performed in order to study the material's microstructure and morphology; micrographs are presented in Fig. 3.32(a). SEM micrograph shows particles with spherical morphology with a wide range of sizes. Nanoparticles around 300 nm and as small as 40 nm were measured. Resolution of SEM micrographs did not allow us to make a comprehensive particle size evaluation. Therefore TEM analysis was performed and particles were shown to be spherical, and their distribution is represented by a histogram in Fig 3.32(c). In order to analyze the size distribution quantitatively, the particle size distribution was fitted using a log-normal function [158].

$$P(D) = \frac{A}{D\sigma_D\sqrt{2\pi}} \exp\left(-\frac{1}{2\sigma_D^2}\ln^2\left(\frac{D}{D_O}\right)\right) \quad (1)$$

where σ_D is the standard deviation of the diameter and D_0 is the mean diameter. A mean diameter of D_0 , as determined from Eq. (1), is about 14±0.4 nm. Size obtained from TEM analysis agrees well with the crystallite size obtained from XRD measurements using the peak broadening. Features observed in SEM are mainly secondary particles, that are formed as a result of aggregation/clustering of smaller ones. This is most probably due to the magnetization within the nanoparticles causing them to cluster. Detailed magnetic investigations are undertaken and results are to be reported elsewhere.

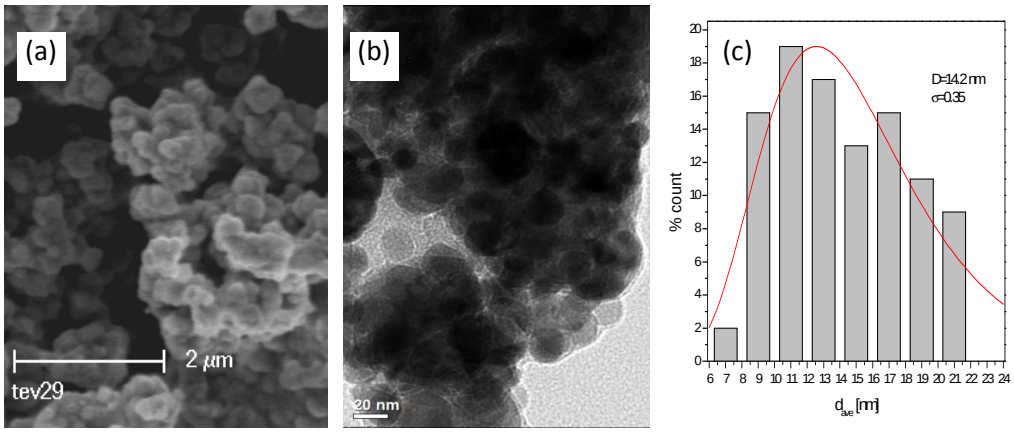

Figure 3.32. a) SEM micrograph, **b)** TEM micrograph, and **c)** calculated histogram of 2-pyrrolidone capped Mn_3O_4 nanoparticles.

The extent of surface coverage of nanoparticles with 2-pyrrolidone molecules were also analyzed using zeta potential mesaurements. Changes in the surface charge is directly based on the chemistry at the nanoparticles' surface. Figure 3.33 shows the results of analysis performed on as prepared sample dispersed in DI water. Surface of nanoparticles are positively charged at low pH values. Amide groups on 2-pyrrolidone are difficult to protonate. Surface of nanoparticles is not covered very densely due to the sterically bulky 2-pyrrolidone groups. So, nanoparticles' surface have still some OH^- groups exposed, which are protonated at low pH values that render the surface charge positive. The increase in pH removes the positive charge and negatively charges the accessible OH^- groups on nanoparticles' surface, thus reversing the initially observed

charge. The transition from positive charge to negative takes place at pH 4.8, which corresponds to the range where the isoelectric point for Mn_3O_4 particles is expected. Based on this analysis it is clear that Mn_3O_4 nanoparticles' surface is not fully covered and surface originating OH groups are accessible to the solution around.

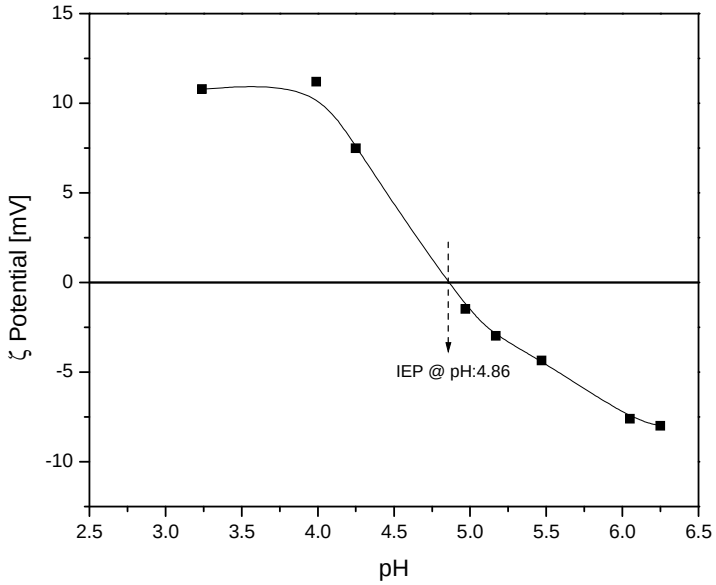

Figure 3.33. Surface potential measurement of a clear suspension of 2-pyrrolidone capped Mn_3O_4 nanoparticles.

3.3.2 Mn_3O_4 Nanoparticles by Oxidation-Reduction Method (*Tev12a & Tev21*)[3]

Mn_3O_4 is formed as a result of three step reaction that can be described as follows: i) formation of $Mn(OH)_2$ as a results of the reaction between $MnSO_4$ and NaOH; ii) partial oxidation of managanese hydroxide by $NaNO_3$ in solution, and finally iii) dehydration reaction of manganese hydroxide and manganese oxyhydroxide. Detailed reactions for the suggested mechanism controlling the transformation of managnese sulfate to the final phase of Mn_3O_4 are given below with respect to the order described above:

$$MnSO_4 + 2NaOH \rightarrow Mn(OH)_2 + Na_2SO_4 \quad [1]$$

$$3Mn(OH)_2 + NO_3^- \rightarrow Mn(OH)_2 + 2MnOOH + H_2O + NO_2 \quad [2]$$

$$Mn(OH)_2 + 2MnOOH \rightarrow Mn_3O_4 + 2H_2O \quad [3]$$

3.3.2.1. XRD Analysis

The X-ray diffraction (XRD) pattern of the as synthesized Mn_3O_4 is shown in Fig.3.34. All diffraction peaks were indexed to the tetragonal hausmannite crystal structure model of Mn_3O_4 (which are consistent bulk value (ICDD Card No: 24-0734). No characteristic peaks of impurities, indicating other forms of manganese oxides, were detected. The intensities of the reflection peaks for the two samples are more or less the same but the width of the reflection peaks are diffrent due to the difference in size of these two Mn_3O_4 nanoparticle samples (Tev 12a and Tev 21). Using Scherrer's formula, the average crystallite size was estimated to be about 14.4 nm for Tev 12a and 11 nm for Tev 21.

[3] T. Ozkaya, A. Baykal, H. Kavas, Y. Köseoğlu, M.S. Toprak, **"A novel synthetic route to Mn3O4 nanoparticles and their magnetic evaluation"**, doi:10.1016/j.physb.2008.07.002

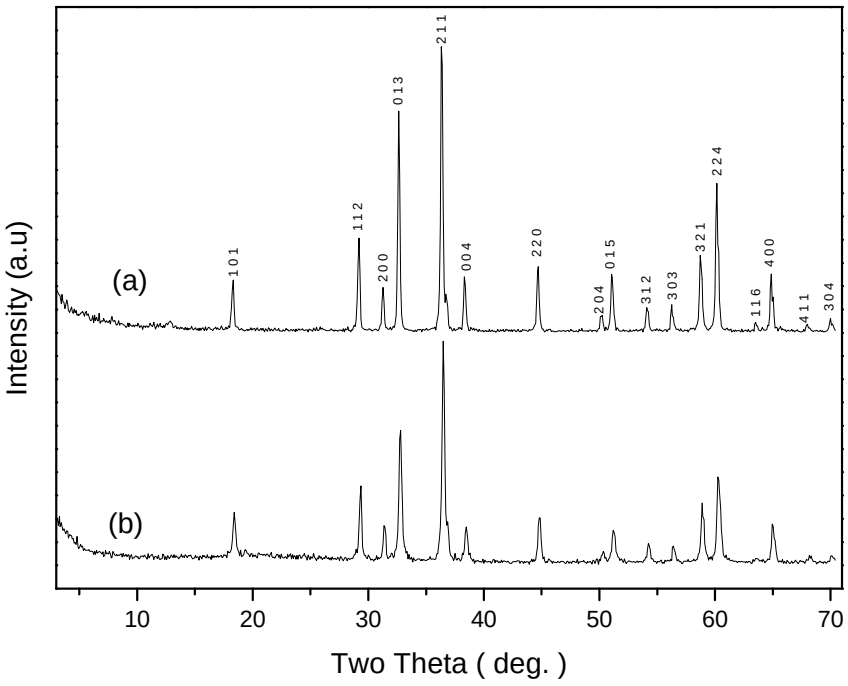

Figure 3.34. XRD patterns of Mn_3O_4 nanoparticles synthesized using (a) NaOH (Tev 12a); (b) NH_3 gas (Tev21) as hydrolyzing agent.

3.3.2.2. FTIR Analysis

FTIR analysis was performed for the prepared samples and spectra are presented in Fig. 3.35. Three significant absorption peaks are observed in the range of 400-650 cm^{-1} for both samples; vibration frequency at 635 - 638 cm^{-1} is characteristic of Mn-O stretching modes in tetrahedral sites whereas vibration frequency at 534 - 536 cm^{-1} corresponds to the distortion vibration of Mn-O in an octahedral environment. The third vibration band, located at a weaker wave number, 417 - 418 cm^{-1}, can be attributed to the vibration of manganese species (Mn^{3+}) in an octahedral site [159].

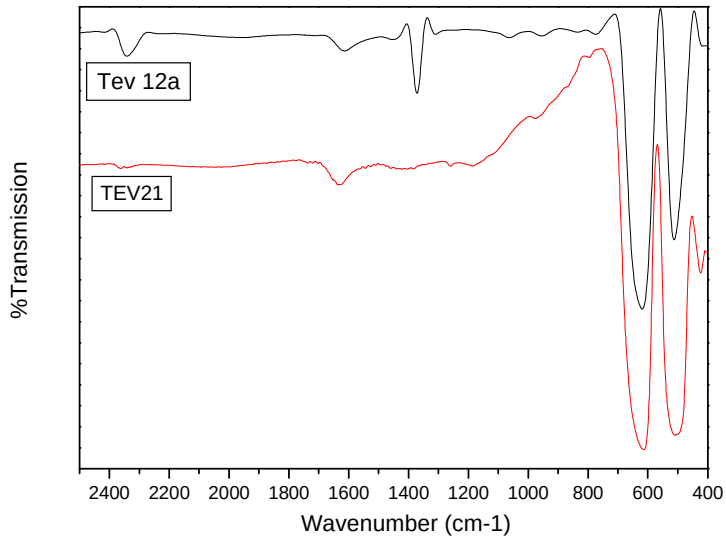

Figure 3.35. FTIR spectra of Mn_3O_4 of nanoparticles synthesized using (a) NaOH (Tev12a); (b) NH_3 gas (Tev21) as hydrolyzing agent.

3.3.2.3. TEM analysis

TEM analysis of Mn_3O_4 nanoparticles was performed to reveal the primary particle size, and micrographs are presented in Fig. 3.36. NaOH hydrolyzed samples showed spherical particles while aqueous ammonia hydrolyzed samples showed mixed morphologies from spherical to ellipsoids. Average particle size for both samples was calculated from several TEM micrographs. A particle size of 14±5 nm and 12±3 nm was obtained for the sample hydrolyzed with NaOH (Fig.3.36a) and conc. NH_3 (Fig 3.36b) respectively. NH_3 hydrolyzed samples are smaller than their NaOH hydrolyzed counterparts. This difference is due to the difference in the strength and concentration of hydrolyzing agents; NH_3 being about 6 times highly concentrated than NaOH. This in turn influences the nucleation rate thus the size of nuclei formed. In our earlier work we reported a similar observation on the synthesis of $NiFe_2O_4$ with CTAB assisted-hydrothermal using conc. NH_3 and 2M NaOH as hydrolyzing agents, where particle size of sample synthesized by conc. NH_3 was much smaller [160,161].

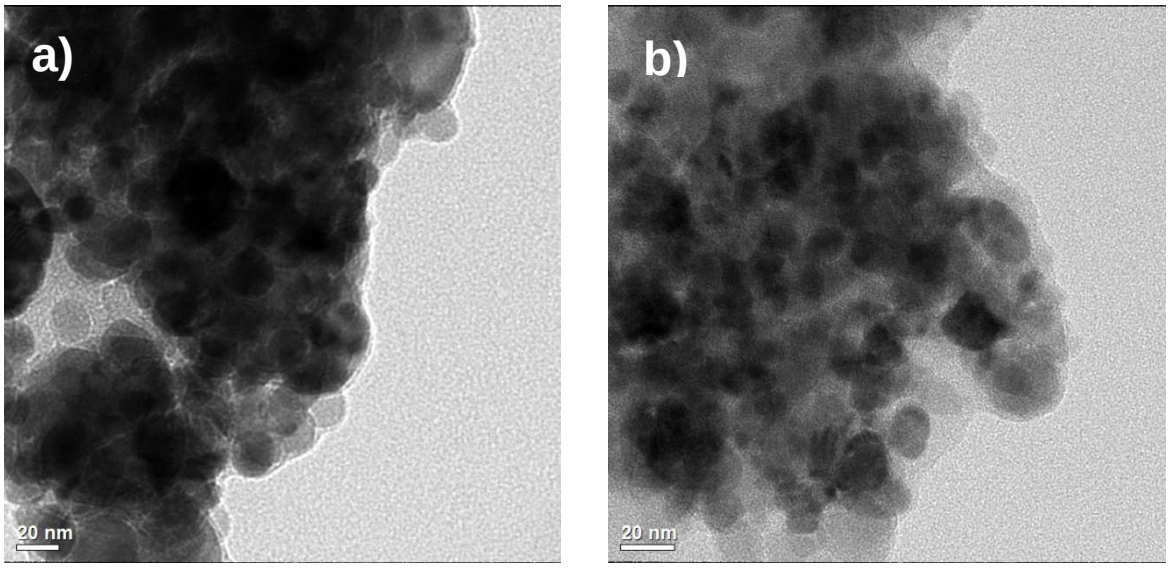

Figure 3.36. TEM micrographs of Mn_3O_4 nanoparticles synthesized using (a) NaOH (Tev12a); (b) NH_3 gas (Tev21) as hydrolyzing agent.

3.3.2.4. Magnetization

The magnetic properties of Mn_3O_4 nanocrystals have been studied by measuring the magnetization as a function of temperature; FC (with field of 200 Oe) M-T curves are shown in Fig.3.37 It reveals that the magnetization decreases by increasing the temperature up to 40 K and sharply decreases at around 40 K. It almost vanishes in the temperature range of 40-305 K. With decreasing temperature, a rapid increase of magnetization gives transition point in magnetic characteristics of samples, typically called Tc. To determine this point more accurately, the derivative of magnetizations with respect to temperature are given in insets of Figure 3.37 temperatures, Tc, are found as 38 K and 40 K for Tev12a and Tev21 respectively. The superparamagnetic threshold volumes of the particles at transition temperature, T_c, are calculated by using Arrhenius law : $V_{th} = k_B T \log(\tau / \tau_0) / K$, where K is the anisotropy constant and found as $V_{th} = 1.45 \times 10^{-19} cm^3$ ($D_{th} = 6.5$ nm) and $V_{th} = 1.53 \times 10^{-19} cm^3$ ($D_{th} = 6.6$ nm) for Tev12 and Tev21 respectively. Average particle size of our samples are also larger than the threshold ones like results of Zysler et al [162, 163]. This may cause lack of superparamagnetic behaviour, or dominated ferromagnetic behaviour to superparamagnetic one at around T_c .

The two samples show an obvious ferromagnetic behavior at low temperatures. The value of magnetization reduces significantly with the decrease of the size which might be attributed to the increasing of surface to volume (S/V) ratio, since the surface region leads to a decrease in the effective magnetic moment. T_C is dependent on the size of nanoparticles, smaller sizes of the Mn_3O_4 nanoparticles resulting in lower T_C values. These anomalous phenomena are expected from the effects of the finite size and the surface that is different from the bulk material as reported earlier for different magnetic nanoparticles [164-168].

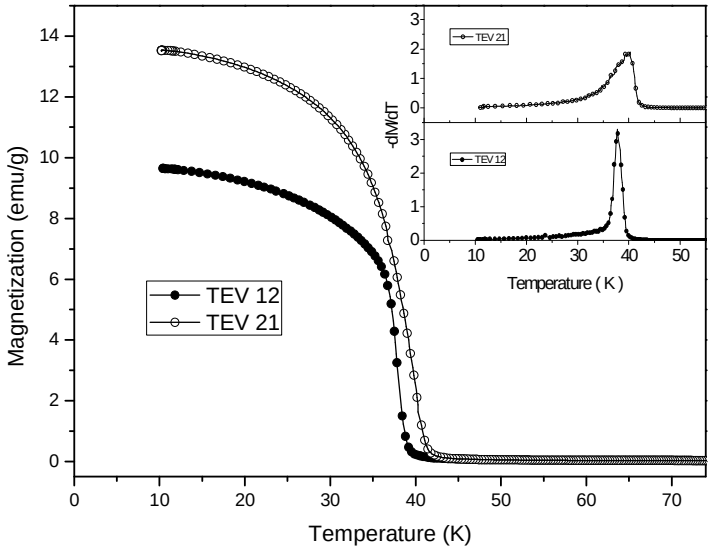

Figure 3.37. Temperature variation of the FC magnetization measurements of Mn_3O_4 nanoparticles synthesized using (a) NaOH (Tev12a); (b) NH_3 gas (Tev21) as hydrolyzing agent. The insets show the temperature derivative of the magnetization vs. temperature.

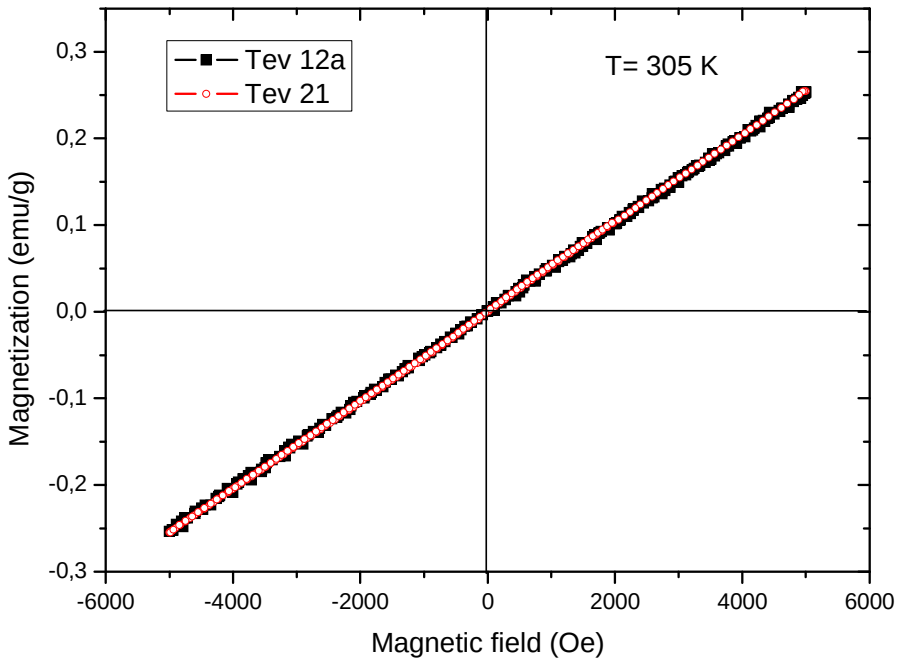

Figure 3.38. Room temperature M-H curves for Mn_3O_4 nanoparticles synthesized using (a) NaOH (Tev12a); (b) NH_3 gas (Tev21) as hydrolyzing agent.

The magnetization curves of both Mn_3O_4 samples at 305 K are shown in Fig. 3.38. M-H curves are linear with the field and have no coercivity at room temperature. Hysteresis in the single domain ferromagnetic particles vanishes when the particle size becomes so small that the maximum anisotropy energy becomes close to the thermal energy, so that the process of flipping of the single domain spin becomes uninhibited [169]. This state of the ferromagnetism is called 'superparamagnetism' as it does not show any hysteresis in its M–H behavior and like in the case of paramagnetism, the magnetization never gets saturated even at very high applied field. Room temperature magnetization curves for both samples show no hysteresis indicating the superparamagnetic character of the samples. Slight difference in size is not reflected in room temperature magnetization behavior. When ferromagnetic systems lose their multidomain character, they are then termed as single domain with their magnetic spins aligned along one of the easy directions of magnetization. An increasing fraction of

atoms lie at or near the surface as the particle size decreases and then surface spin effects and interface effects become more and more significant [170-172].

Large coercivity and shifted hysteresis loops are observed for different temperatures below Tc (see Fig.3.39). The saturation magnetization (M_s) was not reached even at 10 kOe applied magnetic field, but it can be estimated from the high field approximation of magnetization curves and found as 30.8 and 25.6 emu/g for Tev12a and Tev21 respectively at 10 K, where the bulk M_s is 38 emu/g [173]. The core magnetizations of samples at this temperature are obtained, by extrapolation of the high field magnetization to zero field and these are normalized to remanance magnetization values of each sample, as 0.89 for Tev12a and 0.92 for Tev21. By increasing the temperature, the volume ratio of core to all of the sample decreases from 0.77 (at 10 K) to 0.48 (at 40 K) and also normalized value of the core magnetization to the remanance magnetization decreases from 0.91 (at 10 K) to 0.32 (at 40 K) for TEV 21, indicating a smaller fraction of core and an increasing magnetic disorder of the system [163].

As expected, NaOH hydrolyzed sample (Tev12a) with slightly larger particle size showed a higher magnetization than NH_3 hydrolyzed sample (Tev21) at 10 kOe magnetic field. The difference in the magnetization behavior could also come from the differences in sample morphologies: spherical for Tev12a and ellipsoid+spherical for Tev21. The magnetic behavior of the Mn_3O_4 nanoparticles is under the influence of confined particle size. A principle effect of finite size is the breaking of a large number of bonds on the surface cations, producing a core of aligned spins surrounded by a disordered shell. This can result in a disordered spin configuration near to the surface and a reduced average net moment compared to the bulk materials. In addition, the difference in surface spin states can result in high field hysteresis and relaxation of the magnetization, as has been observed for these nanoparticles [174-176]. When superparamagnetic particles are cooled below certain temperature they transform to ferromagnetic state. The thermal energy at this temperature becomes significantly less than the anisotropy energy (KV) and thus cannot facilitate uninhibited flipping of the single domain spins. As a result, the ferromagnetic onset temperature decreases with decrease in size of the single domain particles [177-180]. At low temperatures blocking of the single domain spins by the anisotropy forces gives rise to hysteresis in the M–H plots. At 10 K the observed coercive fields are 1350 Oe and 3070 Oe, for Tev21 and

Tev12a respectively, less than that of bulk Mn_3O_4. The difference in the observed coercive field values can be attributed the difference in the size of the samples, Tev12a exhibiting a higher coercive field due to its larger particle size [174].

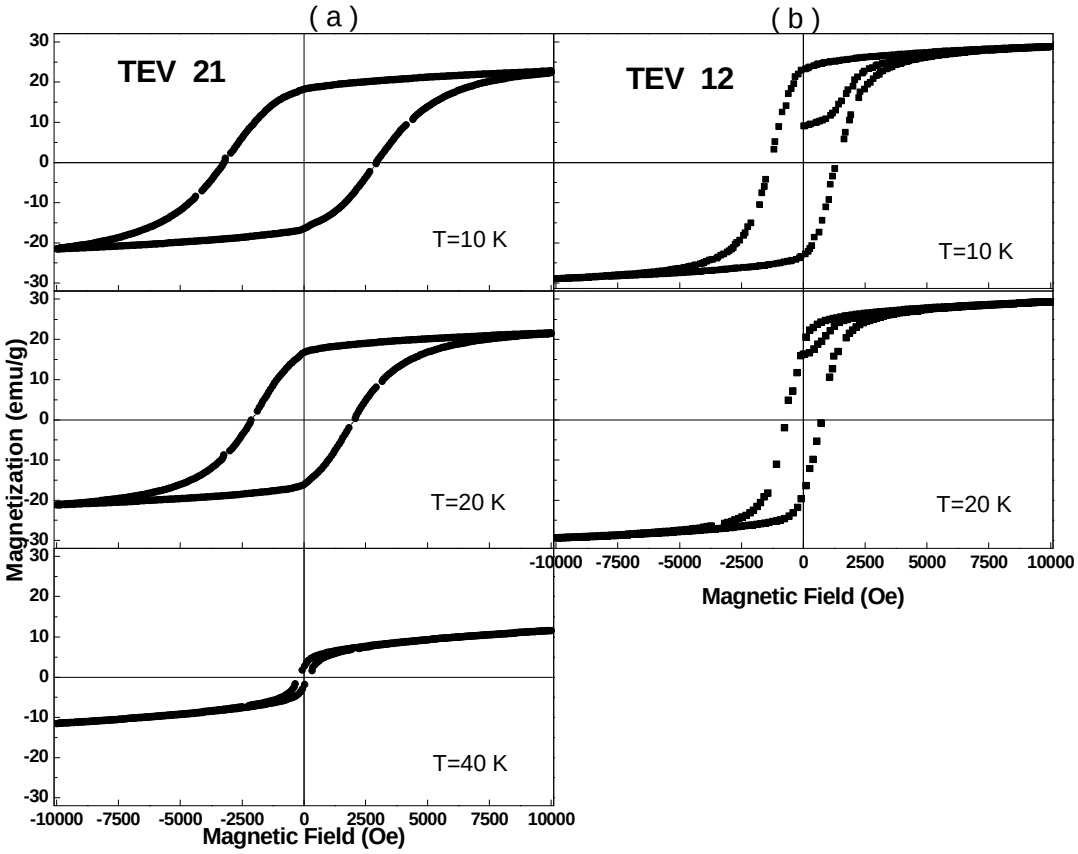

Figure 3.39. M-H curves measured at Temperatures below T_c for Mn_3O_4 nanoparticles synthesized using (a) NH_3 gas (Tev21); (b) NaOH (Tev12a) as hydrolyzing agent.

3.3.3 PEG-asisted Route (*Te 5*)

3.3.3.1 XRD analysis

XRD pattern shows of samples prepared were seen in Fig. 3.40. The characteristic peaks at 2θ angles correspond very well to the standart card of Mn_3O_4 (JCPDS Card No 18-0803) which proves that the samples can be identified as Mn_3O_4. The crystallite size of the samples was calculated as 23.22 nm with the Scherrer's equation.

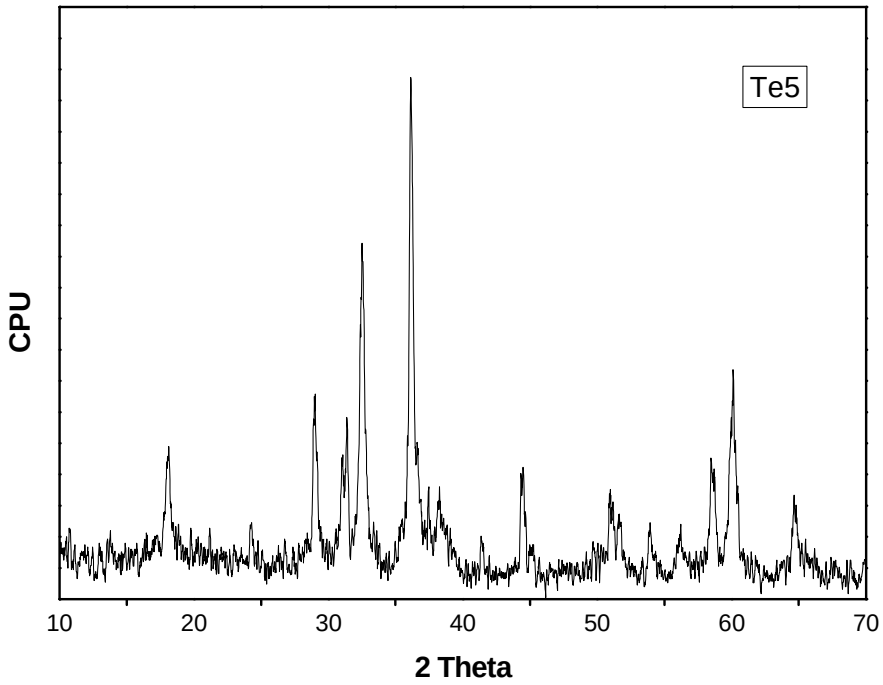

Figure 3.40. XRD patterns of PEG-Mn_3O_4 nanoparticles

3.3.3.2 FTIR analysis

Vibration of ions in the crystal lattice are usually observed in the range of 1000-400 cm^{-1}. Two main broad metal-oxygen bands are seen in the FTIR spectra of all spinels, and ferrites in particular. The highest one, ν_1, generally observed in the range 600-500 cm^{-1}, corresponds to intrinsic stretching vibrations of the metal at the tetrahedral site (T_d), $M_{tetra} \leftrightarrow O$, whereas the ν_2 – lowest band usually observed in the range 450-385 cm^{-1}, is assigned to octahedral-metal stretching (O_h), $M_{octa} \leftrightarrow O$ [181]. Due to the limitation of our FTIR instrument below 400 cm^{-1}, ν_3 (328 cm^{-1}) and ν_4 (below 300 cm^{-1}) were not detected. The FTIR measurements reveal that the vibrational band of C-O bond shifts from 1113 cm^{-1} for pure ethylene glycol to 1095 cm^{-1} for the current Mn_3O_4 nanoparticles, which indicates that the O from C-O coordinates with metal on the surface of zinc doped nickel ferrite nanocrystals. Similarly, the bands around 2910 cm^{-1} and 955 cm^{-1} corresponded to $–CH_2$ stretching vibrations and –CH out of plane bending vibrations, respectively. The $–CH_2$ and –CH peaks were strong evidence that PEG was chemically bonded to the surface. The surfactant molecules in the adsorbed state are influenced by the field of solid state surface. As a result, the characteristic bands shifted to a lower frequency region (Fig.3.41). In the previous reports [182-184], it has been justed that the functional head groups of the surfactant have a coordination bond or strong interaction with nanoparticles and thus kinetically control the growth rates of various faces of crystals, which can control the morphology. It has been reported that PEG with a uniform and ordered chain structure is easily absorbed at the surface of metal oxide colloid [185]. When the surface of the colloid adsorbs this type of polymer, the activities of colloid greatly decrease and the growth rate of the colloids in some certain facet will be confined [186,187]. Therefore, the addition of PEG in the metal oxide colloids will modify the growth kinetics of the growing colloids, which finally, leads to anisotropic growth of the crystals. Due to this, linear PEG has been widely used in the synthesis of a series of nanoparticulates and 1D materials in solution [186].

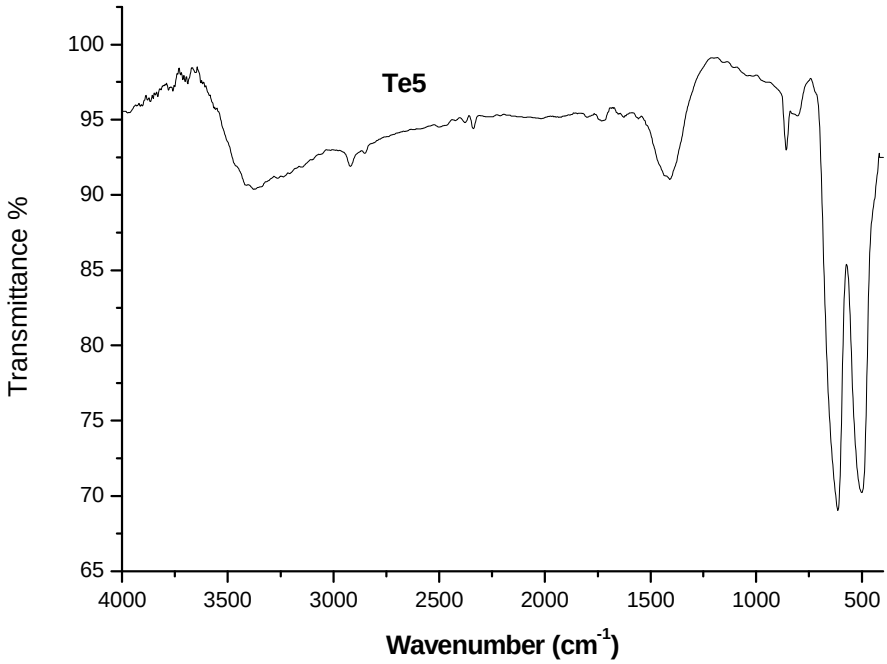

Figure 3.41. FTIR spectra of PEG-Mn_3O_4 nanoparticles.

CHAPTER 4

CONCLUSION

Superparamagnetic iron oxide nanoparticles were successfully synthesized by a simple, novel, and cost-effective gel-to-crystalline method starting from a single component and hydrolyzing at 80-100 ^{o}C under refluxing conditions. XRD analysis suggested non-stoichiometric magnetite with lattice parameter between magnetite and maghemite. The average crystallite size for this non-stoichiometric magnetite is calculated as 11 nm from XRD peak broadening, and 11.4 nm from TEM micrographs. Magnetic domain size is calculated from magnetization curves as 9.7 nm, which is slightly smaller than XRD and TEM size, due to the magnetically dead layer at the nanoparticles' surface. The sample shows superparamagnetic behavior above 300 K with a saturation magnetization, M_s, of 390emu/cm^3. The reduction of M_s from its bulk value can be attributed partly to the presence of non-magnetic (dead) surface layer due to the compositional variations from magnetite to maghemite, superparamagnetic relaxation and spin canting because of the ultrafine nature of the material. Measured T_B of 134 K falls in the range observed in the literature for comparable sized magnetite nanoparticles. Results also indicate the existence of interparticle interactions in the thermomagnetic characteristics of spinels at lower field strengths. Furthermore, iron oxide nanoparticles synthesized in this work could be useful for biomedical applications as magnetic carriers or contrasting agents due to their small particle size and superparamagnetic property above room temperature.

In this work manganese oxide, Mn_3O_4, nanoparticles were successfully synthesized by a novel oxidation-precipitation method in which starting material manganese sulfate was oxidized to manganese salts by $NaNO_3$ that were subsequently hydrolyzed with NaOH and conc. NH_3, without use of any surfactant. To our best knowledge, this is the first report for the synthesis of Mn_3O_4 nanocrystals by using NH_3 as hydrolyzing agent. Formation of Mn_3O_4 nanoparticles was confirmed by XRD analysis. Samples exhibit different crystallite size, estimated based on Scherrer formula, as ~14 nm for NaOH and ~11 nm for NH_3 hydrolyzed samples. Average particle size obtained from TEM analysis as 14±5 nm for NaOH and 12±3 nm for NH_3 hydrolyzed samples show a good agreement with XRD crystallite size. Both samples exhibit superparamagnetic behavior at room temperature, with no apparent saturation magnetization in the region of measured field strength and relatively large coercivity below the ferromagnetic transition temperature. Magnetic measurements performed at 10K showed that NaOH hydrolyzed sample with slightly larger particle size showed a higher saturation magnetization and higher coercivity than NH_3 hydrolyzed sample, which was assigned to scaling of magnetic properties with particle size. Due to the absence of hysteric behavior and no apparent saturation at room temperature, the particles are considered as single superparamagnetic domains with random orientations of magnetic moments and thermal fluctuations of anisotropic axes. The magnetic behavior of Mn_3O_4 nanoparticles is sensitive to particle size, and the ferromagnetic transition temperatures of both samples are lower than that observed for bulk Mn_3O_4 value. Below the transition, the observed differences in temperature dependence of magnetization, hysteresis loop shape and type of the samples from the bulk values are attributed to their smaller size (increase in surface to volume ratio) of the samples which cause the increase of effective magnetic surface anisotropy.

In summary, we have shown that it is possible to prepare water soluble nanocrytals of Mn_3O_4 in the absence of water or air by thermal decomposition of managanese acetylacetonate in a high boiling solvent of 2-pyrrolidone as a novel synthetic approarch. The experimental results reveal that 2-pyyrolidone not only serves as a media for high temperature decomposition reaction, but also involves surface coordination which renders the manganese nanocrytals water-soluble and the colloidal solution stable. TEM analysis revealed the size of nanoparticles as ~14±0.4 nm, in

agreement with the size calculated from XRD peak broadening as 15 nm. Particles are readily dispersed in aqueous solution; however they cluster due to their inherent magnetization. Zeta potential analysis revealed surface OH groups are still present, most likely due to sterically bulky 2-pyrrolidone groups, and are exposed to surrounding solution.

REFERENCES

[1] Feynman R: There's plenty of room at the bottom. Science, 254 (1991) 1300.

[2] Sheeparamatti, B. G. ; Sheeparamatti, R. B. ; Kadadevramath, J. S. Nanotechnology : inspiration from matue. IETE Tech. Rev. 24 (2007) 5.

[3] Whitesides, G. M. Nature Biotech. 21 (2003) 1161.

[4] UK Government Report " Nanoscience and Nanotechnologies: Opportunities and Uncertainties" 29 July 2004 (http://nanotec.org.uk).

[5] J. Jortner, C.N.R. Rao: Pure Appl. Chem. 74 (2002)1491

[6] "Nanoparticle assemblies and superstructures", edited by Nicholas A. Kotov,. CRC Press, Taylor & Francis Group. (2006).

[7] "Synthesis and Functionalization of Magnetic Iron Oxide Nanoparticles for Application in Organic Chemistry", L. Guifeng, 2007, Tianjin-China.

[8] "Nanocrystals; Synthesis, Properties and Applications", Rao,C.N.R, Springer Berlin Heidelberg ,2007.

[9] D.J. Barber, I.C. Freestone: Archaeometry 32 (1990) 33.

[10] a) Jos´e-Yacam´an,L.Rend´on, J. Arenas et al.: Science 273 223 (1996)b) nature photonics, VOL 1, APRIL 2007 (www.nature.com/naturephotonics)

[11] Stupp, S. I. Chem. Rev. 105 (2005) 1123.

[12] Burda, C.; Chen, X.; Narayanan, R.; EI-Sayed, M. Chem. Rev. 105 (2005) 1025.

[13] Cushing, B. L.; Kolesnichenko, V. L.; O'Connor C. J. Chem. Rev. 104 (2004) 3893.

[14] "Synthesis, Functionalization and Surface Treatment of Nanoparticles", Edited by Marie-Isabelle Baraton University of Limoges, FRANCE: January 2003.

[15] "Nanoscale Materials in Chemistry", Edited by Kenneth J. Klabunde, 2001.

[16] "Nanosystem Charecterization Tools In the Life Sciences", edited by Challa S. S. R. Kumar,2006.

[17] P.P. Edwards, R.L. Johnston, C.N.R. Rao: The size-induced metal–insulator transition in clusters and metal particles in: Metal clusters in Chemistry, ed by P. Braunstein, G. Oro, P.R. Raithbay (Wiley-VCH, Weinheim 1998).

[18] A.I. Kirkland, D.E. Jefferson, D.G. Duff et al.: Proc. R. Soc. London A 440 (1993) 589.

[19] T.P. Martin, T. Bergmann, H. G¨ohlich et al.: J. Phys. Chem. B 95 (1991) 6421.

[20] H. Klug, L.E. Alexander: X-ray Diffraction Procedures for Polycrystalline and Amorphous Materials (Wiley, New York 1974).

[21] D.G. Duff, A.C. Curtis, P.P. Edwards et al.: Angew. Chem. Int. Ed. 26 (1987) 676.

[22] O. Bovin, J.O. Malm: Z. Phys. D: Atoms, Molecules and Clusters 19 (1991) 293.

[23] W. Thomson: Philos. Mag. 42 (1871) 448.

[24] P. Pawlow: Z. Phys. Chem. 65 (1909) 545.

[25] M. Takagi: J. Phys. Soc. Jpn. 9 (1954) 359.

[26] Ph. Buffat, J.-P. Borel: Phys. Rev. A13 (1976) 2287.

[27] W.A.deHeer:Rev.Mod.Phys.65 (1993) 611.

[28] M. Brack: Rev. Mod. Phys. 65 (1993) 677.

[29] M. Haruta, N. Yamada, T. Kobayashi et al.: J. Catal. 115 (1989) 301.

[30] G.K. Bethke, H.H. Kung: Appl. Catal. 43 (2000) 194.

[31] M. Valden, X. Lai, D.W. Goodman: Science 281 (1998) 1647.

[32] S. Link, M.A. El-Sayed: Int. Rev. Phy. Chem. 19 (2000) 409.

[33] B.O. Dabbousi, J. Rodriguez-Viejo, F.V. Mikulec et al.: J. Phys. Chem. B101 (1997) 9463.

[34] C. Liu, Z. J. Zhang: Chem. Mater. 13 (2001) 2092.

[35] C.R. Vestal, Z.J. Zhang: Int. J. Nanotechnol. 1 (2004) 240.

[36] O. Masala, R. Seshadri: Chem. Phys. Lett. 402 (2005)160.

[37] C. Liu, B. Zou, A.D. Rondinone: J. Am. Chem. Soc. 122 (2000) 6263.

[38] C. Liu, Z. J. Zhang: Chem. Mater. 13 (2001) 2092.

[39] C. Liu, B. Zou, A.D. Rondinone: J. Am. Chem. Soc. 122 (2000) 6263.

[40] N. Mathur and P. Littlewood, "The third way", Nature Materials, 3, (2004) 207.

[41] G.B. Sergeev ,"Nanochemistry", Elsevier, New York, 2006.

[42] M.T. Swihart: Curr. Opin. Colloid Interface Sci. 8 (2003)127.

[43] C. Burda, X. Chen, R. Narayanan et al.: Chem. Rev. 105 (2005)1025.

[44] B.L. Cushing, V.L. Kolesnichenko, C.J. O'Connor: Chem. Rev. 104 (2004) 3893.

[45] www.wikipedia.org.

[46] P.R. van Rheenen, M.J. McKelvey, R. Marzke et al.: Inorg. Synth. 24 (1983) 238.

[47] "Metal nanoparticles synthesis , characterization, and application", by Daniel L. Fedlheim and Colby A. Foss, 2001.

[48] M. Brust, M. Walker, D. Bethell et al.: J. Chem. Soc., Chem. Commun. (1994) 801.

[49] S. Sun, C.B. Murray: J. Appl. Phys. 85 (1999) 4325.

[50] S. Bradley, E.W. Hill, S. Behal, C.Klein, B.Chaudret , A.Duteil, Chem. Mater. 4 1(1992) 234.

[51] Rajamathi, R. Seshadiri: Curr. Opn. Sol. Stat. Mater. Sci. 6 (2002) 337.

[52] C. Zhang, Z. Kang, E. Shen et al.: J. Phys. Chem. B110 (2006) 184.

[53] J. Zu, J.-P. Ge, Y.-D. Li: J. Phys. Chem. B110 (2006) 2497.

[54] W.S. Seo, J.H. Shim, S.J. Oh et al.: J. Am. Chem. Soc. 127 (2005) 6188.

[55] M.Y. Han, L. Zhow, C.H. Quek et. al.: Chem. Phys. Lett. 287 (1998) 47.

[56] M.T. Reetz, W. Helbig, S.A. Quaiser: Active Metals,edbyA.F¨urstner, p. 339 (Wiley-VCH, Weinham 1996).

[57] H. Bonnemann, W. Brijoux, R. Brinkmann et al.: Inorg. Chim. Acta 350 617 (2003) .

[58] A.B. Bourlinos, A. Simopoulos, D. Petrides: Chem. Mater. 14 (2002) 899.

[59] P.J. Thomas, P. Saravanan, G.U. Kulkarni et al.: Pramana J. Phys. 58 (2002) 371.

[60] F. Grieser, R. Hobson, J.Z. Sostaric et al.: Ultrasonics 34 (1996) 547.

[61] M.-P. Pileni: Langmuir 17 (2001) 7476.

[62] N. Moumen, M.-P. Pileni: J. Phys. Chem. 100 (1996) 1867.

[63] S. Qiu, J. Dong, G. Chen: J Colloid Interface Sci. 216 (1999) 230.

[64] a) C.N.R. Rao, G.U. Kulkarni, P.J. Thomas, V.V. Agarwal and P. Saravanan, 85 (2003) 1041. b) C.N.R. Rao, G.U. Kulkarni, P.J. Thomas, V.V. Agarwal and P. Saravanan J. Phys. Chem. B107 (2003) 7391.c) C.N.R. Rao, G.U. Kulkarni, V.V. Agrawal, U.K. Gautam, M. Ghosh and U. Tumkurkar, J. Colloid Interface Sci. 289 (2005) 305. d) U.K. Gautam, M. Ghosh, C.N.R. Rao: Langmuir 20 (2004) 10775. e)V.V. Agrawal, G.U. Kulkarni, C.N.R. Rao: J. Phys. Chem. B109 (2005) 7300.

[65] C Liu, B Zou, AJ Rondinone, ZJ Zhang, J Phys Chem B 104 (2000) 1141.

[66] T. Sugimoto. Monodisperse Particles. Amsterdam: Elsevier, 2001, pp.793.

[67] N.A. Kotov, “Assembly of Magnetic Nanoparticles”, CRS Press, New York 2005.

[68] EV Shevchenko, DV Talapin, AL Rogach, A Kornowski, M Haase, H Weller, J Am Chem Soc 124 (2002) 11480.

[69] S. Sun, CB Murray, H Doyle. Controlled assembly of monodisperse e-cobalt-based nanocrystals. Mater Res Soc Symp Proc 577 (1999) 385.

[70] V.F. Puntes, K Krishnan, AP Alivisatos, Top Catalysis 19 (2002) 145.

[71] a) C.J. Murphy, N.R. Jana: Adv. Mater. 14 (2002) 80 b) N.R. Jana, L. Gearheart, C.J. Murphy: Chem. Commun. (2001) 617.

[72] a) N.R. Jana, L. Gearheart, C.J. Murphy: J. Phys. Chem. B 105 (2001) 4065 b)J. Gao, C.M. Bender, C.J. Murphy: Langmuir 19 (2003) 9065 c)N.R. Jana, L. Gearheart, C.J. Murphy: Adv. Mater. 13 (2001) 1389.

[73] T.K. Sahu, C.J. Murphy: J. Am. Chem. Soc. 126 (2004) 8648.

[74] Nanoparticles: Building Blocks For Nanotechnology, edited by Vincent Rotello, 2003.

[75] Pillai, V.; Kumar, P. ; Hou, N.J. ;Ayyub, ; Shah, D. O. Adv. Coll. Inter. SCI. 1995, 55, 241.

[76] Klabunde, K. j.; Zhang, D. ; Glavee, G. N. ; Sorensen, C. M. Chem. Mater. 6 (1994) 784.

[77] Lin, X. M. ; Sorensen, C. M. ; Klabunde, K. J. ; Hajinpanayis, G. C. J. Mater. Res. 14 (1999) 1542.

[78] Teranishi, T, ; Miyake, M. Chem. Mater. 11 (1999) 3414.

[79] Park, S. J. ; Kim, S. ; Lee , S. ; Khim, Z. G. ;Char, K. Hyeon, T. J. Am. Chem. Soc/ 122 (2000) 8581.

[80] Burke, N.A. ;Stover, H. D. H. ; Dawson, F. P. ; Lavers, J. D. ; Jain, P. K. ; Oka, H. IEEE Trans. Magn. 37 (2001) 2660.

[81] Puntes, V. F. ; Krishan, K.M. ; Alivisatos , A. P. Science 291 (2001) 2115.

[82] Koltypin, Y.; Cao, X. ; Balogu, J. ; Kaptas, D. ; Gedanken, A. J. Mat.. Chem. 7 (1997) 2453.

[83] F. Grasset, S. Mornet, A. Demourgues, J. Portier, J. Bonnet and AVE Duguet. J. Magn. Magn. Mater. 234 (2001) 409.

[84] a) J. Seongjin, “Magnetism and Magnetotransport of Magnetic Arrays, Doctor of Philosophy, December 2007, Newyork-USA b) http://wikis.lib.ncsu.edu/

[85] Nanotechnology Basic Science and Engineering Technologies, edited by Mick Wilson, Kamali Kannangara, Geoff Smith, and Michelle Simmons, 2002.

[86] http://www.malvern.com

.

[87] Magnetic materials group website at the University at Birmingham, UK, http://www.aacg.bham.ac.uk/magnetic_materials/type.htm (December, 2007).

[88] Robert C. O'handley, Modern Magnetic Materials, John Wiley & Sons Inc., 2000, p.16.

[89] Neil W. Ashcroft and N. David Mermin, Solid State Physics, Harcourt College Publisher, Orlando, Florida, 1976, p. 696.

[90] B. D. Cullity, Introduction to Magnetic Materials, Addison-Wesley Publishing company, Reading, Massachusetts, 1972, p.117.

[91] http://www.geo.umn.edu/orgs/irm/hg2m/hg2m_b/hg2m_b.html.

[92] http://www.ndt-ed.org/EducationResources.

[93] Charles Kittel, Introduction to Solid State Physics, 7th edition, John Wiley & Sons, Inc.,New York, 1996, p. 464.

[94] M. Anilkumar, V. Ravi, Mater. Res. Bull. 40 (2005) 605.

[95] P. H. Refait, J. M. R. Génin, Corros. Sci. 34 (1993) 797.

[96] A. A. Olowe, J. M. R. Génin, Corros. Sci. 32 (1991) 965.

[97] T.J.Daou, G.Pourroy, S.Begin-Collin, J.M.Greneche, C.Ulhaq-Bouillet, P.Legare, P.Bernhardt, C.Leuvrey, G.Rogez, Chem Mater., 18(18) (2006) 4399.

[98] T.Belin, N. Guigue-Millot, T.Caillot, D.Aymes, J.C.Niepce, J.Solid State Chem., 163 (2002) 459.

[99] N. Guigue-Millot, Y.Champion, M.J.Hytch, F.Bernard, S.Begin-Collin, P.Perriat, J.Phys.Chem. 105 (2001) 2175.

[100] J.P.Jolivet, E.J.Tronc, J.Colloid Interface Sci. 125 (1998) 688.

[101] C.N.J. Wagner, E.N. Aqua, Adv. X-ray Anal. 7 (1964) 46.

[102] B. D. Hall, D. Zanchet and D. Ugarte, J. Appl. Cryst. 33 (2000) 1335.

[103] T. Wejrzanowski, R. Pielaszek, A. Opalinska, H. Matysiak, W. Łojkowski, K.J. Kurzydłowski, Applied Surface Science 253 (2006) 204.

[104] R. Pielaszek, Analytical expression for diffraction line profile for polydispersive powders, Appl. Crystallography, Proceedings of the XIX Conference, Krako´w, Poland, September 2003. p. 43.

[105] S.Wei, Y.Zhu, Y.Zhang, J.Xu, Reactive and Functional Polymers, 66 (2007) 1272.

[106] R.A.Nyquist, R.O.Kagel, Infrared Spectra of Inorg.Comp., New York, Academic Press, 1971

[107] I.J. Bruce, J. Taylor, M. Todd, M.J. Davies, E. Borioni, C.Sangregorio, T. Sen, J. Magn. Magn. Mater. 284 (2004) 145.

[108] T. Kim, and M. Shima, J. Appl. Phys. 101 (2007) 09M516.

[109] W.J. Liang, M. Bockrath, D. Bozovic, J.H. Hafner, M. Tinkham, H. Park, Nature 411 (2001) 665.

[110] D.H. Han, J.P. Wang, H.L. Luo, J. Magn. Magn. Mater. 136 (1994) 176.

[111] S.Chikazumi, Physics of Ferromagnetism second edition, Clarendon Press, Oxford, 1997.

[112] E. Blum, A. Cebers, M. M. Maiorov, Magnetic Fluids, Walter de Gruyter, Berlin, 1997.

[113] I. Nedkov, T. Merodiiska, L. Milenova, T. Koutzarova, J. Magn. Magn. Mater. 211 (2000) 296.

[114] Z..Wang, H. Guo, Y. Yu, N. He, J. Magn. Magn. Mater. 302 (2006) 397.

[115] B. Jia and L. Gao, Scripta Materialia 56 (2007) 677.

[116] D.K. Kim, Y. Zhang, W. Voit, K.V. Rao, M. Muhammed, J. Magn. Magn. Mater. 225 (2001) 30.

[117] R.H. Kodama, A.E. Berkowitz, E.J. McNiff, S. Foner Phys. Rev. Lett. 77 (1996) 394.

[118] J.K. Vassiliou, V. Mehrotra, M.W. Russell, E.P. Giannelis, R.D. McMichael, R.D. Shull, R.F. Ziolo, J. Appl. Phys. 73 (1993) 5109.

[119] R. Massart, IEEE Trans. Magn. MAG-17 (1981) 1247.

[120] B.D. Cullity, Introduction to Magnetic Materials, Addison-Wesley, Reading, MA, 1974, p. 94.

[121] C. M. Sorensen, Nanoscale Materials in Chemistry (Ed.: K. J. Klabunde), John Wiley and Sons, Inc., New York, 2001, pp. 169.

[122] E. Blum, A. Cebers, M. M. Maiorov, Magnetic Fluids, Walter de Gruyter, Berlin, 1997.

[123] M. Blanco-Manteco, K.O'Grady, J. Magn. Magn. Mater. 296 (2006) 124.

[124] Z.X. Tang, C.M. Sorensen, K.J. Klabunde, G.C. Hadjipanayis, J. Appl. Phys. 69 (1991) 5279.

[125] R. Kaiser, G. Miskolczy, J. Appl. Phys. 41 (1970) 1064.

[126] S.Shufeng, C. Li, X. Wang, D. Yu, Q. Peng and Y. Li, Crystal Growth & Design 5 (2005) 391.

[127] J.Wan, G. Ttang, Y. Qian, Appl. Phys. A 86 (2007) 261.

[128] Yanglong Hou, Junfeng Yu and Song Gao, J. Mater. Chem. 13 (2003) 1983.

[129] D.K. Kim, Y. Zhang, W. Voit, K.V. Rao, M. Muhammed, JMMM 225 (2001) 30.

[130] D. L. Pelecky, R.D. Rieke, Chem. Mater. 8 (1996) 1770.

[131] A. Sawatsky, F. van der Woude, A.H. Morrish, J. Appl. Phys. 39 (1968) 1204.

[132] G. Gnanaprakash, S. Mahadevan, T. Jayakumar, P. Kalyanasundaram, John Philip, Baldev Raj, Materials Chemistry and Physics, 103, (2007), 168.

[133] R.A.Nyquist, R.O.Kagel, Infrared Spectra of Inorg.Comp., New York, Academic Press, 1971.

[134] I.J. Bruce, J. Taylor, M. Todd, M.J. Davies, E. Borioni, C.Sangregorio, T. Sen, J. Magn. Magn. Mater. 284 (2004) 145.

[135] Nakamato K., Infrared and Ramn Spectra of Inorganic and Coordination Compounds, New York, Wiley, 1986.

[136] Lin H.K., Chiu H.C., Tsai H.C., Catal.Lett., 88, 2003 , 169.

[137] J.A. Gaddsden, Infrared Spectra of Minerals and Related Inorganic Compounds, Butterworth, London, 1975, p. 44.

[138] Y. Chen, Y. Zhang, S.Fu, Materials Letters 61 (2007) 701.

[139] Christokova St.G., Stayonava M., Georgieva M., Mehandjiev D., Mater.Chem. Phys., 60 (1999) 39.

[140] Salah A. Makhlouf, J. Magn. Magn. Mater. 246 (2002) 184.

[141] E.L. Salabas, A. Rumplecker, F. Kleitz, F. Radu, F. Schüth, Nano Lett. 6 (2006) 2977.

[142] W.L. Roth, J. Phys. Chem. Solids 25 (1964) 1.

[143] Salah A. Makhlouf, J. Magn. Magn. Mater. 246 (2002) 184.

[144] Y. Ichiyanagi, Y. Kimishima, S. Yamada, J. Magn. Magn. Mater. 272–276 (2004) e1245–e1246.

[145] D.V. Vadehra, K.R. Nath, CRC Crit. Rev. Food Technol. 4 (1973) 193.

[146] E. Li-Chen, S. Nakai, CRC Crit. Rev. Poultry Biol. 8 (1989) 21.

[147] Y. Mine, Trends Food Sci. Technol. 6 (1995) 225.

[148] O. Lyckfeldt, J. Brandt, S. Lesca, J. Eur. Ceram. Soc. 20, (2000) 2551.

[149] S. Dhara, P. Bhargava, J. Am. Ceram. Soc. 84 (2001) 3045.

[150] S. Dhara, P. Bhargava, J. Am. Ceram. Soc. 86 (2003) 1645.

[151] S. Dhara, J. Am. Ceram. Soc. 88 (2005) 2003.

[152] S. Maensiri, C. Masingboon, B. Boonchom, S. Seraphin, Scripta Materialia 56 (2007) 797.

[153] Z.H. Zhou, J.M. Xue, J. Wang, H.S.O. Chan, T. Yu and Z.X. Shen, J. Appl. Phys. 91 (2002) 6015.

[154] F.Kurtuluş, H.Güler, Inorg.Mat., 41(5) (2005) 483.

[155] R. A. Meyers, Interpretation of Infrared Spectra, A Practical Approach. J. Coates in Encyclopedia of Analytical Chemistry, (Ed.), 10815, John Wiley, Chichester, 2000.

[156] R.M. Silverstein, G.C. Bassler, and T.C. Morrill, Spectrometric Identification of Organic Compounds. 4th ed. New York: John Wiley and Sons, 1981.

[157] K. Nakamato, Infrared and Raman Spectra of Inorganic and Coordination Compounds, New York, Wiley, 1986.

[158] T.Kim and M.Shima, J.Appl.Phys. 101 09M516 (2007).

[159] M. Ishii, M. Nakahira, Solid State Commun. 11 (1972) 209.

[160] A. Baykal, N. Kasapoglu, Y. Köseoglu, M.S. Toprak, H. Bayrakdar, J. Alloys Comp (2007), doi:10.1016/j.jalcom.2007.10.041.

[161] N. Kasapoglu, "Synthesis, Characterization and ESR Studies of Magnetic Spinel Materials", Master Thesis, Fatih University, January 2007, Istanbul-TURKEY.

[162] R.D. Zysler, H. Romero, C.A. Ramos, E. De Biasi, D. Fiorani, J. Magn. Magn.Mater. 266 (2003) 233.

[163] E.Winkler, R.D. Zysler, D. Fiorani, Phys. Rev. B 70 (2004) 174406.

[164] R.H. Kodama , A.E. Berkovitz , E.J., Jr.McNiff, S. Foner, Phys. Rev. Lett. 77 (1996) 394.

[165] R.H. Kodama , S.A. Makhlouf , A.E. Berkovitz , Phys. Rev. Lett. 79 (1997) 1393.

[166] R.H. Kodama, A.E. Berkovitz , Phys. Rev. B 59(1999) 6321.

[167] Y. Köseoğlu , H. Kavas J. Nanosci. Nanotechnol. 8 (2008) 584.

[168] Y. Köseoğlu , H. Kavas, B.Aktaş, Phys. Stat. Solid. (a) 203 (2006) 1595.

[169] C. Liu, A.J. Rondinone, Z. J. Zhang, Pure Appl. Chem. 72(1-2) (2000) 37.

[170] R.D. Sanchez, J. Rivas, P. Vaquerio, M.A .Lopez-Quintela, D. Caeiro, J. Magn. Magn. Mater. 247 (2002) 92.

[171] H. Nathani, R.D.K. Misra, Mater. Sci.& Eng. B 113 (2004) 228.

[172] Z. Huang, Q. Feng, Z. Chen, S. Chen, Y. Du, Microelect. Eng. 66 (2003) 128.

[173] T R.S. Ebble, D.J. Craik, Magnetic Materials, Academic Press, NewYork, 1969

[174] N. Kasapoğlu, A. Baykal, Y. Köseoğlu, M.S. Toprak, Scripta Materialia 57 (2007) 441.

[175] K. Binder, P.C. Hohenberg, Phys. Rev. B 9 (1974) 2194.

[176] K. Dwirby, N. Menyuk, Phys. Rev. 119 (1960) 1470.

[177] J.P. Chen, S.C. Morensen, K.J. Klabunde, G.C. Hadjipanayis, E. Devlin, A. Kostas, Phys. Rev. B 54 (13) (1996) 9285.

[178] G. Mathew, A.M. John, Swapna S. Nair, P.A. Toy, M.R. Anantharaman, J. Magn. Magn. Mater. 302 (2006) 190.

[179] A. E. Berkowitz, R. H. Kodama, S. A. Makhlouf, F. T. Parker, F. E. Spada, E. J. McNiff Jr., S. Foner, J. Magn. Magn. Mater. 196-197 (1999) 591.

[180] R.D. Sanchez, J. Rivas, P. Vaquerio, M.A. Lopez-Quintela, D. Caeiro, J. Magn. Magn. Mater. 247 (2002) 92.

[181] S.Hafner, Z.Krist., 115 (1961) 331.

[182] Z.Chen. L.Gao, Mater.Sci.Eng. B (2007), doi:10.1016/jmseb.2007.06.003.

[183] Z.Q.Li, Y.J.Xiong, Y.Xie, Inorg.Chem. 42 (2003) 8105.

[184] Y.G.Sun, Y.N.Xia, Adv.Mater. 14 (2002) 833.

[185] J. Dobryszycki, and S. Biallozor, Corrosion Science 43 (2001) 1309.

[186] M. Bognitzki, H.Q.Hou, M. Ishaque, T.Frese, M.Hellwig, C.Schwarte, A.Schaper, J.H. Wendorff, A.Greiner, Adv.Mater. 12 (2000) 637.

[187] X.H.Lu, J.Yang, L.Wang, X.J.yang, L.D.Lu, X.Wang, Mater.Sci.Eng. A 289 (2000) 241.